

TRANSIENT SIGNAL DETECTION IN CONTINUOUS GPS COORDINATE  
TIME SERIES USING EMPIRICAL MODE DECOMPOSITION AND  
PRINCIPAL COMPONENT ANALYSIS

A THESIS SUBMITTED TO  
THE GRADUATE SCHOOL OF NATURAL AND APPLIED SCIENCES  
OF  
MIDDLE EAST TECHNICAL UNIVERSITY

BY

SONER ÖZDEMİR

IN PARTIAL FULFILLMENT OF THE REQUIREMENTS  
FOR  
THE DEGREE OF DOCTOR OF PHILOSOPHY  
IN  
GEODETIC AND GEOGRAPHIC INFORMATION TECHNOLOGIES

JULY 2019



Approval of the thesis:

**TRANSIENT SIGNAL DETECTION IN CONTINUOUS GPS COORDINATE  
TIME SERIES USING EMPIRICAL MODE DECOMPOSITION AND  
PRINCIPAL COMPONENT ANALYSIS**

submitted by **SONER ÖZDEMİR** in partial fulfillment of the requirements for the degree of **Doctor of Philosophy in Geodetic and Geographic Information Technologies Department, Middle East Technical University** by,

Prof. Dr. Halil Kalıpçılar  
Dean, Graduate School of **Natural and Applied Sciences** \_\_\_\_\_

Prof. Dr. Zuhâl Akyürek  
Head of Department, **Geodetic and Geographical Inf. Tech.** \_\_\_\_\_

Prof. Dr. Mahmut Onur Karşlıođlu  
Supervisor, **Geodetic and Geographical Inf. Tech., METU** \_\_\_\_\_

**Examining Committee Members:**

Prof. Dr. Haluk Özener  
KOERI, Bođaziçi University \_\_\_\_\_

Prof. Dr. Mahmut Onur Karşlıođlu  
Geodetic and Geographical Inf. Tech., METU \_\_\_\_\_

Assoc. Prof. Dr. Utku Kanođlu  
Aerospace Engineering Dept., METU \_\_\_\_\_

Assoc. Prof. Dr. Uđur Murat Lelođlu  
Geodetic and Geographical Inf. Tech., METU \_\_\_\_\_

Assist. Prof. Dr. Kamil Teke  
Geomatics Engineering, Hacettepe University \_\_\_\_\_

Date: 26.07.2019

**I hereby declare that all information in this document has been obtained and presented in accordance with academic rules and ethical conduct. I also declare that, as required by these rules and conduct, I have fully cited and referenced all material and results that are not original to this work.**

Name, Surname: Soner Özdemir

Signature :

## ABSTRACT

### **TRANSIENT SIGNAL DETECTION IN CONTINUOUS GPS COORDINATE TIME SERIES USING EMPIRICAL MODE DECOMPOSITION AND PRINCIPAL COMPONENT ANALYSIS**

Özdemir, Soner

Doctor of Philosophy, Geodetic and Geographic Information Technologies

Supervisor: Prof. Dr. Mahmut Onur Karşlıoğlu

June 2019, 171 pages

Continuous Global Positioning System (GPS) coordinate time series might be exposed to tectonic and non-tectonic transient signals as well as the persistent signals such as secular rates and seasonal motions. Transient signal detection becomes challenging when the targeted signal is weak and buried in the noise. Incoherency of the transient signal in space and large number of sites in the GPS network make the detection even more complicated. We propose a new approach based on Empirical Mode Decomposition (EMD) and Principal Component Analysis (PCA) in this study to detect tectonically-driven transient signals. Thanks to the adaptive nature of EMD, we did not make any a priori assumptions about the type of the colored noise present in the time series, and suppressed the white noise by means of the filtering properties of the EMD method. We utilized PCA to recognize the coherent but localized transient signals in space. The main geographic area of interest is Turkey. We focused on analyzing the data collected in CORS-TR network, which is a real-time kinematic type permanent network in Turkey, and making the time series employable in tectonic monitoring. We demonstrated the existence of Common Mode Error (CME) at CORS-TR sites and reduced it for further investigations. We proved the capability of our method by successfully detecting the slow slip events in Cascadia, the transient

inflation at Akutan volcano, Alaska, and the postseismic deformation following the October 23, 2011 Van earthquake, Turkey.

Keywords: Transient Signal, GPS, EMD, PCA, CORS-TR

## ÖZ

### **DENEYSSEL MOD AYRIŞTIRMA VE TEMEL BİLEŞENLER ANALİZİ İLE SÜREKLİ GPS KOORDİNAT ZAMAN SERİLERİNDE GEÇİCİ SİNYAL TESPİTİ**

Özdemir, Soner  
Doktora, Jeodezi ve Coğrafi Bilgi Teknolojileri  
Tez Danışmanı: Prof. Dr. Mahmut Onur Karşlıoğlu

Temmuz 2019, 171 sayfa

Sürekli Küresel Konumlama Sistemi (GPS) koordinat zaman serileri, doğrusal hız ve mevsimsel hareketler gibi varlığı süreklilik arz eden sinyaller kadar, tektonik veya başka etkenlerden kaynaklanan geçici sinyaller de içerebilmektedir. Hedeflenen geçici sinyalin zayıf ve gürültünün içinde gömülü olması, tespitini zorlaştırmaktadır. Bu sinyallerin mekansal olarak tutarlılık göstermemesi ve GPS ağında fazla sayıda istasyon bulunması durumu daha da güçleştirmektedir. Bu çalışmada, GPS zaman serilerinde tektonik kaynaklı zayıf sinyallerin tespiti için Deneysel Mod Ayırıştırma (EMD) ve Temel Bileşenler Analizi (TBA) tabanlı yeni bir yaklaşım önerilmektedir. EMD'nin adaptif yapısı sayesinde, zaman serilerinde mevcut olan renkli gürültünün türü hakkında varsayımda bulunma zorunluluğu olmamakta, yöntemin filtreleme özellikleri sayesinde beyaz gürültü bastırılabilir. TBA, mekansal olarak sınırlı bir bölgede tutarlı bir şekilde varlığını gösteren geçici sinyalleri tespit edebilmektedir. Coğrafi olarak temel ilgi alanı Türkiye'dir. TUSAGA-Aktif ağında toplanan verilerin analiz edilmesine ve üretilen zaman serilerinin tektonik izleme amaçlı kullanılabilir hale getirilmesine odaklanılmıştır. TUSAGA-Aktif istasyonlarında Ortak Mod Hatasının (CME) varlığı tespit edilerek giderilmiştir. Önerilen yöntemin yetenekleri, Cascadia bölgesindeki yavaş atım olaylarının (SSE), Akutan Volkanı'ndaki (Alaska)

şişmenin ve 23 Ekim 2011 tarihli Van depreminin ardından TUSAGA-Aktif istasyonlarında meydana gelen postsismik deformasyonun başarılı şekilde tespit edilmesiyle ortaya konmuştur.

Anahtar Kelimeler: Geçici Sinyal, GPS, EMD, TBA, TUSAGA-Aktif



To my beloved daughter ~ADA~

## ACKNOWLEDGMENTS

I would like to express my gratitude to my supervisor Prof. Dr. Mahmut Onur KARSLIOĞLU for his guidance throughout my thesis studies. I have always admired his deep knowledge in geodesy and related sciences, and his inspiring teaching style.

I thank my thesis committee, Prof. Dr. Haluk ÖZENER, Assoc. Prof. Dr. Utku KANOĞLU, Assoc. Prof. Dr. Uğur Murat LELOĞLU and Assist. Prof. Dr. Kamil TEKE for their constructive criticism that helped to improve the manuscript.

I gratefully acknowledge the assistance of Assist. Prof. Dr. Murat DURMAZ in developing some of the codes. I have always enjoyed our scientific conversations.

This study would not have been possible without the continuous data of CORS-TR stations operated by General Directorate of Mapping, and General Directorate of Land Registry and Cadastre, Turkey.

This study was partially supported by Scientific and Technological Research Council of Turkey (TUBITAK) under the grant number 113Y511.

## TABLE OF CONTENTS

ABSTRACT .....	v
ÖZ .....	vii
ACKNOWLEDGMENTS .....	x
TABLE OF CONTENTS .....	xi
LIST OF TABLES .....	xv
LIST OF FIGURES .....	xvi
LIST OF ABBREVIATIONS .....	xix
CHAPTERS	
1. INTRODUCTION .....	1
1.1. Motivation .....	1
1.2. Objectives .....	9
1.3. Thesis Outline.....	11
2. GLOBAL POSITIONING SYSTEM AND COORDINATE TIME SERIES ..	13
2.1. GPS Segments .....	13
2.1.1 Space Segment.....	13
2.1.2 Control Segment .....	14
2.1.3 User Segment.....	15
2.2. GPS Signal Structure .....	16
2.3. GPS Observables and Parameter Estimation.....	17
2.3.1 Code Pseudorange Observable .....	17

2.3.2	Carrier Phase Observable.....	18
2.3.3	Least Squares Estimation.....	22
2.4.	High-precision GPS Positioning.....	23
2.5.	GPS Time Series.....	26
3.	EMPIRICAL MODE DECOMPOSITION.....	35
3.1.	Motivation.....	35
3.2.	Empirical Mode Decomposition.....	40
3.3.	Limitations of the Empirical Mode Decomposition .....	43
3.3.1.	Mathematical Foundation .....	44
3.3.2.	Envelope Interpolation.....	45
3.3.3.	Boundary Effects.....	46
3.3.4.	Stopping Criterion.....	46
3.3.5.	Confidence Limit and Statistical Significance.....	47
3.3.6.	Missing Data Points .....	48
3.3.7.	Mode Mixing.....	49
3.4.	Methodological Improvements .....	50
3.4.1.	Ensemble Empirical Mode Decomposition .....	51
3.4.2.	CEEMD and CEEMDAN .....	53
3.5.	Signal Denoising with EMD.....	54
4.	PRINCIPAL COMPONENT ANALYSIS .....	61
4.1.	Introduction.....	61
4.2.	Principal Components Transformation.....	62

5.	GPS ANALYSES AND TRANSIENT SIGNAL DETECTION .....	67
5.1.	High-precision GPS Analyses .....	68
5.1.1.	Introduction.....	68
5.1.2.	CORS-TR Data .....	70
5.1.3.	GPS Data Processing .....	72
5.1.4.	Quality Assessment.....	76
5.1.4.1.	Satellite Visibility .....	76
5.1.4.2.	Antenna Phase Center Models .....	77
5.1.4.3.	One-way LC Phase Residuals .....	78
5.1.4.4.	Multipath.....	80
5.1.4.5.	Proximity to the Active Faults .....	80
5.1.5.	Time Series Analysis .....	82
5.1.6.	Overview of Analysis Results.....	90
5.1.7.	Velocity Field .....	92
5.1.8.	Common Mode Error Reduction .....	95
5.2.	Transient Signal Detection .....	99
5.2.1.	Slow Slip Events in Cascadia .....	109
5.2.2.	Transient inflation at Akutan Volcano.....	120
5.2.3.	Postseismic deformation following October 23, 2011 Van Earthquake	125
6.	DISCUSSION, CONCLUSIONS AND FUTURE WORK .....	135
6.1.	Discussion .....	135
6.2.	Conclusions .....	138

6.3. Future Work.....	142
REFERENCES.....	145
CURRICULUM VITAE .....	165

## LIST OF TABLES

### TABLES

Table 2.1. IGS GPS products .....	25
Table 2.2. Best noise model for SGIN and SBAR.....	33
Table 3.1. Comparison of HHT with Fourier and Wavelet Analyses.....	37
Table 3.2. The EMD algorithm.....	41
Table 3.3. The EEMD algorithm .....	51
Table 3.4. Confidence interval parameters .....	59
Table 4.1. Flowchart of the PCA .....	65
Table 5.1. CORS-TR stations which have the poorest satellite visibility.....	77
Table 5.2. The highest mean RMS values and associated standard deviations .....	79
Table 5.3. Stations with the highest multipaths .....	80
Table 5.4. Stations within 2 km of the active faults.....	81
Table 5.5. Stations which have high mean (M) daily coordinate uncertainties .....	83
Table 5.6. Sites experienced coseismic displacements during the analysis period... 87	
Table 5.7. Comparison of the GPS analysis.....	92
Table 5.8. NRMS values of the velocity estimates of the IGS sites .....	94
Table 5.9. External validation of GPS results .....	95
Table 5.10. The overall daily dispersion in common-mode corrected time series ...	99

## LIST OF FIGURES

### FIGURES

Figure 2.1. Navigation message cycle.....	15
Figure 2.2. The definition of the phase .....	19
Figure 2.3. Daily GPS time series of ADIY and MUGL stations .....	27
Figure 2.4. Daily GPS time series of ANKR and HALP stations .....	27
Figure 2.5. Daily GPS time series of MURA and ADAN stations .....	28
Figure 2.6. Daily GPS time series of KNY1 station .....	29
Figure 2.7. Daily GPS time series of BTMN and EMIR stations .....	30
Figure 2.8. Photo of GPS antenna at EMIR station.....	30
Figure 2.9. Daily GPS time series of INEB and SEMD stations .....	31
Figure 3.1. Phase planes, phase functions, instantaneous frequencies.....	40
Figure 3.2. The sifting procedure .....	42
Figure 3.3. AFYN data and its EMD components .....	44
Figure 3.4. Mode mixing.....	50
Figure 3.5. EEMD solution to mode mixing.....	52
Figure 3.6. Rescaled spectra of IMF components of noise-only signals.....	56
Figure 3.7. IMF log-variance controlled by the Hurst index.....	57
Figure 3.8. Statistical characteristics of IMF variances .....	58
Figure 3.9. Relation between IMF variance and mean period .....	59
Figure 5.1. CORS-TR stations .....	71
Figure 5.2. CORS-TR monument types .....	71
Figure 5.3. IGS sites included in the analyses.....	74
Figure 5.4. Sky plot of CATK station .....	76
Figure 5.5. LC phase residuals vs. elevation angles for EDIR station .....	77



Figure 5.6. LC phase residuals showing bad pattern .....	78
Figure 5.7. Histogram of the mean RMS of the LC phase residuals .....	79
Figure 5.8. The multipaths at the BTMN station .....	81
Figure 5.9. RMS values obtained in the reference frame definition .....	83
Figure 5.10. Daily coordinate uncertainties of IZMI station .....	84
Figure 5.11. Daily coordinate uncertainties of all CORS-TR stations.....	85
Figure 5.12. Repeatabilities of the CORS-TR stations .....	86
Figure 5.13. The earthquakes and the affected CORS-TR sites .....	87
Figure 5.14. The outlier detection .....	89
Figure 5.15. The realistic sigma curve .....	90
Figure 5.16. The Eurasia-fixed CORS-TR velocity field .....	93
Figure 5.17. CORS-TR stations used in the regional reference frame definition ....	97
Figure 5.18. CME correction at ADIY station.....	100
Figure 5.19. EEMD decomposition of the ERGN east component .....	103
Figure 5.20. Standardized means of the IMF components of ERGN station.....	104
Figure 5.21. Log-variance of the IMF components of ERGN station .....	106
Figure 5.22. Denoising of the ERGN east time series .....	107
Figure 5.23. Tectonic map of Cascadia.....	110
Figure 5.24. The east motion of the Victoria station.....	111
Figure 5.25. The 2007 and 2008 ETS events .....	112
Figure 5.26. Cascadia stations used in transient signal detection .....	113
Figure 5.27. The detrended time series of Cascadia stations .....	114
Figure 5.28. The filtered time series of Cascadia stations .....	115
Figure 5.29. The SNR improved time series of Cascadia stations.....	115
Figure 5.30. The first PCs from the PCA applied to Cascadia stations .....	116
Figure 5.31. The percent variability from original detrended time series.....	118
Figure 5.32. The percent variability from filtered time series .....	118
Figure 5.33. The percent variability from SNR improved time series.....	119

Figure 5.34. The Alaska sites used in the transient signal detection .....	121
Figure 5.35. The percent variability from raw and SNR improved time series .....	122
Figure 5.36. The first PC of the CME-reduced-SNR-improved time series .....	122
Figure 5.37. Sites on the Akutan Island used in the analysis .....	123
Figure 5.38. The first and second PC of Akutan sites .....	124
Figure 5.39. The percent variability from SNR improved time series at Akutan ...	125
Figure 5.40. The coseismic and postseismic motions of VAAN and MURA .....	127
Figure 5.41. Time series of ARDH, ERZR and UDER stations .....	128
Figure 5.42. CORS-TR stations used in the transient signal detection .....	129
Figure 5.43. Comparison of PCs before and after the application of the method...	130
Figure 5.44. The percent variability from raw and SNR improved time series .....	131
Figure 5.45. The spatial pattern of the first PC of the raw time series .....	132
Figure 5.46. The spatial pattern of the first PC after our method applied .....	133

## LIST OF ABBREVIATIONS

### ABBREVIATIONS

AS	Analytic Signal
C/A	Coarse Acquisition
CEEMD	Complementary Ensemble EMD
CEEMDAN	Complete EEMD with Adaptive Noise
CME	Common Mode Error
CORS-TR	Turkish National Permanent GNSS Network-Active
DOF	Degrees of Freedom
DORIS	Orbitography and Radiopositioning Integrated by Satellite
EEMD	Ensemble Empirical Mode Decomposition
EGNOS	European Geostationary Navigation Overlay Service
EMD	Empirical Mode Decomposition
EOF	Empirical Orthogonal Function
ERP	Earth Rotation Parameter
ETS	Episodic Tremor and Slip
fBm	Fractional Brownian motion
fGn	Fractional Gaussian noise
FOGM	First-order Gauss-Markov
FT	Fourier Transform
GA	Ground Antenna
GAMIT	GPS Analysis at MIT
GDLRC	General Directorate of Land Registry and Cadastre
GDM	General Directorate of Mapping
GEONET	GPS Earth Observatory Network
GLOBK	Global Kalman filter VLBI and GPS analysis program
GNSS	Global Navigation Satellite Systems
GPS	Global Positioning System
H	Hurst index
HHT	Hilbert Huang Transform
HSA	Hilbert Spectral Analysis
IAG	International Association of Geodesy

ICA	Independent Component Analysis
IDS	International DORIS Service
IERS	International Earth Rotation and Reference Systems Service
IGS	International GNSS Service
ILRS	International Laser Ranging Service
IMF	Intrinsic Mode Function
InSAR	Interferometric Synthetic Aperture Radar
IQR	Inter Quartile Range
IRLS	Iteratively Reweighted Least Squares
ITRF	International Terrestrial Reference Frame
IVS	International VLBI Service
JPL	Jet Propulsion Laboratory
LAAS	Local-Area Augmentation System
LC	Linear Combination
MCS	Master Control Station
MIT	Massachusetts Institute of Technology
MP	Multipath
MS	Monitor Station
NRMS	Normalized Root Mean Square
NTRIP	Network Transport of RTCM
P	Precise
PBO	Plate Boundary Observatory
PC	Principal Component
PCA	Principal Component Analysis
PCV	Phase Center Variation
PNT	Positioning, Navigation and Timing
PPP	Precise Point Positioning
RMS	Root Mean Square
RSS	Remote Sensing Systems
RTCM	Radio Technical Commission for Maritime
RTK	Real Time Kinematic
RTS	Real-Time Service
SBAR	Southern part of the Basin and Range Geodetic Network
SD	Standard Deviation
SGIN	Southern California Integrated GPS Network
SNR	Signal-to-noise Ratio

SOPAC	Scripps Orbit and Permanent Array Center
SSE	Slow Slip Event
SVD	Singular Value Decomposition
TRNC	Turkish Republic of Northern Cyprus
TUBITAK	Scientific and Technological Research Council of Turkey
UAH	University of Alabama at Huntsville
USA	United States of America
VEP	Variance Explanation Percentage
VEPR	Variance Explanation Percentage Rate
VLBI	Very Long Baseline Interferometry
WAAS	Wide Area Augmentation System
WRMS	Weighted Root Mean Square
WSD	Weak Signal Detection
WT	Wavelet Transform



## CHAPTER 1

### INTRODUCTION

This study is about detecting transient signals in Global Positioning System (GPS) coordinate time series (hereinafter referred to as “GPS time series”). To this end, ~ 10-year-long data from Turkish National Permanent GNSS Network-Active (CORS-TR), which consists of homogeneously distributed permanent reference stations, are analyzed carefully and GPS time series are generated. Empirical Mode Decomposition (EMD) and Principal Component Analysis (PCA) are used to enhance the signal-to-noise ratio of the time series in time and space domain, respectively. Capability of the method is demonstrated through applications to known real transient signals. The motivation, objectives, and the thesis outline are described in the next subsections.

#### 1.1 Motivation

GPS is the oldest of the Global Navigation Satellite Systems (GNSS). Since the launch of the first satellite by the United States in 1978 for military purposes primarily, it has become an indispensable tool in a wide range of applications calling for real-time positioning, navigation or timing (PNT), such as surveying, mapping, aviation etc. Very roughly, distance vectors between a GPS receiver and at least four GPS satellites in view are calculated and intersected to determine the location of the receiver in three dimensions.

Space segment of the system has been modernized over the past decades with new generation satellites which possess extended capabilities. There are 31 operational satellites in the constellation as of January 9, 2019 (<https://www.gps.gov/>) to ensure the simultaneous visibility of at least four satellites at any time, anywhere on Earth. The accuracy and reliability of GPS-derived locations might be increased by incorporating satellite-based augmentation systems, such as Wide Area Augmentation System (WAAS) and European Geostationary Navigation Overlay Service (EGNOS), or ground based augmentation systems, such as Local-Area Augmentation System (LAAS), which transmit additional parameters to the receivers to be used in the correction of the calculated positions.

Improvements on the side of the user segment were also significant. Instrumental development in the receivers and antennas, combinations of GPS observables, mitigating the effects of the error sources through proper modeling etc. made contribution in gaining the highest precision. In addition, International GNSS Service (IGS) (<http://www.igs.org/>) which is affiliated to International Association of Geodesy (IAG) (<http://www.iag-aig.org/>), provides high-quality data and data products, such as satellite orbits, Earth Rotation Parameters (ERPs), global ionosphere maps, which are essential for PNT applications. IGS also contributes to the International Terrestrial Reference Frame (ITRF) (Altamimi et al., 2016) which provides an accurate datum to which almost all global and regional networks tied. ITRF is generated by combining the long-term solutions from IGS (Dow et al., 2009), the International Very Long Baseline Interferometry (VLBI) Service (IVS) (Schuh and Behrend, 2012), the International Doppler Orbitography and Radiopositioning Integrated by Satellite (DORIS) Service (IDS) (Willis et al., 2010), and the International Laser Ranging Service (ILRS) (Pearlman et al., 2002).



Conventional horizontal and vertical control networks which were generally formed by trilateration and spirit leveling measurements mostly gave their places to unified GPS/GNSS networks today, thanks to the three dimensional nature of the satellite systems. GPS receivers and antennas are easily transported and unaffected by the atmospheric conditions, and visibility between sites is not required. Currently, it is possible to obtain the coordinates of a point with millimeter level precision. However, it is mainly due to its relative inexpensiveness that GPS became popular among above mentioned space geodetic techniques (Segall and Davies, 1997). When used together, its relatively high spatial and temporal resolution might add value to the findings of strainmeters and Interferometric Synthetic Aperture Radar (InSAR), respectively. It has been widely used as a versatile tool in the studies of various physical processes such as, dynamic ground motions (e.g., Grapenthin and Freymueller, 2011; Geng et al., 2016; Huang et al., 2017), plate motions (e.g., Kreemer et.al., 2014; Prawirodirdjo and Bock, 2004), polar motion (e.g., Dong et al., 2002), volcano deformation (e.g., Ji and Herring, 2011; Freymueller and Kaufman, 2010), coseismic ionospheric disturbance (e.g., Liu and Jin, 2019), earthquake studies (e.g., Larson, 2009; Tanaka et al., 2018) and hydrology (e.g., King et al., 2007; Tregoning et al., 2009).

Considering the advantages, and the achievements reached with reasonable budgets, continuously operating GPS/GNSS networks with various scales have been established increasingly. Such networks are utilized in geophysical studies successfully. The global IGS network consists of more than 500 GPS/GNSS stations. To monitor actively deforming areas, specially designed regional networks are formed such as Plate Boundary Observatory (PBO) in the United States and GPS Earth Observatory Network (GEONET) in Japan. Both networks have over 1000 stations. Recently, a real-time kinematic (RTK) network (CORS-TR) consists of 158 reference stations (as of May 1, 2019) has been established in Turkey and in Turkish Republic of Northern Cyprus.

Although the main purpose of the CORS-TR network is to provide correction parameters to the rovers in the field, static data collected at the reference stations might also be useful for tectonic studies. On the other hand, although having been situated at the intersection of major tectonic plates and being abundant of crustal deformation, Turkey is deprived of any national-scale continuous GPS/GNSS network specifically designed for tectonic studies. Thus, assessing the availability of CORS-TR in crustal deformation studies is important.

Although higher-rate samplings can be studied (e.g., Bock et al., 2004; Larson et al., 2007), processing the continuous GPS data daily and getting one position estimate per day for each station is common. These estimates together form coordinate time series in each of the three dimensions. Changes in the daily coordinates of stations are the results of noise and several signals riding on a secular velocity that might or might not be related to the tectonics.

The station velocity is assumed to be linear due to tectonic plate motion. Annual and semi-annual signals can bias the velocity estimates (Blewitt and Lavallee, 2002). These quasi-seasonal signals might be originated from (1) surface mass redistributions due to, e.g., ocean tide and atmospheric loadings, (2) thermal reasons such as bedrock thermal expansion, and (3) various errors due to e.g., satellite orbit and atmosphere models (Dong et al., 2002). Due to the aliasing effects of diurnal and semi-diurnal signals (Penna et al., 2007), sinusoids of constant amplitude might not represent the seasonal signals perfectly (Bennet, 2008).

Discontinuities due to, e.g., updates in processing strategy (e.g., changing from relative to absolute antenna phase center corrections), equipment changes (of antenna, radome etc.) which might also result in noise changes, and coseismic displacements are also often in GPS time series. Outliers due to, e.g., adverse atmospheric conditions

might contaminate the time series (Ostini, 2012). Most outlier detection algorithms assume a model of the patterns in the data, and decide whether a data point is an outlier according to the level of the deviations from these patterns (Aggarwal, 2015). Time series might suffer from data gaps due to various reasons such as receiver malfunctions and problems in power supply. The interpolated data can lead to spurious conclusions, as the data gap becomes longer. Non-tectonic effects might be seen due to, e.g., environmental changes around the antenna, vandalism, heavy snow load on the antenna.

Transient signals from tectonic origins, which are of main interest in this thesis, might also exist in the time series. Studies about tectonic transients include, e.g., postseismic deformation (e.g., Savage and Langbein, 2008; Xu et al., 2019; Gunawan et al., 2019), hydrologic deformation (e.g., Ji and Herring, 2012; Silverii et al., 2019), volcanic inflation (e.g., Chang et al., 2007; Ji et al., 2017) and slow slip events (e.g., Szeliga et al., 2008; Vergnolle et al., 2010).

It is important to have knowledge of the noise characteristics in GPS time series to evaluate the significance of the detected transient signals. It has been shown in several studies that GPS time series contain temporally correlated noise (e.g., Zhang et al., 1997; Mao et al., 1999; Williams et al., 2004; Beavan, 2005; Amiri-Simkooei et al., 2007; Langbein, 2008; Santamaria-Gomez et al., 2011; Wang et al., 2011). Power spectra,  $S(f)$ , of the noise in GPS time series obey a power-law model well (e.g., Williams et al., 2004) as:

$$S(f) \cong 1/f^\alpha, \quad (1.1)$$

where  $f$  is frequency, and  $\alpha$  is spectral index (Mandelbrot and Van Ness, 1968; Agnew, 1992). When noise is white,  $\alpha = 0$ ; while flicker noise and random-walk correspond to  $\alpha = 1$  and  $\alpha = 2$ , respectively. According to Zhang et al. (1997) and Mao et al. (1999), combination of white and flicker noise is the best choice to describe the noise in GPS time series. Williams et al. (2004) states the more varied nature of the spectral index in regional solutions. Langbein (2008) found that either flicker or random-walk noise can represent one-half of the time series examined from 236 GPS sites. Flicker plus random-walk, power law, first-order Gauss-Markov plus random walk, power law plus broadband, and seasonal noise were the descriptors of the noise in the remaining time series.

Possible site-specific sources of correlated noise might be due to, e.g., satellite geometry, multipath, and monument instability. Random-walk type errors are introduced to the time series due to the random motion of the monuments with respect to the deeper crust (Johnson and Agnew, 1995). Anchoring to more than 10-m depth might mitigate the monument instability (Wyatt, 1989). However, most of the CORS-TR stations are installed on the roofs or terraces of buildings, considering operational convenience.

In addition to the temporally correlated noise, GPS time series are also exposed to spatially correlated noise. Since such noise is common to the sites in the network rather than being site-specific, it is called “Common Mode Error” (CME). Possible causes of CME might be errors of satellite orbits and reference frame (Wdowinski et al., 1997; Dong et al., 2006). CME can be reduced by regional filtering approach (Wdowinski et al., 1997) in which epochwise mean values of the stacked residuals are removed from the individual positions. This approach works well when the assumption of spatial uniformity of CME holds. It is equivalent to translating the origin of the network in three dimensions (Dong et al., 2006). Spatiotemporal

filtering of Dong et al. (2006) utilizes PCA and Karhunen-Loeve expansion and allows non-uniformity in the estimation of CME. Transforming the reference frame by a seven-parameter Helmert transformation into a regional reference frame using fiducial local sites is another approach to suppress the CME (Ji and Herring, 2011).

In a network, a tectonic transient often reveals itself in multiple sites. However, since the sites to be investigated in transient signal detection are not known a priori, inspecting all sites becomes challenging as the network size grows. Yet, especially in noisy data, the weakness of the transient is the major difficulty in detection. Hence, signal-to-noise ratio (SNR) of the original signal must be improved. This can be achieved by suppressing the noise. To this end, the level and the stochastic nature of the noise must be determined well. However, there is no ubiquitous noise model for GPS time series since the correlated noise is site-specific as aforementioned. Based on their findings on the majority of the time series they inspect, researchers try to reach an approximation. Since the validity of these approximations are arguable, the methods of adaptive data-driven Empirical Mode Decomposition (EMD) (Huang et al., 1998), its noise-assisted version Ensemble Empirical Mode Decomposition (EEMD) (Wu and Huang, 2009) and Complete EEMD with Adaptive Noise (CEEMDAN) (Torres et al., 2011), which is the complete variant of EEMD, are applied here, for denoising the GPS residual time series. Hereby, no a priori assumptions are made about the noise like, e.g., in Ji and Herring (2011), where they used a first-order Gauss-Markov (FOGM) process to account for temporally correlated noise and transients, due to its easy implementation in Kalman filters.

EMD decomposes the noisy signal into amplitude and frequency modulated Intrinsic Mode Functions (IMFs). Each IMF contains higher frequency oscillations than the following IMF components. Denoising properties of EMD were reported in, e.g., Wu and Huang (2004), Flandrin et al. (2004, 2005) and Boudraa and Cexus (2006). Since

then, signal denoising through EMD was applied in various fields (e.g., Weng et al., 2006; Khaldi et al., 2008; Tsolis and Xenos, 2009). Lately, Li et al. (2018) combined CEEMD and Wavelet-Transform (WT) based multiscale multiway Principal Component Analysis (Li et al., 2017) for denoising GNSS time series.

Fractional Brownian motion (fBm) has long-range, temporal and spatial correlation unlike the classical Brownian motion with independent increments. This makes fBm a convenient model for complex natural processes such as long GPS time series. The Fractional Gaussian noise, fGn, (Mandelbrot and Van Ness, 1968) is the increment process of fBm and a widely used model for broadband noise with no dominant frequency band. The self-similarity parameter Hurst index ( $H$ ), determines the statistical properties of fGn. When  $H = 0.5$ , the process is uncorrelated. If  $H < 0.5$ , the process shows short-range dependence, while it exhibits long-range dependence if  $H > 0.5$ . The relationship between  $H$  and  $\alpha$  (spectral index of power-law model) is as follows (Schroeder, 2009):

$$\alpha = 2H - 1, \quad (1.2)$$

where  $\alpha \leq 2$ . Flandrin et al. (2004) carried out extensive simulations and examined the behavior of IMF energies in noise-only situations (where  $0.1 \leq H \leq 0.9$ ). From this point of view, the residuals are denoised in this study by subtracting only the IMFs whose Hurst indexes are below or equal to  $0.5$  (white noise). It is not attempted to remove the IMFs with higher  $H$  indexes which correspond to colored noise, to avoid losing also the traces of the transients.

The Common Mode Error (CME) is first reduced by applying a reference frame transformation. To discriminate between the site-specific colored noise and the

transients in the denoised residual time series, the spatial coherence of the transients is sought. Principal Component Analysis (PCA) (e.g., Jolliffe, 2002; Abdi and Williams, 2010) is applied to the denoised residuals to detect this coherence. PCA transforms the time series into linearly uncorrelated principal components (PCs). Considering also the reduction of the CME beforehand, it is expected to catch the coherent transients in the first PC which has the largest variance, and a  $\chi^2$  value significantly inconsistent with the simply random noise.

The spectrum of time series analysis methods is very wide (see, e.g., [https://en.wikipedia.org/wiki/Time\\_series](https://en.wikipedia.org/wiki/Time_series)). There are tens of methods which are used for various purposes such as, forecasting, classification and prediction, as well as signal detection. The primary motivation of this study is to develop a novel method which combines the high-precision GPS analysis, Empirical Mode Decomposition and Principal Component Analysis to detect the tectonically driven transient signals in GPS time series, effectively. High-precision GPS analysis sets the basis for weak and transient signal detection by modeling the other signals which can mask the targeted signal. The adaptive nature of EMD makes it possible to improve the SNR effectively without the a priori assumptions about the data. The patterns which are normally not easily discernible in the original data can be identified by PCA. The developed method can be used by Earth science community for tectonic monitoring where the weak transient signals are of significance.

## **1.2 Objectives**

We primarily aim at realizing a tool for transient signal detection in GPS coordinate time series. This is going to be achieved by reducing CME and improving the signal-to-noise ratio both in time and space domain without making any assumption about

the noise characteristics of the targeted time series. The following research objectives are considered to reach this goal:

- Daily GPS phase data from CORS-TR stations are going to be processed with the high-precision analysis techniques, and the coordinate time series in north, east and up directions are going to be generated. Known signals such as secular velocities, seasonal signals, coseismic displacements due to known earthquakes, non-tectonic signals due to, e.g., antenna change, are going to be determined. Outliers are going to be removed and data gaps are going to be interpolated. Precise velocities and uncertainties of the sites are going to be estimated.
- Sufficient number of homogeneously distributed local stations with low coordinate and velocity uncertainties are going to be selected. Based on the coordinates of these stations, reference frame of the time series is going to be transformed into a regional frame by using a seven parameter Helmert Transformation, and CME is going to be reduced.
- GPS time series are going to be detrended, considering the secular rates and seasonal signals. Residual signals are going to be denoised using Empirical Mode Decomposition.
- Transient signals are going to be investigated in the denoised residuals by decomposing them into principal components using Principal Component Analysis.



- Detection capability of the proposed method is going to be displayed on slow slip events in Cascadia, a known transient in Plate Boundary Observatory (PBO) network due to inflation at Akutan volcano, Alaska, and on postseismic deformation at CORS-TR sites after October 23, 2011 Van earthquake.

### 1.3 Thesis Outline

The structure of the thesis is as follows:

- **Chapter 1, Introduction:** The motivation, objectives and thesis outline are introduced.
- **Chapter 2, The Global Positioning System and Coordinate Time Series:** Theoretical bases of high-precision GPS analysis are presented. Examples of common signals in GPS time series, and noise characteristics are also displayed.
- **Chapter 3, Empirical Mode Decomposition:** Fundamentals of Empirical Mode Decomposition (EMD) method are introduced. Problematic areas of EMD are touched. Signal denoising approach is presented.
- **Chapter 4, Principal Component Analysis:** Mathematical foundations of Principal Component Analysis (PCA) are given.
- **Chapter 5, Applications:** Details and results in the processing of CORS-TR GPS data are illustrated. Common mode error is reduced. Detection capability

of the proposed method is shown on previously known transient signals in Cascadia, Alaska and Turkey.

- **Chapter 6, Conclusions:** Discussion, conclusions and future work are included.

## **CHAPTER 2**

### **GLOBAL POSITIONING SYSTEM AND COORDINATE TIME SERIES**

The Global Positioning System (GPS) segments and GPS signals are first presented in the next subsections. GPS observables and positioning principles are explained afterwards. Data processing software used and high-precision positioning standards are introduced next. Examples of various signals seen in the time series of the station positions, as well as the noise characteristics are illustrated in the end.

#### **2.1 GPS Segments**

##### **2.1.1 Space Segment**

The space segment includes 31 operational GPS satellites (as of January 9, 2019). These satellites rotate around the Earth in almost circular orbits of approximately 26600 km radius with the Earth's centre of mass being at the centre. They transmit signals towards the Earth using microwaves, which are used for ranging between the satellites and the receiver. Signals are encoded with the navigation messages which include orbit parameters (broadcast ephemeris) to be used in the calculation of the satellites' positions. In high-precision analysis, more precise orbit information is used, supplied by, e.g., International GNSS Service (IGS).

The design of the GPS constellation has some consequences, desirable or not. First of all, anytime and anywhere on the Earth, at least four satellites are visible. On the other hand, a GPS satellite completes its revolution in the orbit in approximately 11 h 58 min. Satellites are placed in six fixed orbital planes with  $55^\circ$  inclination over the equator. Therefore, same set of satellites are observed by a user at the same location everyday with a 4 min. delay. Such geometry can cause repeating errors, such as multipath interference which is due to signals reflected by the objects around the antenna. Since the observations are biased consistently, coordinate repeatabilities are not intriguing, although the accuracy is degraded. Fixed orbital planes with  $55^\circ$  inclination also causes GPS satellites never rise above  $55^\circ$  elevation at the poles, which leads to lower vertical positioning accuracy at these regions (Blewitt, 2009).

### **2.1.2 Control Segment**

The control segment monitors the satellite orbits and the health of the satellites, maintains GPS time, predicts and updates satellite ephemerides and clock parameters (Misra and Enge, 2006). It consists of several globally distributed monitor stations (MS), a master control station (MCS) with an alternate, and ground antennas (GA).

Monitor stations determine the range data by tracking the GPS satellites. They send the observations together with the local atmospheric data to the master control station. Using these data, master control station computes the satellite positions and satellite clock behaviors, and forms the navigation message, which later uplinked to the satellites by ground antennas. This process is shown in Figure 2.1.

### 2.1.3 User Segment

The user segment includes GPS receivers and antennas, as well as the software used for data processing. A GPS receiver collects signals from the satellites and convert them to the observables which are used in the calculation of the positions. They can be classified according to various criteria, such as available data-type, channel realizations and intended use. Design of the geodetic antennas generally serves for high-precision, such that they receive both L1 and L2 carriers which can be used together in the removal of ionospheric effect, and can be protected against multipath.

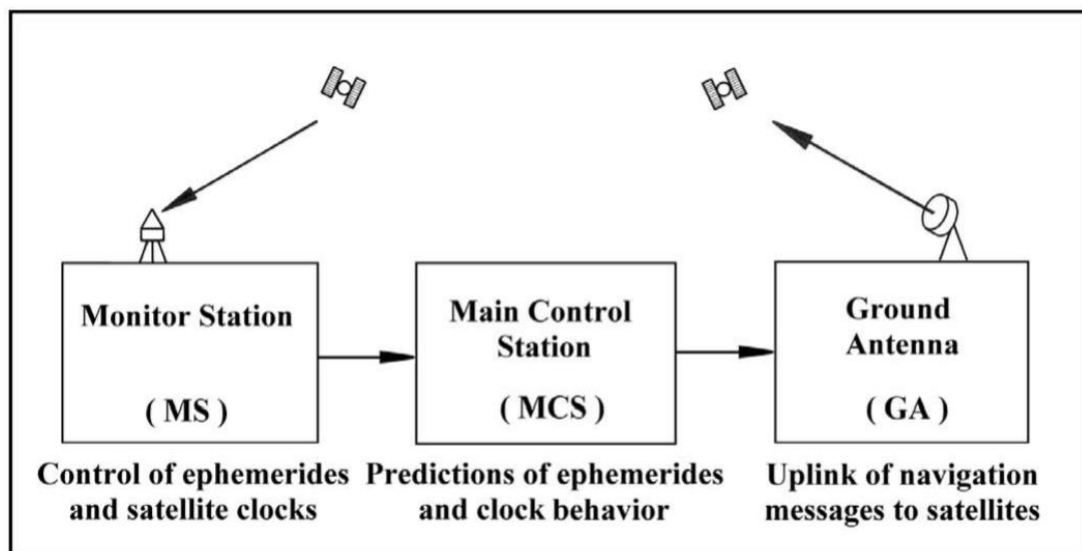


Figure 2.1. Navigation message cycle (Seeber, 2003)

Generally, scientific software packages are used in post-processing mode in the applications which require ultrahigh-precision. Such softwares, in addition to the employment of an accurate observation model, have extended capabilities in modeling and incorporating many phenomena which might affect positioning precision. Three widely used packages are as follows:

- GAMIT-GLOBK software, Massachusetts Institute of Technology (MIT), USA (Herring et al., 2018),
- BERNESE software, Astronomical Institute, University of Bern, Switzerland (Dach et al., 2015),
- GIPSY-OASIS II software, Jet Propulsion Laboratory (JPL), California Institute of Technology, USA (Zumberge et al, 1997).

## 2.2 GPS Signal Structure

The fundamental frequency of GPS signals is 10.23 MHz, provided by the precise atomic clocks. Two main *L*-band carrier signals are generated from this signal:

- *L1*:  $154 \times 10.23 = 1575.42$  MHz
- *L2*:  $120 \times 10.23 = 1227.60$  MHz

As of January, 2019, twelve operational Block IIF satellites, launched between 2010 and 2016, transmit also *L5* signal of 1176 MHz. The carriers are encoded with information using binary digits (code) showing whether the signal remains unchanged (0) or flipped by  $180^\circ$  (1). There exist C/A (coarse acquisition) code transmitted at 1.023 Mbps on *L1* channel and P (precise) code transmitted at 10.23 Mbps on both *L1* and *L2* channel. Both codes (with different resolution) convey satellite clock time of signal transmission. *L2* carriers from the satellites, launched since 2005, are also encoded with *L2C* code. The navigation message which contains information about orbital parameters, ionosphere, satellite clock corrections, satellite health status and almanac, is encoded on *L1* channel and transmitted at 50 bps.

## 2.3 GPS Observables and Parameter Estimation

### 2.3.1 Code Pseudorange Observable

Determining the position of a point with GPS mainly depends on measuring distances (ranges) to the satellites of known positions. However, these ranges cannot be measured directly by the GPS receivers. Instead, signal's time of flight between transmission from the satellite and reception in the receiver is measured. To this end, the receiver generates the replica of the satellite-specific C/A and P codes, compares them with the incoming codes by cross-correlation, and computes the time delay required in the alignment of the codes. This time measurement is multiplied by the speed of light (299792458 m/s), and the so-called pseudorange is obtained. The term 'pseudo' is due to the bias in the range introduced by the receiver's clock. Although this bias is receiver-specific, it is the same for all satellites in view. Thus it can be estimated together with the three unknown coordinates of the receiver in the positioning solution. The information about much smaller errors in the satellite clocks are transmitted through navigation messages.

The basic equation of a pseudorange to the satellite  $s$  is:

$$\begin{aligned} P^s(t) &= (t - t^s)c + c\tau - c\tau^s \\ &= \rho^s(t, t^s) + c\tau - c\tau^s, \end{aligned} \quad (2.1)$$

where  $t$  is the time of signal reception,  $t^s$  is the time of signal transmission,  $\tau$  is the receiver clock bias,  $\tau^s$  is the satellite clock bias,  $c$  is the speed of light, and  $\rho^s(t, t^s)$  is the range (geometric distance) which can be written from Pythagoras Theorem as:

$$\rho^s(t, t^s) = \sqrt{(x^s(t^s) - x(t))^2 + (y^s(t^s) - y(t))^2 + (z^s(t^s) - z(t))^2}, \quad (2.2)$$

where  $x$ ,  $y$  and  $z$  are the receiver coordinates, whereas  $x^s$ ,  $y^s$  and  $z^s$  are the satellite coordinates. Satellite coordinates and satellite clock bias are computed by means of the navigation message. Hence, the three components of the receiver's position and the receiver clock bias are the unknowns left. Therefore, observation equations for at least four satellites in view are formed to calculate the unknowns. Code pseudorange observation model might be improved more by including the signal delay due to troposphere ( $Z_A^j$ ) and ionosphere ( $I_A^j$ ) (Blewitt, 2002):

$$P_A^j(T_A) = c(T_A - T^j) = \rho_A^j(t_A, t_j) + c\tau_A - ct^j + Z_A^j + I_A^j, \quad (2.3)$$

where subscript  $A$  indicates the receiver quantities, and superscript  $j$  indicates the satellite quantities.

### 2.3.2 Carrier Phase Observable

Carrier phase observable is used to reach higher precision in positioning. It is the difference between the phases of the incoming carrier and a reference signal generated by the receiver. The meaning of phase ( $\varphi$ ) is illustrated in Figure 2.2. Carrier phase observable is multiplied by the wavelength of the carrier, and a biased distance to the satellite is obtained. The observation model is similar to that of the code pseudorange:

$$\begin{aligned} L_A^j(T_A) &\equiv \lambda_0 \phi_A^j(T_A) \\ &= \rho_A^j(t_A, t_j) + c\tau_A - ct^j + Z_A^j - I_A^j + B_A^j, \end{aligned} \quad (2.4)$$



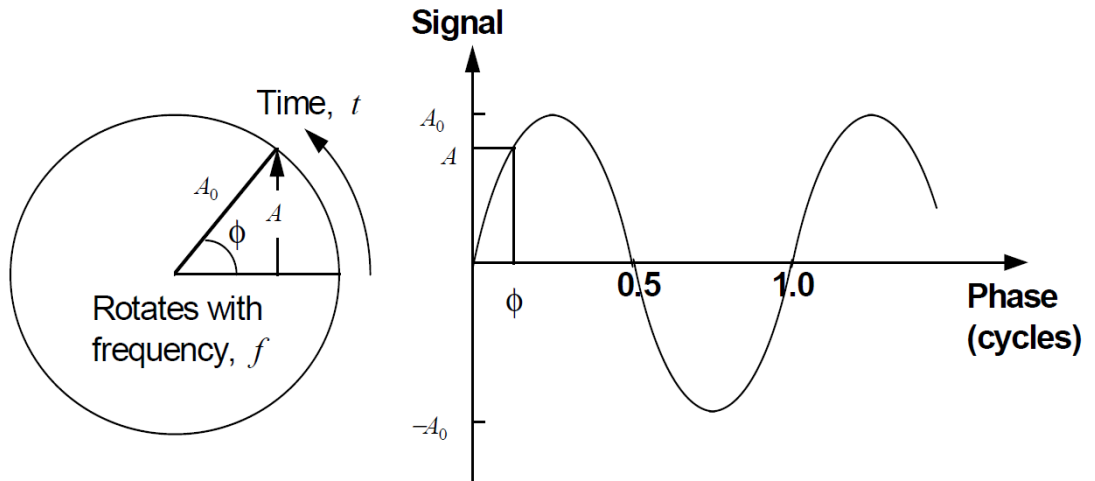


Figure 2.2. The definition of the phase (Blewitt, 2002)

where  $\lambda$  is the wavelength of the carrier  $L_A$ , and  $B_A^j$  is the carrier phase bias (Blewitt, 2002) as follows:

$$B_A^j \equiv \lambda_0(\varphi_{0A} - \varphi_0^j - N_A^j), \quad (2.5)$$

where  $N_A^j$  is the integer number of cycles (wavelengths) between the satellite and the receiver, which is ambiguous initially, since only the fractional phase is recorded rather than the total phase. Ambiguity resolution techniques are used to resolve this bias (for an overview of ambiguity resolution techniques, see, e.g., Hoffman-Wellenhof et al. (2008)). The integer ambiguity can be modeled as constant for all measurements, for the receiver counts the full signal oscillations since the first measurement. However, if the lock on a satellite is lost for any reason, the count of the complete cycles is restarted, and a new integer ambiguity is introduced. The name of this integer discontinuity is “cycle-slip”. Cycle-slips can be removed by, e.g., triple-

differencing (e.g., Seeber, 2003; Hoffman-Wellenhof et al., 2008). For the sake of integrity, let us now explain the differencing techniques.

The observation model of a carrier phase between the receiver  $A$  and satellite  $j$  has already been introduced. A similar carrier phase can be formed between the receiver  $B$  and the same satellite  $j$ . The single difference phase  $\Delta L_A^j$  is the difference between these two phase observables:

$$\begin{aligned}\Delta L_A^j &\equiv L_A^j - L_B^j \\ &= \Delta \rho_{AB}^j + c\Delta \tau_{AB} + \Delta Z_{AB}^j - \Delta I_{AB}^j + \Delta B_{AB}^j.\end{aligned}\quad (2.6)$$

As can be seen, the parameter relating to the satellite clock bias is eliminated in the above equation, which is actually the purpose of single differencing.

The above single difference phase can also be constructed for another satellite  $k$ . If the difference between these two single difference phases is taken, the double difference phase is reached:

$$\begin{aligned}\nabla \Delta L_{AB}^{jk} &\equiv \Delta L_{AB}^j - \Delta L_{AB}^k \\ &= \nabla \Delta \rho_{AB}^{jk} + \nabla \Delta Z_{AB}^{jk} - \nabla \Delta I_{AB}^{jk} + \nabla \Delta B_{AB}^{jk}.\end{aligned}\quad (2.7)$$

The aim of generating double differences is to eliminate receiver clock bias, as the above equation exhibits clearly.

Assuming that the integer ambiguity remains constant between epochs, triple differencing can be used to eliminate the ambiguity (Blewitt, 2002). Triple difference

phase is the difference between two double difference phase at two successive epochs ( $i, i+1$ ):

$$\begin{aligned}
\delta(i, i + 1)\nabla\Delta L_{AB}^{jk} &\equiv \nabla\Delta L_{AB}^{jk}(i + 1) - \nabla\Delta L_{AB}^{jk}(i) \\
&= \delta(i, i + 1)\nabla\Delta\rho_{AB}^{jk}(i) + \delta(i, i + 1)\nabla\Delta Z_{AB}^{jk}(i) \\
&\quad - \delta(i, i + 1)\nabla\Delta I_{AB}^{jk}(i).
\end{aligned} \tag{2.8}$$

Note also the negative sign of the ionospheric delay in carrier phase observations, due to the increase in the phase velocity. The ionospheric refraction bias can be eliminated by constructing a linear combination ( $LC$ ) of the carrier phases (so-called ionosphere-free combination):

$$\begin{aligned}
LC &= \frac{f_1^2 L1 - f_2^2 L2}{(f_1^2 f_2^2)} \\
&\cong 2.546L1 - 1.546L2,
\end{aligned} \tag{2.9}$$

where  $f_1 = 154$  and  $f_2 = 120$ .

Combinations cannot eliminate the tropospheric delay, since it is frequency-independent. The influence of the troposphere on the observed ranges is usually expressed by dry and wet components. The distribution of the water vapor in the atmosphere governs the wet portion. The main contributor to the total tropospheric refraction is the dry component (Seeber, 2003). Further information about the available models for the tropospheric delay can be found in, e.g., (Mendes and Langley, 1994, 1999).

### 2.3.3 Least Squares Estimation

To determine the unknowns (e.g., the receiver coordinates and the receiver clock bias), the observation equations are linearized first, followed by applying ordinary least-squares analysis. The linearized model between the observations ( $\mathbf{y}$ ) and the unknowns ( $\boldsymbol{\beta}$ ), and the stochastic part of the model (together called Gauss-Markoff model) can be written as:

$$\Delta \mathbf{y}_{nx1} + \mathbf{e}_{nx1} = \mathbf{X}_{nxu} \Delta \boldsymbol{\beta}_{ux1}, \quad (2.10)$$

$$\mathbf{D}(\mathbf{y}) = \sigma^2 \mathbf{P}^{-1}, \quad (2.11)$$

where  $\Delta \mathbf{y}$  is the reduced observations (prefit residuals) vector,  $\mathbf{e}$  is the random observation errors vector,  $\mathbf{X}$  is the coefficient matrix formed by taking the partial derivatives of the function according to the unknowns,  $\Delta \boldsymbol{\beta}$  is the correction vector of the unknowns,  $\mathbf{D}(\mathbf{y})$  is the covariance matrix of the observations,  $\mathbf{P}$  is the data weight matrix,  $\sigma^2$  is the variance of unit weight,  $n$  is the number of linearly independent double differenced data,  $u$  is the number of the unknowns. Corrections to the unknowns are calculated using the least squares estimation method (details of the least squares estimation can be found in, e.g., Koch, 1999):

$$\Delta \hat{\boldsymbol{\beta}} = (\mathbf{X}^T \mathbf{P} \mathbf{X})^{-1} \mathbf{X}^T \mathbf{P} \Delta \mathbf{y}. \quad (2.12)$$

Adjusted parameters and corrected observations are obtained as follows:

$$\hat{\boldsymbol{\beta}} = \boldsymbol{\beta}_0 + \Delta \hat{\boldsymbol{\beta}}, \quad (2.13)$$

$$\hat{\mathbf{y}} = \mathbf{X} \hat{\boldsymbol{\beta}}. \quad (2.14)$$

Estimated residuals (postfit residuals) are the differences between the original observations and the corrected observations:

$$\hat{\mathbf{e}} = \mathbf{y} - \hat{\mathbf{y}}. \quad (2.15)$$

The covariance matrix of the estimated parameters is:

$$\mathbf{D}(\hat{\boldsymbol{\beta}}) = \hat{\sigma}_0^2 (\mathbf{X}^T \mathbf{P} \mathbf{X})^{-1}, \quad (2.16)$$

where the variance scale factor, which is a measure of fitting, is:

$$\hat{\sigma}_0^2 = \frac{\hat{\mathbf{e}}^T \mathbf{P} \hat{\mathbf{e}}}{n-u}. \quad (2.17)$$

## 2.4 High-precision GPS Positioning

Measuring pseudoranges at a single station to the satellites in view (which is called absolute positioning) enables users to reach only couple meters of positioning accuracy. The Precise Point Positioning (PPP) technique, which relies on the dual-frequency measurements at a single station and precise GPS orbit and clock products, has been used successfully to achieve centimeter/decimeter level of accuracy (e.g., Zumberge et al., 1997; Gao and Shen, 2002), and applied in various areas (e.g., Kuo et al., 2012; Li et al., 2015). PPP is implemented in post-processing mode conventionally, due to the latency of the precise products provided by IGS and several other agencies. Real-time PPP is a hot topic in the geodetic community, and IGS provides precise orbit and clock products through its Real-Time Service (RTS) since

2013 via NTRIP (Network Transport of Radio Technical Commission for Maritime (RTCM) via Internet Protocol) (Colombo, 2008), to contribute real-time applications.

Absolute positioning with PPP using precise orbit and clock products (1), relative positioning of networks using precise orbits, but estimating the clock biases (2), and relative positioning of networks by double-differenced observations, using again precise orbits (3), all produce similar results of high-precision and therefore are common in geophysical studies (Blewitt, 2009). The points taken into consideration in high-precision GPS analysis are summarized as follows:

- For geodetic applications precise satellite orbits and clocks are needed. These data might be obtained from the dedicated services such as IGS which is the fruit of an international collaboration. As of May 2019, the claimed accuracies of the IGS GPS products are given in Table 2.1.
- Dual-frequency GPS receivers are required to eliminate the ionospheric delay errors, by combining the carrier phases appropriately.
- Simultaneous observations at different ground stations are needed to construct differenced data which might be used in, e.g., cancelling out the receiver clock bias.
- Positioning precision increases with longer observation sessions (Eckl et al., 2001; Soler et al., 2006; Firuzabadi and King, 2011). Since the measurements are uninterrupted in permanent GPS stations, positions can be determined using the data with sub-daily intervals. However, it is common to estimate the positions by using 24-h data packages (and generally with 30-s data sampling) in geophysical studies.

Table 2.1. IGS GPS products (<http://www.igs.org/products>)

Type		Accuracy	Latency	Updates	Sample Interval
Broadcast	orbits	~100 cm	real time	--	daily
	Sat. clocks	~5 ns RMS ~2.5 ns SDev			
Ultra-Rapid (predicted half)	orbits	~5 cm	real time	at 03, 09, 15, 21 UTC	15 min
	Sat. clocks	~3 ns RMS ~1.5 ns SDev			
Ultra-Rapid (observed half)	orbits	~3 cm	3 - 9 hours	at 03, 09, 15, 21 UTC	15 min
	Sat. clocks	~150 ps RMS ~50 ps SDev			
Rapid	orbits	~2.5 cm	17 - 41 hours	at 17 UTC daily	15 min
	Sat. & Stn. clocks	~75 ps RMS ~25 ps SDev			5 min
Final	orbits	~2.5 cm	12 - 18 days	every Thursday	15 min
	Sat. & Stn. clocks	~75 ps RMS ~20 ps SDev			Sat.: 30s Stn.: 5 min

**Note 1:** Orbit accuracies are 1D mean RMS values over the three XYZ geocentric components. IGS accuracy limits, except for predicted orbits, are based on comparisons with independent laser ranging results and discontinuities between consecutive days. The precision is better.

**Note 2:** The accuracy (neglecting any contributions from internal instrumental delays, which must be calibrated separately) of all clocks is expressed relative to the IGS timescale, which is linearly aligned to GPS time in one-day segments. The standard deviation (SDev) values are computed by removing a separate bias for each satellite and station clock, whereas this is not done for the RMS values.

- A sophisticated geodetic software is used in the estimation of the model parameters. It utilizes an accurate observation model and considers modeling of, e.g., Earth rotation, atmosphere, solid Earth and ocean tides, atmospheric pressure loading, antenna phase center variations. It must also detect and correct the cycle-slips, and resolve the integer ambiguities.

## 2.5 GPS Time Series

Processing the data and computing the station coordinates daily is the initial step of producing the time series. Geodetic time series might serve in reflecting phenomena related to oceanography, hydrology, glaciology, meteorology, and geophysics which are the sciences having close connection to geodesy (Torge and Müller, 2012). Changes in the position are the consequences and interactions of the tectonic or non-tectonic factors as well as the correlated noise, revealing themselves in the time series with miscellaneous characteristics. Various types of signals which are commonly present in GPS time series are displayed in this subsection. Examples are from CORS-TR time series which are the main interest of this thesis.

The most immanent pattern, especially in the horizontal components of the time series, is the secular velocities originated mostly from the constant motions of the rigid plates according to the plate tectonic theory (e.g., Tomecek, 2009). The reasons of the vertical velocities are not so clear. High rates in the vertical component are often indicatives of local events. Annual and semi-annual seasonal signals might be present in the time series due to, e.g., ocean tide and atmospheric loadings (see Figure 2.3).

There might exist discontinuities due to, e.g., updates in processing strategy or equipment changes (antenna, radome etc.). Outliers due to systematic errors, e.g., adverse atmospheric conditions, might contaminate the time series. Time series might suffer from data gaps due to various reasons, such as receiver malfunctions and problems in power supply (see Figure 2.4).



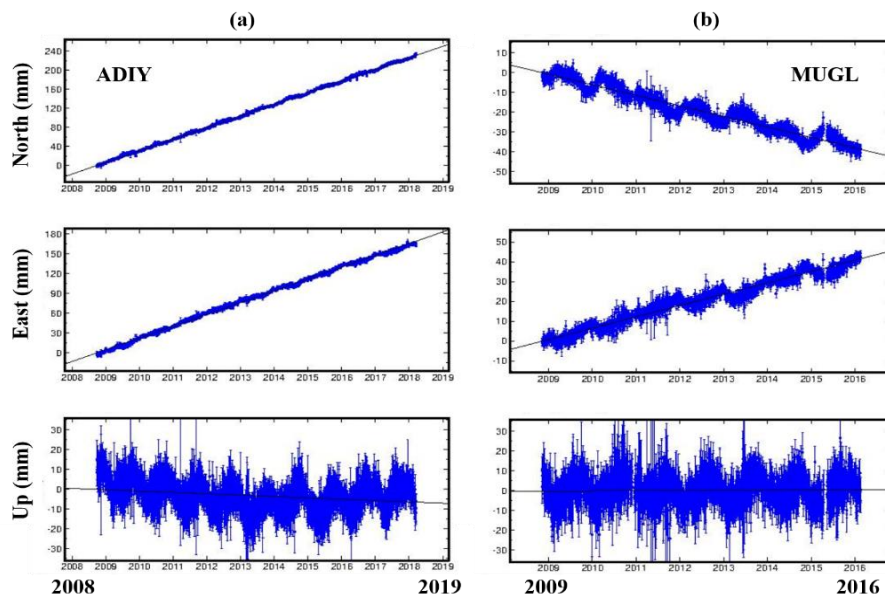


Figure 2.3. Daily GPS time series of (a) ADIY and (b) MUGL stations. Secular velocities are shown by the line fits. Often, seasonal signals exist in the time series as can be seen in (b).

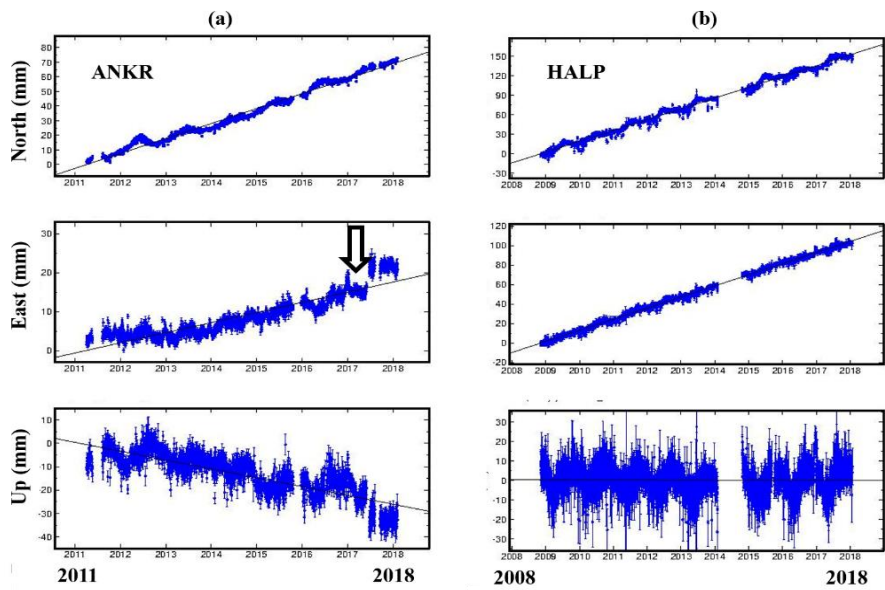


Figure 2.4. (a) The offset highlighted by the arrow in the east component of ANKR station occurred due to antenna and receiver change. (b) Outliers and data gap are shown in the time series of HALP station.

In addition to these common patterns, there might be also tectonically driven transient signals. In Figure 2.5, the coseismic displacement and postseismic deformation following the October 23, 2011 Van earthquake at MURA station, and hydrologic deformation at ADAN station which is located very close to Seyhan River (< 500m) and correlated with the water level change at the Seyhan Dam (Ozdemir et al., 2017) are presented.

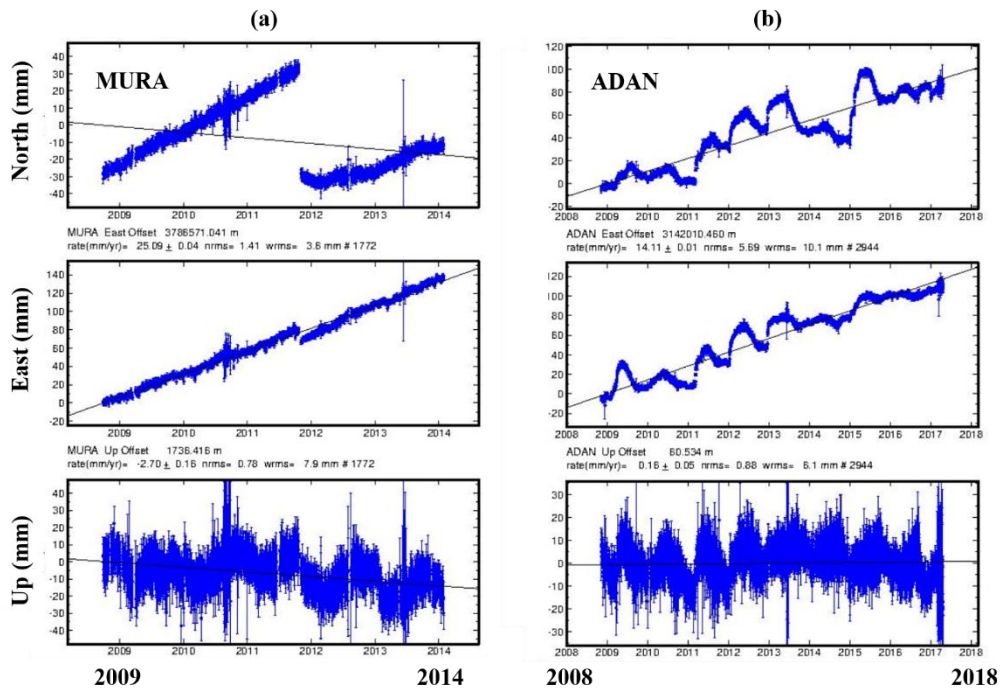


Figure 2.5. (a) Coseismic displacement and postseismic deformation observed at MURA station following October 23, 2011 Van earthquake, (b) Hydrologic deformation observed at ADAN station correlated with the water level change at the nearby Seyhan Dam.

The time series of KNY1 station is displayed in Figure 2.6, which suffers from the land subsidence in Konya, detected also by Ustun et al. (2015). Its intolerable up velocity is about 6.5 cm/yr.

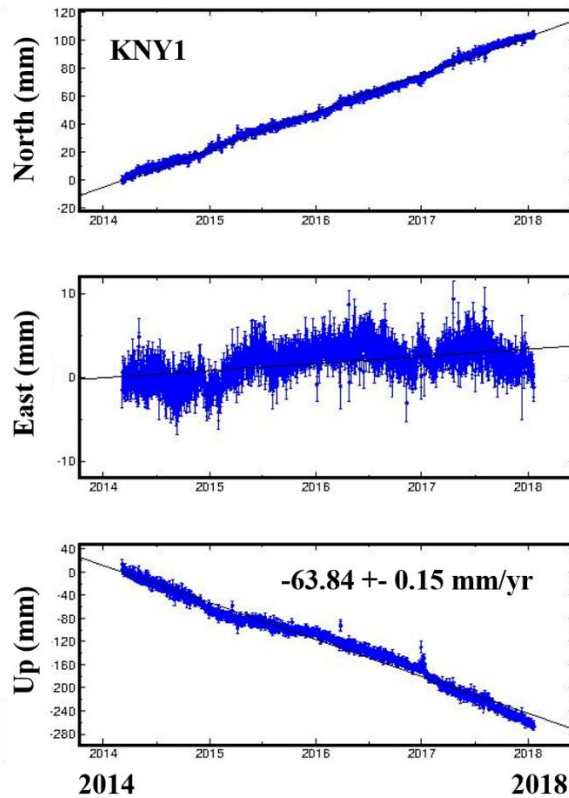


Figure 2.6. Time series of KNY1 station whose up velocity is about 6.5 cm/yr, indicative of a possible land subsidence.

Tectonics is not the only source of transient signals in GPS time series. Many non-tectonic signals, due to such as human interaction, antenna malfunction, changes in the environment around the antenna, repeating heavy snow cover during winters, multipath, water vapor effect in summers may also affect the time series. In Figure 2.7, the effect of the repeating multipath during summer seasons at BTMN station is demonstrated. It is also shown in the same figure the time series of EMIR station which deviates from its regular pattern during late 2013, since a lightning rod had been mounted on the mast (see Figure 2.8) of this site. Time series returned to its former pattern after the removal of the rod at January 09, 2014.

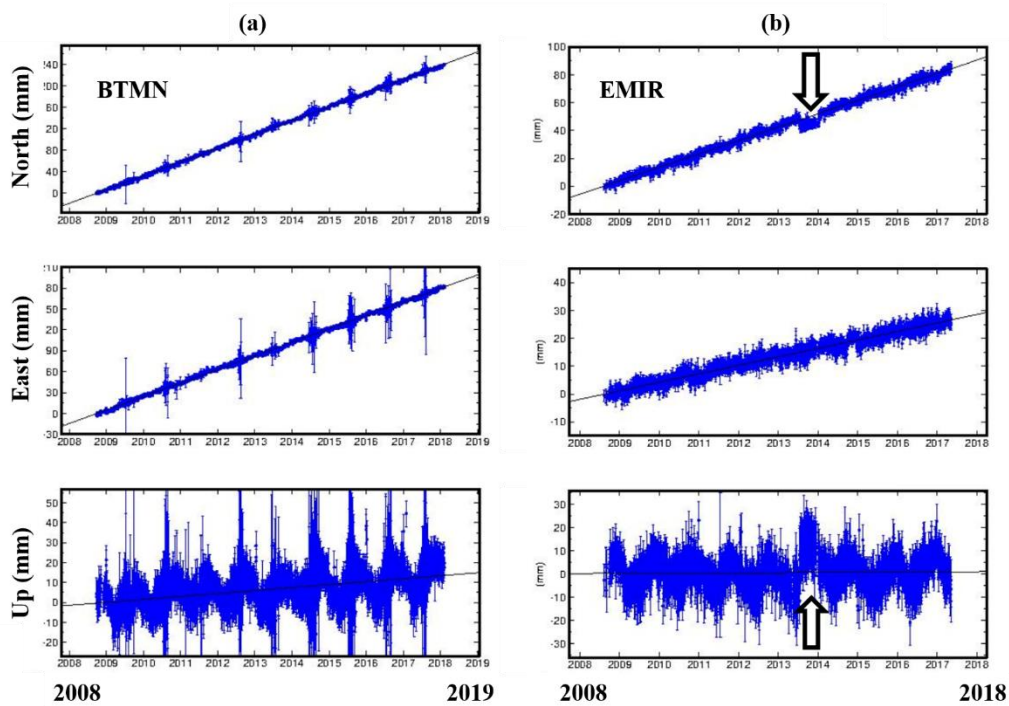


Figure 2.7. (a) Time series of BTMN station showing repeating signal during summer season due to multipath, (b) The effect of a lightning rod mounted on the mast of the GPS antenna of EMIR station (see also Figure 2.8).



Figure 2.8. Lightning rod mounted on the mast of the GPS antenna at EMIR station.

There might be also obvious signals in the time series whose sources could not have been discovered yet. Two such signals at INEB and SEMD stations are presented in Figure 2.9, respectively. INEB station had been relocated twice, due to a repeating pattern occurring every year between June and late October. A severe jump happens at the beginning of 2016 at SEMD station, very similar to a coseismic displacement. However, no earthquake has been detected which can cause such a displacement on these days.

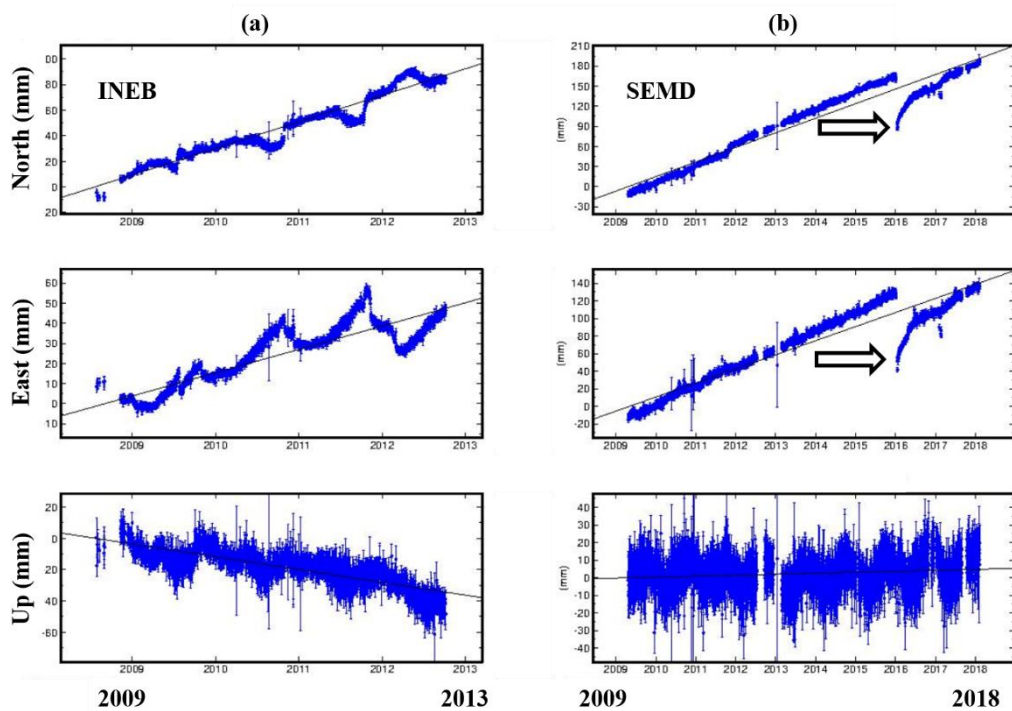


Figure 2.9. (a) Time series of INEB station showing unknown repeating signal between June and late October every year, (b) Unknown displacements (indicated by an arrow) seen in the time series of SEMD station.

In addition to these several types of signals, GPS time series also contain temporally and spatially correlated noise. Contrary to what is believed previously, studies in the

last two decades have shown that noise in GPS time series cannot be assumed simply white in time, but also exhibits colored characteristics (e.g., Zhang et al., 1997; Mao et al., 1999; Williams et al., 2004; Beavan, 2005; Amiri-Simkooei et al., 2007; Langbein, 2008; Santamaria-Gomez et al., 2011; Wang et al., 2011). Although reasons of correlated noise are not so clear, satellite geometry, multipath, and monument instability might be regarded as the possible sources.

Power spectra,  $S(f)$ , of the noise in GPS time series obey a power-law model well (e.g., Williams et al., 2004) as:

$$S(f) \cong 1/f^\alpha, \quad (2.18)$$

where  $f$  is frequency, and  $\alpha$  is spectral index (Mandelbrot and Van Ness, 1968; Agnew, 1992). When noise is white,  $\alpha = 0$ , while flicker noise and random-walk correspond to  $\alpha = 1$  and  $\alpha = 2$ , respectively. According to Zhang et al. (1997) and Mao et al. (1999), combination of white and flicker noise is the best choice to describe the noise in GPS time series. Williams et al. (2004) states the more varied nature of the spectral index in regional solutions, possibly due to local conditions. Langbein (2008) found that either flicker or random-walk noise can represent one-half of the time series examined from 236 GPS sites. Flicker plus random-walk, power law, first-order Gauss-Markov plus random walk, power law plus broadband, and seasonal noise were the descriptors of the noise in the remaining time series (see Table 2.2).

GPS time series suffer from the spatially correlated noise, in addition to the temporally correlated noise. Such noise is also called “Common Mode Error” (CME). Possible causes of CME might be errors of satellite orbits and reference frame. (Wdowinski et al., 1997; Dong et al., 2006). CME can be reduced by spatial filtering approach

(Wdowinski et al., 1997) in which epochwise mean values of the stacked residuals are removed from the individual positions. This approach works well when the assumption of spatial uniformity of CME holds. Spatial filtering was improved more in later studies by taking into account the correlations and distances between neighboring sites (e.g., Nikolaidis, 2002; Tian and Shen, 2016). However, spatial scale of CME could not be described well.

Table 2.2. Best noise model for Southern California Integrated GPS Network (SGIN) and Southern part of the Basin and Range Geodetic Network (SBAR). (Table from Langbein (2008)).

Noise Model	Percentage of All Sites		
	North	East	Vertical
FL	32	27	41
RW	21	35	18
PL	11	11	6
FLRW	20	16	21
FOGMRW	8	3	9
BPPL	8	9	5

FL: flicker; RW: random-walk; PL: power law; FLRW: flicker + random-walk; FOGMRW: first-order Gauss-Markov + random-walk; BPPL: band-pass + power law

Spatiotemporal filtering of Dong et al. (2006) utilizes PCA and Karhunen-Loeve expansion and allows non-uniformity in the estimation of CME. PCA and its modified versions later were used widely in spatiotemporal filtering (e.g., Shen et al., 2014; He et al., 2015; Li et al., 2015). However, PCA results need to be studied visually further, and contamination might exist between Principal Components (PCs) which might cause preventing the detection of the subtle geophysical transients in the initial PCs. Lately, Liu et al. (2018) filtered GPS vertical time series in Antarctica more by using Independent Component Analysis (ICA) in addition to PCA.

Another approach to minimize CME is to transform the reference frame by a Helmert transformation into a regional reference frame using fiducial local sites (Szeliga et al., 2004; Melbourne et al., 2005; Ji and Herring, 2011). These methods, by mitigating CME, facilitate the detection of the transient signals and are extensively employed in the geodetic studies (e.g., Lin et al., 2010; Ji and Herring, 2012; Jiang et al., 2012; Blewitt et al., 2013).



## CHAPTER 3

### EMPIRICAL MODE DECOMPOSITION

Fundamentals of the original Empirical Mode Decomposition (EMD) method are first introduced in this chapter. Since it is an experimental approach as its name implies, and hence lacks exact mathematical description, it depends on pre-determined parameters. This may result in obtaining unstable results. These problematic areas are presented in the next subsections. Some improved versions of EMD, such as Ensemble EMD (EEMD), Complementary Ensemble EMD (CEEMD), Complete Ensemble EMD with Adaptive Noise (CEEMDAN) are mentioned afterward. Finally, the approach of denoising/detrending signals using EMD is explained.

#### 3.1 Motivation

Empirical Mode Decomposition (EMD) emerged in Huang et al. (1998), as a preprocessing phase of the nonstationary and nonlinear data which results in Intrinsic Mode Functions (IMFs). Hilbert Spectral Analysis (HSA) is applied to the IMFs afterwards to obtain the instantaneous frequencies as functions of time, and to construct the amplitude-frequency-time distribution (Hilbert Spectrum) of the data. EMD and HSA together are called Hilbert-Huang Transform (HHT).

Conventional data analysis methods, such as spectral analysis (e.g., Priestly, 1981), mostly assume that the underlying process is linear and stationary. A linear function  $f(x)$  satisfies additivity and homogeneity properties, respectively:

$$f(x_1 + x_2) = f(x_1) + f(x_2), \quad (3.1)$$

$$f(\alpha x) = \alpha f(x), \quad (3.2)$$

for all scalar  $\alpha$ , where  $x$  is the independent variable. Such a function can be portrayed as a straight line, graphically. Stationary processes exhibit constant statistical properties (e.g., mean and variance) over selected time intervals. Such processes can be analyzed successfully based on a well-established mathematical theory. Thus, spectral analysis mainly assumes and deals with the stationary processes. However, real-world phenomena, which are generally output of unstable systems, obey this strong assumption very rarely. To cope up with the non-stationarity, data are tried to be transformed into some stationary form, traditionally. For example, data might be detrended by using, e.g., a polynomial fit. Yet, the nature of the non-stationarity is generally much more complex which cannot be explained by a simple trend.

Fourier spectral analysis, which is a dominant method in data analysis, requires linearity and stationarity, and uses pre-determined sines and cosines as basis functions. Each non-zero Fourier coefficient of the Fourier Transform (FT) displays a global uniform harmonic component. Local characteristics, due to the non-stationarity of the signal, cause spurious harmonics and hence energy spreading in the spectrum. Being mathematically sensible does not always bring the physical sense.

Several time-frequency analysis methods have been proposed to overcome the weakness of Fourier analysis on non-stationary data such as, the spectrogram (short-

time Fourier Transform) method (Oppenheim et al., 1999), the wavelet analysis (Daubechies, 1992; Mallat, 2009), the Wigner-Ville distribution (Cohen, 1995; Boashash, 2003), evolutionary spectrum (Priestly, 1981) and the empirical orthogonal function expansion (EOF) (Vautard and Ghil, 1989). A comparison between Fourier, wavelet (the two widely used data analysis methods) and HHT analyses is given in Table 3.1. Other miscellaneous methods can be found in, e.g., Brockwell and Davis (1991). Among these methods, only the EOF provides expansion basis *a posteriori*, that is, derived from the data. However, the linearity and stationarity of the EOF components are not guaranteed. For a discussion about the limitations of these methods see, e.g., Huang et al. (1998), Hou and Shi (2011, 2013a, 2013b). The breakthrough in adaptive non-stationary data analysis was the introduction of the Hilbert spectral representation through EMD (Huang et al., 1998) first, and later through wavelet projection which is suitable for nonstationary but linear time series (Olhede and Walden, 2004).

Table 3.1. Comparison of HHT with Fourier and Wavelet Analyses (Table from Huang and Wu, 2008).

	<i>Fourier</i>	<i>Wavelet</i>	<i>HHT</i>
<i>Basis</i>	a priori	a priori	a posteriori adaptive
<i>Frequency</i>	convolution over global domain, uncertainty	convolution over global domain, uncertainty	differentiation over local domain, certainty
<i>Presentation</i>	energy in frequency space	energy in time-frequency space	energy in time-frequency space
<i>Nonlinearity</i>	no	no	yes
<i>Nonstationarity</i>	no	yes	yes
<i>Feature extraction</i>	no	discrete, no; continuous, yes	yes
<i>Theoretical base</i>	complete mathematical theory	complete mathematical theory	empirical

EMD provides a complete, local and adaptive basis for the expansion of the non-linear/non-stationary data. Orthogonality is not a necessary condition of the EMD, for it is considered in linear systems. Since the local behavior of the non-stationary data evolves over the time (the “non-stationary” is called sometimes also “evolutionary”), studying the “instantaneous frequency” of the signal is important. Instantaneous frequency ( $w$ ) can be described as the derivative of the phase ( $\theta$ ) of the analytical signal (which is a complex-valued function with no negative frequency components):

$$w = \frac{d\theta(t)}{dt}. \quad (3.3)$$

Therefore, the data must be made analytical first. This can be accomplished through the Hilbert Transform. For the sake of integrity, it is now demonstrated how to generate an analytic signal (AS). Hilbert Transform  $y(t)$  of a function  $x(t)$  for all  $t$  is:

$$y(t) = \frac{1}{\pi} P \int_{-\infty}^{+\infty} \frac{x(\tau)}{t-\tau} d\tau, \quad (3.4)$$

where the Cauchy principal value  $P$  expands the class of functions for which the integral exists when  $\tau = t$ . Hilbert Transform in the time domain is the convolution of  $x(t)$  with the operator  $1/\pi t$ , that is, it filters  $x(t)$  by a filter  $1/\pi t$ . Since the convolution in the time domain is equivalent to the multiplication in the frequency domain, the Fourier Transforms of  $x(t)$  and  $1/\pi t$  are multiplied. By applying Inverse Fourier Transform to the product, the Hilbert Transform  $y(t)$  can be obtained.  $x(t)$  and  $y(t)$  form the complex conjugate pair, so the analytic signal  $z(t)$  is:

$$z(t) = x(t) + iy(t) = a(t)e^{i\theta(t)}, \quad (3.5)$$

where  $i = \sqrt{-1}$ . The instantaneous amplitude  $a(t)$  and the instantaneous phase  $\theta(t)$  can be computed as:

$$a(t) = \sqrt{x^2(t) + y^2(t)}, \quad (3.6)$$

$$\theta(t) = \tan^{-1} \frac{y(t)}{x(t)}. \quad (3.7)$$

Both amplitude and frequency are expressed as functions of time, as can be seen explicitly above. This satisfies the locality requirement of the decomposition of the non-linear and non-stationary data.

The real part of the Fourier Transform of the data must not have negative frequency. Otherwise, the instantaneous frequency is meaningless (Gabor, 1946; Bedrosian, 1963; Boashash 1992). Huang et al. (1998) illustrated the justification of this restriction by examining the phase and instantaneous frequency of a simple  $x(t) = \alpha + \sin t$  function for the different values of  $\alpha$  (see Figure 3.1).

When  $\alpha = 0$ , the phase function is a straight line, and the instantaneous frequency is constant. If  $0 < \alpha < 1$ , the centre of the circle of unit radius (the phase plot) is still inside the circle, though the phase function and the instantaneous frequency are different from that of  $\alpha = 0$  condition. If  $\alpha > 1$ , the centre is no longer inside the circle, and thus negative (meaningless) phase and instantaneous frequency values are displayed. This evaluation provided the motivation leading to the Empirical Mode Decomposition, that is, expressing the data as a sum of a small number of *a posteriori* Intrinsic Mode Functions which are restricted to be symmetric with respect to the zero mean level, and hence have physically meaningful instantaneous frequencies obtained through Hilbert Transform.

### 3.2 Empirical Mode Decomposition

An Intrinsic Mode Function satisfies two requirements according to the original definition:

- The number of extrema and the number of zero crossings are equal or differ by one.
- The mean value of the upper and the lower envelopes defined by the local maxima and minima, respectively, is zero at any point.

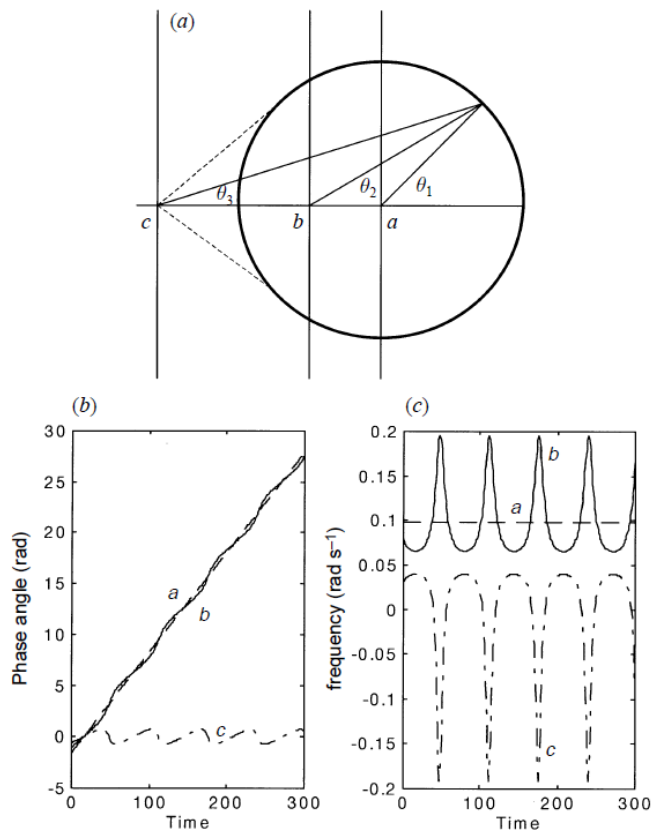


Figure 3.1. For  $\alpha = 0$ ,  $0 < \alpha < 1$ , and  $\alpha > 1$  (corresponding to  $a$ ,  $b$ , and  $c$ , respectively) in  $x(t) = \alpha + \sin t$ ; (a) the phase planes, (b) the unwrapped phase functions, (c) the instantaneous frequencies (Figure from Huang et al., 1998).

The procedure to reduce data into the IMFs is called Empirical Mode Decomposition. The reduction is accomplished through an iterative process known as “sifting”. The EMD algorithm applied to a given signal  $x(t)$  is illustrated in Table 3.2.

Table 3.2. The EMD algorithm

- |  |
|--|
| <ol style="list-style-type: none"> <li>1. Detect all local maxima and minima in <math>x(t)</math>.</li> <li>2. Form the upper (<math>e_{max}(t)</math>) and lower (<math>e_{min}(t)</math>) envelopes by connecting the maxima and minima with a cubic spline, respectively.</li> <li>3. Calculate the mean of the envelopes: <math>m(t) = (e_{min}(t) + e_{max}(t))/2</math>.</li> <li>4. Extract the detail: <math>x(t) = x(t) - m(t)</math>.</li> <li>5. Repeat steps 1-4 (sifting) until the detail <math>x(t)</math> is an IMF (<math>imf_j(t)</math>) according to a stopping criterion.</li> <li>6. Subtract the attained IMF from the data: <math>x(t) = x(t) - (imf_j(t))</math>.</li> <li>7. If <math>x(t)</math> has more than one extremum, return to step 1. Otherwise, the decomposition is finished, and <math>x(t)</math> is the residue <math>r_n(t)</math>.</li> </ol> |
|--|

Finally, the original signal is expressed as follows:

$$x(t) = \sum_{j=1}^n imf_j(t) + r_n(t). \quad (3.8)$$

The sifting process is illustrated in Figure 3.2a-c graphically, using the weekly east offsets of AFYN station in the CORS-TR network. To enhance the visibility, only the data between 2009 and 2012 are displayed, after detrending through the subtraction of a simple linear trend (see Fig. 3.2a). The upper and the lower envelopes are shown in dashed lines, their mean in red dot-dashed line, and the original data in solid line in Figure 3.2b. The difference between the data and the mean of the envelopes is given in Figure 3.2c. As highlighted by a red circle, there still exists local minimum above

the zero mean line. Thus, sifting process is repeated until the detail signal shown in Figure 3.2c ensures the requirements of an IMF mentioned above.

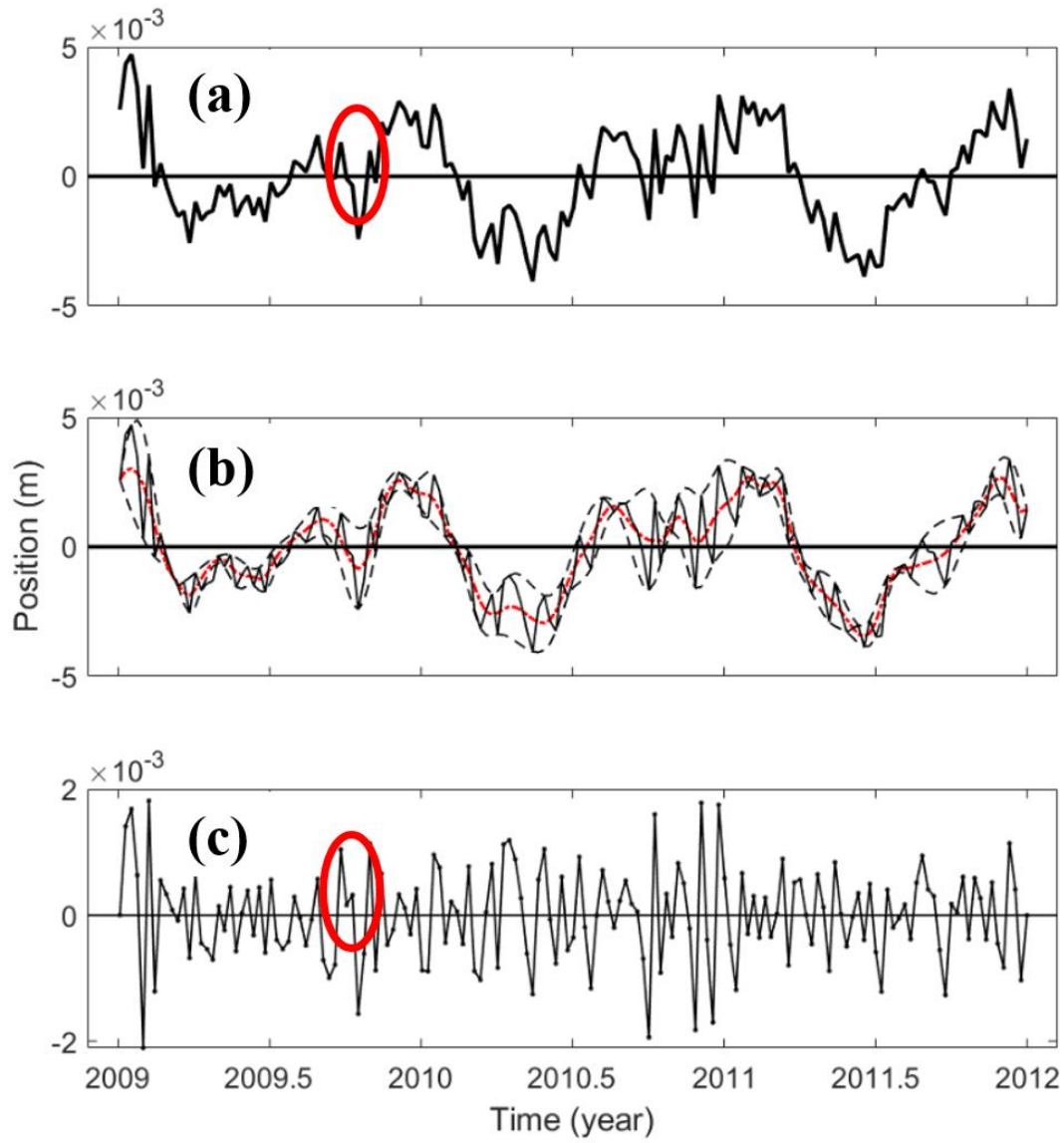


Figure 3.2. The sifting procedure: (a) the east offsets of AFYN station, (b) the upper and lower envelopes in dashed lines, their mean in red dot-dashed line, and the data in solid line, (c) the difference between the data and the mean of the envelopes.



The selected criterion to stop the sifting process for  $j$ th IMF in Huang et al. (1998) depends on the size of the standard deviation ( $SD$ ) calculated from the two consecutive siftings:

$$SD = \sum_{t=0}^T \left[ \frac{|(h_{j(k-1)}(t) - h_{j(k)}(t))|^2}{h_{j(k-1)}^2(t)} \right], \quad (3.9)$$

where  $T$  is the total number of the data points, and  $h$  is the remaining detail of the  $k$ th sifting. The value of  $SD$  is recommended to be between 0.2 and 0.3. The overall EMD process stops when the final residue can no longer produce an IMF, that is, either it is a monotonic function or it possesses only a single extremum. Typically, the total number of IMFs is around  $\log_2 N$  with  $N$  being the total number of the data points (Flandrin et al., 2004; Wu and Huang, 2005), and is also generally linked to the level of the noise (Flandrin et al., 2004). The resulting IMFs, as well as the residual from AFYN data are given in Figure 3.3.

### 3.3 Limitations of the Empirical Mode Decomposition

Since the Empirical Mode Decomposition is deprived of a definite mathematical foundation, its soundness and effectiveness only could have been validated empirically. The uniqueness of the decomposition results is not guaranteed since, e.g., the selected stopping criterion in the sifting process, the interpolation technique used in the formation of the envelopes and the method of handling boundary effects might change the obtained IMFs. These open problems are touched now.

### 3.3.1 Mathematical Foundation

The lack of theoretical foundation of the EMD is the main reason of the other complications mentioned in the following subsections. Principles or laws, and the validity of the results can only be deduced with a mathematical foundation (Huang and Wu, 2008). Until then, user-selected parameters render EMD an optimization issue. Chen et al. (2006) tried to express the EMD analytically by replacing the cubic spline with B-spline. Recently, significant developments have been made in EMD mathematics which can be seen as the most exciting breakthroughs since the introduction of the EMD (Huang and Shen, 2014).

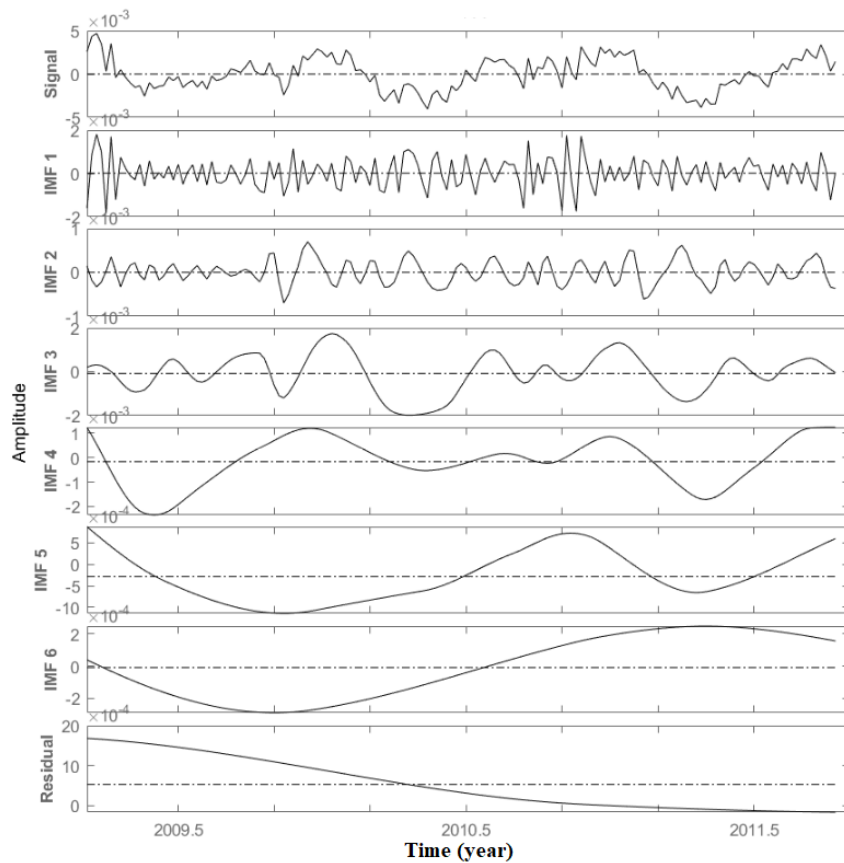


Figure 3.3. AFYN data and its EMD components.

Daubechies et al. (2011) introduced the mathematical framework of an EMD-like method where they used synchrosqueezed wavelet transforms in constructing the components (see also Wu et al., 2011). Hou and Shi (2011, 2013a, 2013b), inspired by EMD and compressed sensing theory (Donoho, 2006), decomposed an arbitrary function into IMFs using a nonlinear optimization process based on sparsity, and justified that EMD is a generalization of the Fourier expansion (Huang and Shen, 2014). Since their method is based on a solid mathematical formulation, pre-defined numerical parameters, such as the number of the siftings are not included in the method and hence do not effect the performance. Moreover, their method is more robust to the noise and end effects.

### **3.3.2 Envelope Interpolation**

Traditionally, natural cubic splines are used in the formation of the envelopes. Overshoots and undershoots of the interpolation which can be seen, e.g., at the beginning of 2009 in Figure 3.2*b*, might cause the generation of new extrema. A gentle hump on a slope which is, e.g., highlighted by a red circle in Figure 3.2*a*, might turn into an extrema after the sifting (see the same time location in Figure 3.2*c*). In addition, the envelopes might intersect the original data. Such problems affect the IMF estimation. To alleviate these problems, Huang et al. (1998) used the taut spline, but the improvement was minor. Rilling et al. (2003) states that the number of the siftings might increase due to the utilization of linear or polynomial interpolation and thus the data might be over-decomposed. Chen et al. (2006) proposed to use B-spline to alleviate the creation of extra extrema by cubic spline. Time-consuming higher-order splines might introduce additional length scales and result in slow or non-convergence (Huang and Wu, 2008). Which spline suits EMD best is still an open question.

### **3.3.3 Boundary Effects**

Since the characteristics of the first and the last data points of the original signal are not known (whether they are extrema or not), and the envelopes are needed to be extended to cover the whole data range, large swing problems of cubic splines might occur at the ends. Gradual influence of the end swings through the sifting process can distort the results. Precious data are lost near the ends if a windowing procedure is applied to deal with the end effects. Instead, Huang et al. (1998) extended the data beyond the real range by adding artificial waves at both ends, defined by the two consecutive extreme values nearest to the boundary. Prediction of the non-linear and non-stationary time series beyond the real span is challenging. Various methods have been proposed to handle the end effects in EMD process such as, data flipping (mirror) (Rilling et al., 2003), support vector regression machine (Cheng et al., 2005), improved slope (Wu and Qu, 2008), artificial neural networks (Xun and Yan, 2008), gray prediction model (He et al., 2012) and wavelet denoising (Yan and Lu, 2014).

### **3.3.4 Stopping Criterion**

The number of siftings in the IMF production is determined by the stopping criterion. Every round of sifting makes the upper and lower envelopes more symmetric which is a desirable condition. However, the exact symmetry can only be reached when the envelopes become constant lines which causes the removal of the meaningful amplitude fluctuations. This yields to pure frequency modulated IMFs only. On the other hand, too few siftings might generate components that do not approximate an IMF sufficiently. Therefore, a wisely limited number of siftings is required. The commonly used stopping criteria might be grouped as follows:

- Cauchy type criterion (Huang et al., 1998) as described in section 3.2, and its variants (Shen et al., 2005; Huang and Wu, 2008).
- $S$ -number criterion (Huang et al., 1999, 2003) where the equality of the numbers of zero-crossings and extrema holds for  $S$  consecutive times. A typical value of  $3 \leq S \leq 5$  has been proved successful in Huang et al. (2003).
- Fixed sifting number criterion (Wu and Huang, 2004, 2005, 2009). Wu and Huang (2010) states that fixing the sifting number to 10 makes EMD similar to an adaptive dyadic filter bank.

Obviously, Cauchy type criteria has nothing to do with the definition of the IMF, and deciding on the value of  $SD$  is subjective. Further, it is not certain whether the IMFs will have same numbers of zero crossings and extrema. To overcome these shortcomings, the  $S$ -number criterion was proposed.

### 3.3.5 Confidence Limit and Statistical Significance

Since the stopping criterion, splines, and boundary conditions all have a changing effect on the decomposition results, it is desirable to have a confidence limit for EMD to assess the sensitivity of the input signal to the sifting process. Huang et al. (2003) examined the coherence of the decompositions by changing the  $S$  number. Hereby, it is possible to study the statistical distribution of the yielding IMF sets and obtain a quantitative confidence limit. However, this is a limited approach, since the effects of the other parameters, such as spline interpolation and boundary conditions, on the uniqueness of the IMFs, remain untreated.

Flandrin et al. (2004, 2005, 2014) and Flandrin and Gonçalves (2004), by studying the Fourier spectra of the IMFs of various fractional Gaussian noise, and Wu and

Huang (2004, 2005), by inspecting the white noise, discovered that EMD behaves as a dyadic filter bank. Flandrin et al. (2005) applied EMD on the extensive Monte Carlo simulations of the fractional Gaussian noise, and determined the theoretical distribution of the energy of the resulting IMFs and their corresponding 95% and 99% confidence limits. From this point of view, any IMF above these limits should contain significant information statistically.

### **3.3.6 Missing Data Points**

Locality is one of the most attractive properties of EMD. When applied to equally spaced and sufficiently long real-world data, EMD can help making physical interpretations through meaningful instantaneous frequencies and their exact time locations. However, true interpretations might be hindered by the existence of the missing data points which is very common in the nonsynthetic signals (e.g., due to the receiver malfunction in the GPS coordinate time series). Since there is no solution for predicting the values originated from a non-linear/non-stationary process, we are imposed on two unsatisfactory approaches: (1) to cut and paste all the data points next to each other as if there is no gap, and (2) to interpolate the missing values as properly as possible.

The inappropriateness of the first approach is apparent, since the time information of the local behaviors is lost, which is against the philosophy of the EMD method. As for the second approach, the interpolation technique used is important. A linear interpolation, for example, causes constant frequency during the corresponding period. A polynomial or a spline interpolation neither creates nor removes any scales (if the undershoots and overshoots are not counted), however, they might lead to large swings as the data gap becomes larger. When the missing values occur especially in the local extrema, envelopes cannot be formed properly, and thus EMD results are

distorted. Barnhart et al. (2011, 2012) applied EMD to complete data segments only, and adapted a mirroring approach for the data gaps. Kim and Oh (2016) proposed self-consistency (Tarpey and Flury, 1996) as an imputation method of the missing values before decomposing the signal with the EMD.

### **3.3.7 Mode Mixing**

Mode mixing is a severe limitation of the EMD and might occur if:

- very disparate oscillations are present in a single IMF or,
- very similar oscillations are present in different IMFs.

It is a consequence of signal intermittency (Huang et al., 1998), and signals having frequencies too close, cannot be separated. Thus, IMFs might lose their physical meaning. An example of mode mixing is illustrated in Figure 3.4, by giving the comparison of the decomposition results of Remote Sensing Systems (RSS) T2, the channel 2 tropospheric temperature of the microwave sounding unit (Mears et al., 2003), and of the University of Alabama at Huntsville (UAH) T2, an alternative analysis of the same channel 2 tropospheric temperature of the microwave sounding unit (Christy et al., 2000). Since there is only a minor difference between these two input signals, they can be seen as their perturbed versions with a low level of random noise. Decompositions are significantly different due to the mode mixing (Huang and Wu, 2008). Which decomposition to opt for is an immediate question, and the answer is ambiguous.

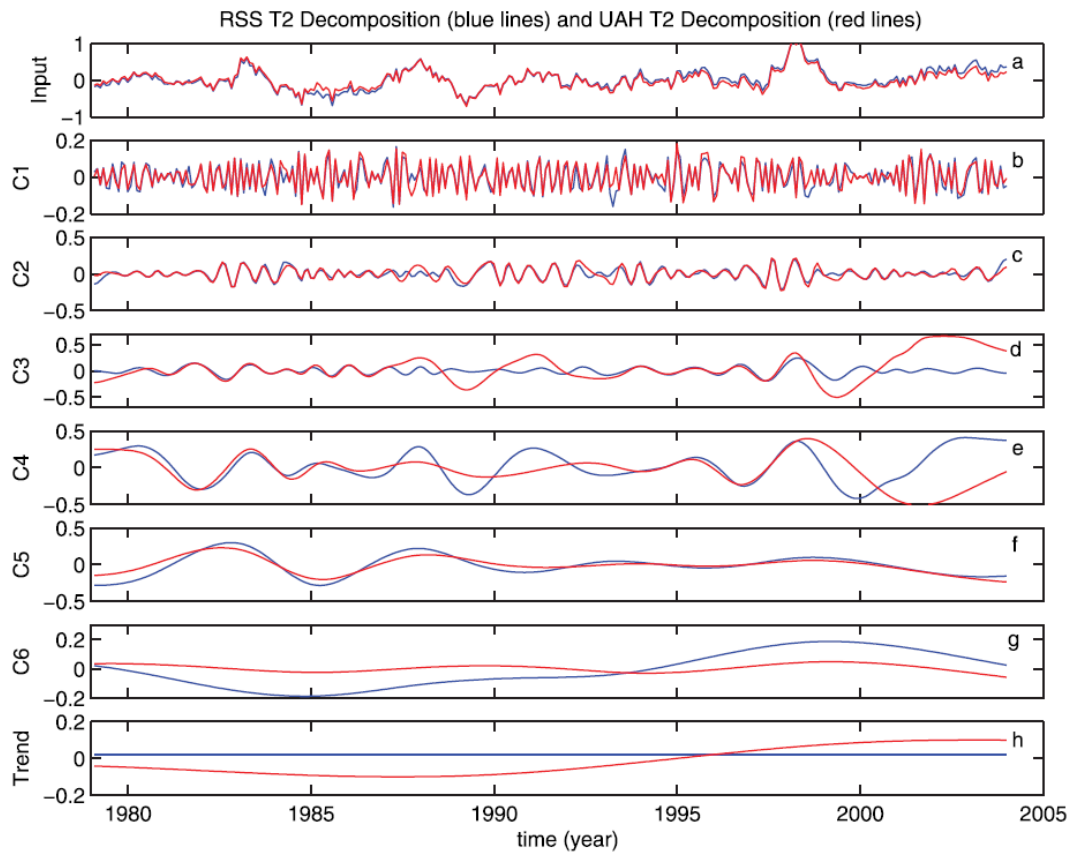


Figure 3.4. Significantly different decomposition results of very similar input signals due to mode mixing (Blue lines correspond to RSS T2, red lines correspond to UAH T2, see the explanation in the text). (Figure from Huang and Wu, 2008).

### 3.4 Methodological Improvements

Other than the advances in EMD mathematics, some methodological developments have also been made by devising the noise-assisted versions of EMD. These variants of EMD are presented in the following subsections.



### 3.4.1 Ensemble Empirical Mode Decomposition

Since mode (scale) mixing can be counted as the most critical problem of EMD, Ensemble Empirical Mode Decomposition (EEMD) approach (Wu and Huang 2005, 2009), which alleviates this problem, might be acknowledged as the most significant methodological improvement to EMD. EEMD was inspired by the noise added analyses such as those in Flandrin et al. (2005). The basic idea depends on applying EMD to the white noise added versions of the original signal. The ensemble means of the resulting IMFs are accepted as the true IMF components. The EEMD algorithm is given in Table 3.3.

Table 3.3. The EEMD algorithm

<ol style="list-style-type: none"><li>1. Add white noise of finite amplitude to the input signal.</li><li>2. Apply traditional EMD to the signal obtained in step 1.</li><li>3. Repeat step 1-2 for a large number of times, by adding different sets of white noise.</li><li>4. Calculate the ensemble means of the corresponding IMFs.</li></ol>
--

EEMD intuition is straightforward, that is, white noise sets cancel each other out, and only the true components persist in the ensemble mean. A dyadic filter bank consists of a number of band-pass filters having a constant shape like, e.g., a Gaussian distribution. Neighbouring filters, for example in a decreasing order, cover half of the frequency range of the preceding filter. There might be overlapped frequency ranges of the filters. Finite magnitude noise makes EMD behave as a truly dyadic filter bank (Wu and Huang, 2009), and provides the uniqueness of the decomposition. IMFs

generated from the same data, presented previously in Figure 3.4, by using the EEMD are displayed in Figure 3.5. It is seen that EEMD diminished the mode mixing largely.

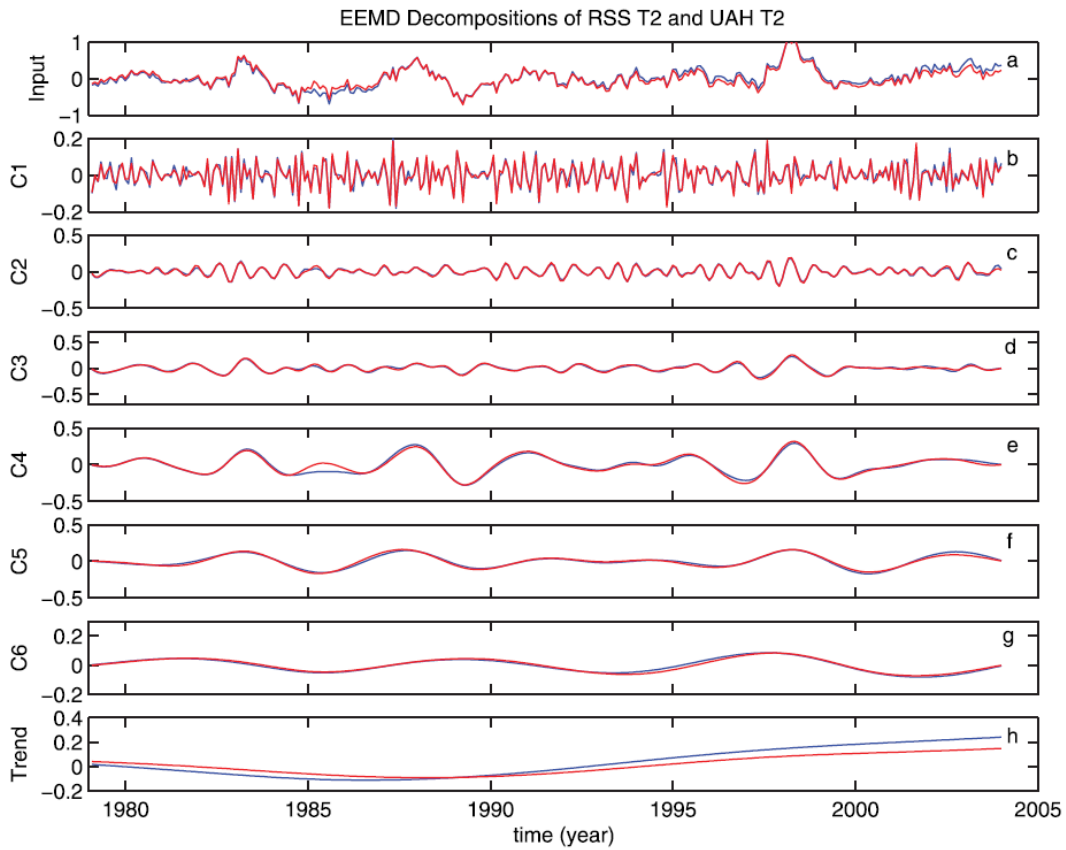


Figure 3.5. EEMD results of the data presented in Figure 3.4 (Blue lines correspond to RSS T2, red lines correspond to UAH T2, see the explanation in the text). For both decompositions, the ensemble number is 100, and the added noise has an amplitude of 0.2 of that of the standard deviation of the corresponding data (Figure from Huang and Wu, 2008).

### **3.4.2 Complementary Ensemble Empirical Mode Decomposition (CEEMD) and Complete Ensemble Empirical Mode Decomposition with Adaptive Noise (CEEMDAN)**

Ensemble Empirical Mode Decomposition, while resolving the mode mixing problem, causes the decomposition to be incomplete, that is, the input signal cannot be reconstructed by summing up the resulting IMFs and the residue perfectly, due to the residual noise introduced, especially when the number of ensemble is not sufficiently large. In addition, different number of IMFs might be generated from the different realizations of signal plus noise, and thus averaging might be flawed.

The Complementary Ensemble Empirical Mode Decomposition (CEEMD) method proposed by Yeh et al. (2010), deals with the reconstruction problem well. In this method, noise is added to the input signal in pairs (positive and negative), i.e., there are two sets of mixtures: one with positive noise, one with negative noise. The final IMFs are the ensembles of the IMFs with these noises. Although CEEMD removes the residue of the added white noises, and hence makes the decomposition complete, problem of generating different number of IMFs from different realizations continues.

Another variant of EEMD is the Complete Ensemble Empirical Mode Decomposition with Adaptive Noise (CEEMDAN), proposed by Torres et al. (2011) and Colominas et al. (2012). In traditional EEMD, every realization of the signal plus white noise is decomposed independently from the other realizations. CEEMD makes a connection between these realizations and the original data. Initially, the first IMF is computed as it is done in the traditional EEMD. This IMF is subtracted from the original data, and a residue is obtained. After that, residue plus noise realizations are made, and EEMD is applied to these realizations. Second IMF is the average of the first modes

of these decompositions. A new residue is attained by subtracting the second IMF from the former residue, this time. These steps are iterated until the residue cannot be decomposed further. CEEMDAN achieves a negligible reconstruction error and solves the problem of the generation of the different number of IMFs due to the different noise realizations (Colominas et al., 2014).

### 3.5 Signal Denoising with EMD

Denoising with EMD mainly depends on the filtering properties of the method, reported in, e.g., Rilling et al. (2003), Wu and Huang (2004), Flandrin and Gonçalves (2004), Flandrin et al. (2004, 2005, 2014), who examined the Fourier spectra of IMFs of fractional Gaussian noise and came to the conclusion that EMD behaves as a dyadic filter bank. Wu and Huang (2010) and Wang et al. (2010) state that this behavior is valid only when the number of siftings is fixed to 10, and the increasing number of siftings causes the ratio of mean frequency between the neighboring IMFs to decrease below 2. In this section, we focus on the denoising procedure described in Flandrin et al. (2004, 2005, 2014).

The movements originating from the Brownian motion are random. However, the Fractional Brownian motion (fBm) has long-range, temporal and spatial correlation unlike the classical Brownian motion with independent increments. This makes fBm a convenient model for complex natural processes. The Fractional Gaussian noise, fGn, (Mandelbrot and Van Ness, 1968) is the increment process of fBm and a widely used model for broadband noise with no dominant frequency band. The self-similarity parameter Hurst ( $H$ ) index ( $0 < H < 1$ ), determines the statistical properties of fGn, whose autocorrelation sequence is:

$$r_H[k] = \frac{\sigma^2}{2} (|k-1|^{2H} - 2|k|^{2H} + |k+1|^{2H}). \quad (3.10)$$

When  $H = 0.5$ , the process is uncorrelated. If  $H < 0.5$ , the process shows short-range dependence, while it exhibits long-range dependence if  $H > 0.5$ . The relationship between  $H$  and  $\alpha$  (spectral index of power-law model) is as follows (Schroeder, 1992):

$$\alpha = 2H - 1, \quad (3.11)$$

where  $\alpha \leq 2$ . Flandrin et al. (2004, 2005) and Flandrin and Gonçalves (2004) carried out extensive simulations and examined the Fourier spectra of IMFs in noise-only situations (where  $0.1 \leq H \leq 0.9$ ). They found that, excluding the spectra of the first IMFs (modes), the spectra of all modes of any fGn appear to be the same, when they are scaled appropriately (see Figure 3.6). Moreover, decrease in the number of zero-crossings (which can be used to express the mean frequency), as the order of the modes increases is around 2, and can be approximated as:

$$\rho_H \approx 2.01 + 0.2(H - 0.5) + 0.12(H - 0.5)^2. \quad (3.12)$$

Furthermore, it has been demonstrated that the IMFs log-variance is a function of the IMF index, controlled by the Hurst index (see Figure 3.7):

$$\log_2 V_H[k] = \log_2 V_H[2] + 2(H - 1)(k - 2) \log_2 \rho_H, \quad (3.13)$$

for  $k \geq 2$ .

Hereby, the Hurst index for a fGn process can be estimated as:

$$\hat{H} = 1 + \frac{k_H}{2}, \tag{3.14}$$

where  $k_H$  is the slope of the corresponding straight line in Figure 3.7. For a comparison of Hurst estimators see, e.g., Rea et al. (2009).

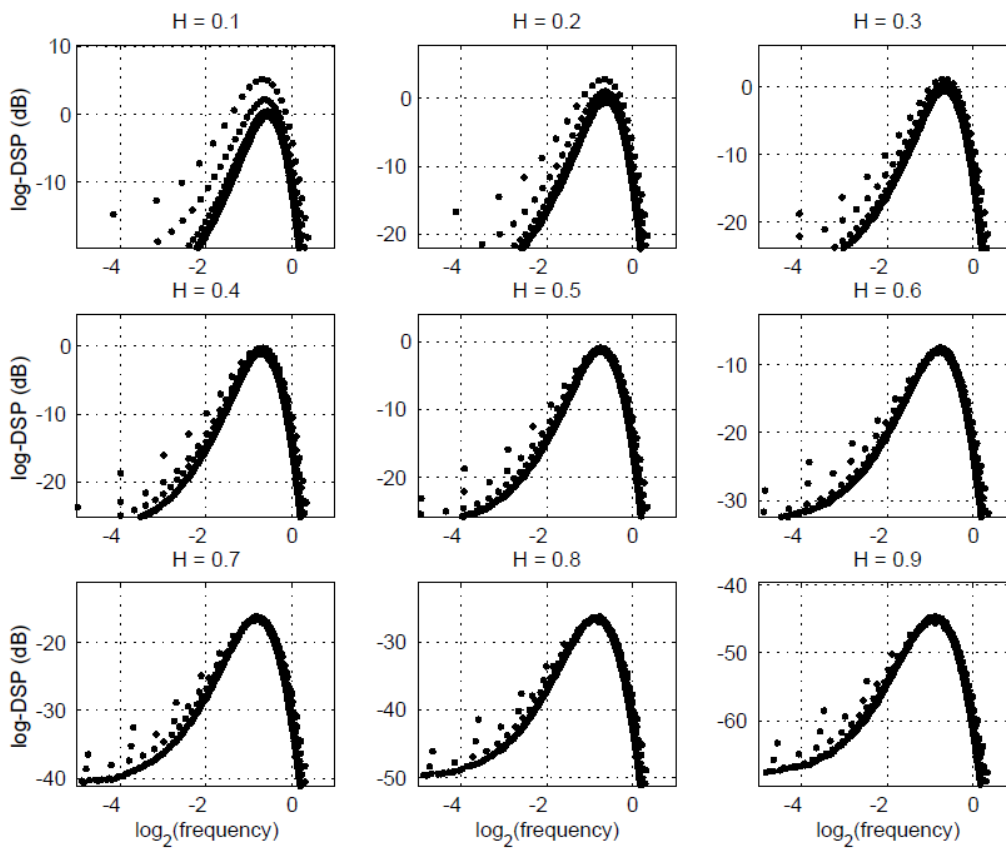


Figure 3.6. Rescaled spectra of IMF components between 2 and 6 (Figure from Flandrin, 2005).

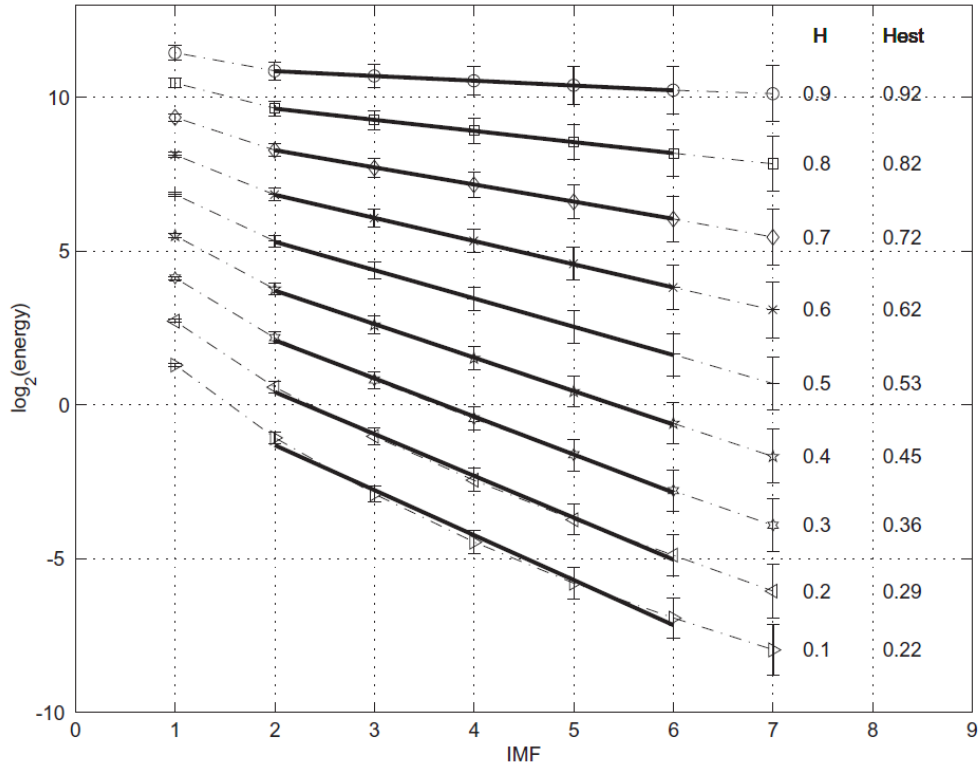


Figure 3.7. Estimated IMF log-variance controlled by the Hurst index, and fitted straight lines. The error bars correspond to the standard deviations associated with the realizations (Figure from Flandrin, 2005).

The variability of the variance estimate is indicated with the observed standard deviation (vertical bars) in Figure 3.7, which is a rough approach. For a greater appreciation, the experimental mean, median and various confidence intervals for  $H = 0.2, 0.5$  and  $0.8$  are displayed in Figure 3.8.

By examining the logarithm of the relative confidence intervals, the following formula has been suggested:

$$\log_2 \left( \log_2 \left( \frac{T_H[k]}{W_H[k]} \right) \right) = a_H k + b_H, \quad (3.15)$$

where  $W_H[k]$  and  $T_H[k]$  are the  $H$ -dependent variations of the IMF energy and mean period, respectively.  $T_H[k]$  can be estimated as follows (Rilling et al., 2005):

$$\hat{T}_H[k] = \frac{\text{distance between the first and the last zerocrossing}}{\text{number of zerocrossings}-1}. \quad (3.16)$$

The relation between  $V_H[k]$  and  $\hat{T}_H[k]$  is illustrated in Figure 3.9.

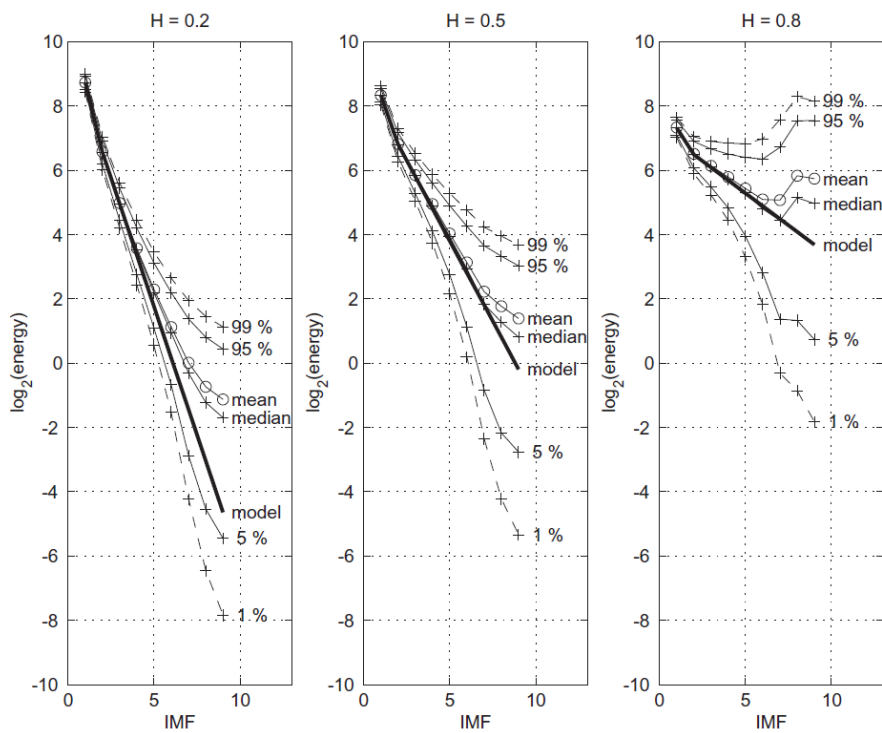


Figure 3.8. For  $H = 0.2, 0.5$  and  $0.8$ , the statistical characteristics (mean, median, confidence intervals) of the estimated IMF variances, together with the linear models presented previously in Figure 3.6 (Figure from Flandrin, 2005).

The confidence interval parameters,  $a_H$  and  $b_H$ , which were deduced from the simulations, are given in Table 3.4.



Table 3.4. Confidence interval parameters (Table from Flandrin, 2005)

$H$	$\beta_H$	$a_H(95\%)$	$b_H(95\%)$	$a_H(99\%)$	$b_H(99\%)$
0.2	0.487	0.458	-2.435	0.452	-1.951
0.5	0.719	0.474	-2.449	0.460	-1.919
0.8	1.025	0.497	-2.331	0.495	-1.833

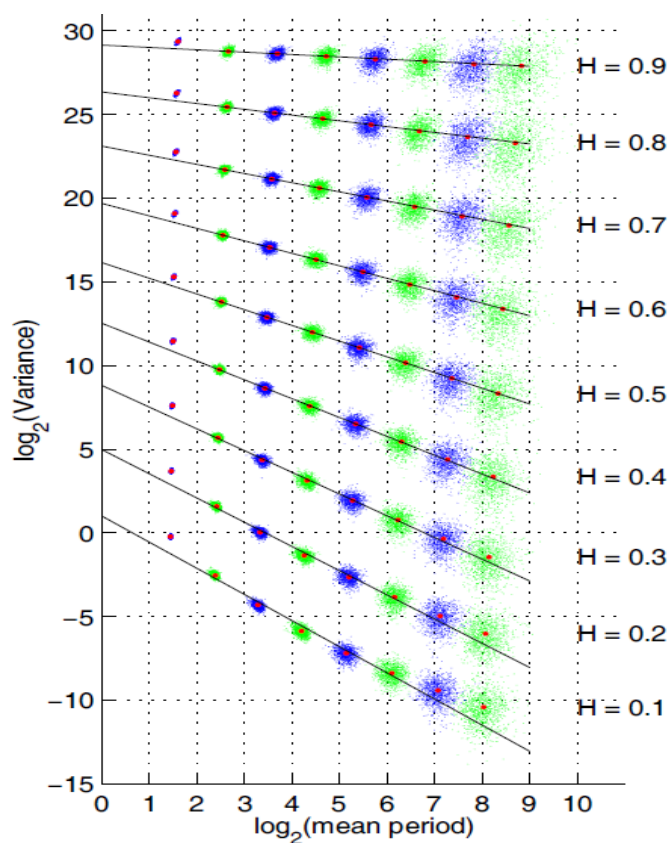


Figure 3.9. The relation between  $V_H[k]$  (IMF variance) and  $\hat{T}_H[k]$  (mean period) (Figure from Rilling et al., 2005).

Finally, taking into account these considerations, the denoising procedure can be summarized as follows:

1. Estimate the noise level first, assuming it is mostly in the first IMF, by computing:

$$\widehat{W}_H[1] = \sum_{n=1}^N imf_1^2[n], \quad (3.17)$$

where  $N$  is the data length.

2. Estimate the noise only model by computing the subsequent values of  $W_H[k]$  :

$$\widehat{W}_H[k] = C_H \rho_H^{-2(1-H)k}, \quad (3.18)$$

where  $k \geq 2$  and  $C_H = \widehat{W}_H[1]/\beta_H$  by using  $\beta_H$  values from Table 3.4.

3. Estimate the corresponding model for the chosen confidence interval by using (3.15) and Table 3.4.
4. Compare the IMF energies by using the confidence interval as a threshold.
5. Compute a partial reconstruction by summing up only the residual and those IMFs whose energy exceeds the threshold.

The above explained procedure is used in this study to improve the SNR of the GPS coordinate time series by suppressing the white noise. This is accomplished by removing the IMFs whose energies are inside the 95% confidence interval of  $H = 0.5$ .

## CHAPTER 4

### PRINCIPAL COMPONENT ANALYSIS

Principal Component Analysis (PCA) is one of the oldest and widely used statistical technique in the analysis of multivariate data sets. In this chapter, we present the formulations of PCA briefly, together with a general framework of its application.

#### 4.1 Introduction

PCA was introduced by Pearson (1901) first, and later developed by Hotelling (1933). It has several other names (although there might be minor differences between them), including Karhunen-Loeve Transform, Hotelling Transform, Factor Analysis, Empirical Orthogonal Functions.

There are two main purposes of PCA: (1) identifying the patterns, which are normally not easily discernible in the original data, and (2) reducing the dimensionality, like e.g., compressing a hyperspectral image, by sacrificing only little and insignificant information. To accomplish these, PCA uses a orthogonal transformation, which transforms the possibly correlated variables to linearly uncorrelated variables (principal components). These principal components are in an order with respect to the variations (information) they convey of the original variables. The PCA of a  $n$  (observations) by  $p$  (variables) data matrix  $\mathbf{X}$  results in  $\min(n - 1, p)$  number of distinct principal components (PCs). Each PC is a linear combination of the original

variables with same length, and orthogonal to (and thus uncorrelated with) the preceding PCs.

Though the application spectrum of PCA is very wide, the method is not devoid of limitations, which are mostly due to (1) the large amount of missing data and outliers, and (2) the mixed nature of the data. Although there are studies to generalize PCA method to cope up with these difficulties (see e.g., Vidal, 2016), it is focused here on the classical PCA method, whose details can be found in general textbooks (e.g., Jackson, 1991; Jolliffe, 2002) and tutorials (e.g., Smith, 2002; Shlens, 2005). These references also provide necessary algebraic proofs which are not included here, such as the equality of the inverse of an orthogonal matrix and its transpose, and diagonalization of a symmetric matrix by a matrix of its orthonormal eigenvectors, for a complete understanding of the underlying math.

## 4.2 Principal Components Transformation

The eigenvalue decomposition of the data covariance matrix (1), or the singular value decomposition (SVD) of the data matrix (2) can be used in the implementation of PCA. Usually, the data matrix is normalized in an initial step, i.e., it is centered, and sometimes also divided by the standard deviations of the variables, to prevent biased results, due to the large differences between the ranges of the individual variables. Assume that  $\mathbf{X}$  is a  $n$  (observations) by  $p$  (variables), centered data matrix. The  $p$  by  $p$  covariance matrix  $\mathbf{C}$  of the data matrix is:

$$\mathbf{C} = \mathbf{X}^T \mathbf{X} / (n - 1) \quad (4.1)$$

The covariance matrix describes the scatter of the data about the mean and the correlations between the variables. It is a symmetric matrix, and can be diagonalized as:

$$\mathbf{C} = \mathbf{V}\mathbf{L}\mathbf{V}^T, \quad (4.2)$$

where  $\mathbf{V}$  is a matrix consists of eigenvectors in its columns, and  $\mathbf{L}$  is a matrix having eigenvalues  $\lambda_i$  on the diagonal, in decreasing order. To be complete, the eigenvector  $\mathbf{v}$  of a square matrix  $\mathbf{A}$  is a non-zero vector that, when it is multiplied by  $\mathbf{A}$ , it is only scaled by a scalar value  $\lambda$ , and does not change direction:

$$\mathbf{A}\mathbf{v} = \lambda\mathbf{v}, \quad (4.3)$$

where the scalar  $\lambda$  is the eigenvalue associated with the eigenvector  $\mathbf{v}$ .

The eigenvectors of the covariance matrix of the data are the *principal directions* of the data, and the projections of the data on these directions,  $\mathbf{XV}$ , are called *principal components* or *scores*. Principal components are linear combinations of the original variables, and they are uncorrelated. Since principal directions are just a rotation of the original directions, the principal components transform is classified as a rotational transform. The most variance (information) of the data is in the first principal direction, and the least variance is in the last principal direction. Eigenvalues display the variances in the direction of the respective PCs. When we rank the eigenvectors with respect to their associated eigenvalues from highest to lowest, the principal components are in the order of significance.

Similarly, the singular value decomposition of  $\mathbf{X}$  is:

$$\mathbf{X} = \mathbf{USV}^T, \quad (4.4)$$

where  $\mathbf{U}$  is a unitary matrix, and  $\mathbf{S}$  is a matrix having singular values  $s_i$  on the diagonal. So:

$$\mathbf{C} = \frac{\mathbf{VSU}^T\mathbf{USV}^T}{n-1} = \mathbf{V} \frac{\mathbf{S}^2}{n-1} \mathbf{V}^T, \quad (4.5)$$

which means that right singular vectors  $\mathbf{V}$  are principal directions, and the relation between the singular values and the eigenvalues of the covariance matrix is:

$$\lambda_i = \frac{s_i^2}{n-1}. \quad (4.6)$$

The principal components are:

$$\mathbf{XV} = \mathbf{USV}^T\mathbf{V} = \mathbf{US} . \quad (4.7)$$

The original data can be reconstructed by:

$$\mathbf{X} = \mathbf{XV}\mathbf{V}^T = \mathbf{USV}^T . \quad (4.8)$$

Having the principal components and associated eigenvalues in hand, the percentage of the total variance explained by each PC can be computed via dividing the eigenvalue of each component by the sum of the eigenvalues. These explanation percentages of the PCs can be viewed, e.g., on a scree plot, and which PCs to retain is decided. The higher the percentage, the more significant is the corresponding PC. The

matrix of the eigenvectors of the selected PCs is named *feature vector*. Finally, the new data set can be derived as:

$$\mathbf{FinalData} = \mathbf{FeatureVector}^T \mathbf{X}^T, \quad (4.9)$$

or similarly, by selecting  $m$  first columns of  $\mathbf{U}$ , and  $m$  by  $m$  upper-left part of  $\mathbf{S}$ :

$$\mathbf{FinalData} = \mathbf{U}_{n \times m} \mathbf{S}_{m \times m}. \quad (4.10)$$

The flowchart of the whole PCA procedure, using the eigenvalue decomposition of the covariance matrix of the data, is summarized in Table 4.1.

Table 4.1. Flowchart of the PCA, using eigenvalue decomposition of the data covariance matrix.

<b>Step 1</b>	Organize the data.
<b>Step 2</b>	Subtract the mean.
<b>Step 3</b>	Calculate the covariance matrix.
<b>Step 4</b>	Calculate the eigenvectors and eigenvalues of the covariance matrix.
<b>Step 5</b>	Choose the components to be retained and form the feature vector.
<b>Step 6</b>	Derive the new data set.

PCA is used in this study to detect the tectonically driven transient signals in GPS time series. These transients are common to many but not all time series.





## CHAPTER 5

### GPS ANALYSES AND TRANSIENT SIGNAL DETECTION

The theory and the background information underlying the transient signal detection through the high-precision analysis of GPS data, Empirical Mode Decomposition, and Principal Component Analysis, are provided in the previous chapters. The daily GPS data from Turkish National Permanent GNSS Network-Active (CORS-TR), which has critical importance in Turkey due to the lack of any other countrywide permanent GNSS network, specifically designed for tectonic studies, are processed in this chapter first. Considering the state-of-the-art approaches, models and products, reliable coordinate time series are generated. Secular velocities, seasonal signals, offsets, known signals, data gaps, noise, outliers etc. are determined, and the precise coordinates and the velocities of the stations are estimated.

Taking into consideration the uncertainties, homogeneity and various performance criteria, a sufficient number of local stations are selected, and the solutions (time series) are expressed in a Turkey-fixed reference frame based on the coordinates of the selected stations. This way, the effect of Common Mode Error, which might hinder the detection of the transient signals, is diminished. Such a procedure has been implemented for the first time in the literature in the analyses of CORS-TR stations. Ensemble Empirical Mode Decomposition (EEMD) is applied to the precise and CME-reduced time series afterward, and the white noise in the time series is suppressed.

Transient signals are searched in the denoised signals by seeking spatial coherence through Principal Component Analysis. The significance of the detected signals is determined by looking for systematic temporal patterns, and by assessing the largeness of the eigenvalues and  $\chi^2$  values of the first PCs. The detection capability of the transient signal detection method is demonstrated on: (1) renowned slow slip events in Cascadia, (2) inflation at Akutan volcano, and (3) post-seismic deformation at CORS-TR sites, after October 23, 2011 Van earthquake.

## **5.1 High-precision GPS Analyses**

### **5.1.1 Introduction**

The Global Positioning System (GPS) is a versatile tool widely utilized in diversified applications, calling for positioning with different levels of accuracies. Today, even a simple hand-held GPS receiver may provide three dimensional coordinates of a point with a couple meters level of precision, which is sufficient for many ordinary everyday needs, such as navigation. However, geodesy, geodynamics, geophysics, i.e., Earth sciences, mostly do need very high level of positioning precision (cm, mm, or even sub-mm level). To reach this goal, receivers with extended capabilities, long-duration GPS observations, sophisticated software, auxiliary products etc. are exploited.

Since the Earth is a kind of living organism covered with moving (which is believed to be due to the convection currents) tectonic plates, a point fixed to a plate cannot be assumed stable. The motion of the point is the consequences of the motion of the plate on which the point is placed, the interactions between the plates, the atmospherical and tidal loadings, noise, and of many other local effects which can be transient or persistent. Often, this is an inverse problem, since the contributions of these effects to the motion of the point cannot be measured directly. Rather, they are deduced and

modeled from the actual motion (velocity) of the point, which is estimated through the repeated GPS observations over time.

Traditionally, the velocity of a geodetic point is estimated by processing the episodic (campaign type) GPS measurements which are carried out with appropriate time intervals. Dense networks consist of campaign points provide velocity fields with high spatial resolution. Geodetic velocity fields (through which, e.g., strain analyses are realized) are commonly used in geophysical studies in Anatolia, such as in determining the plate motions and in monitoring the tectonic deformations (e.g, Kahle et al., 2000; Nyst and Thatcher, 2004; Reilinger et al., 2006; Aktuğ et al., 2009, 2013, 2016; Ozener et al., 2010).

Permanent GPS/GNSS networks which consist of stations at which positioning signals are collected continuously, have been increasingly established, especially after 1990s. Compared to campaign-type, permanent-type positions and velocities are generally more reliable and have lower uncertainties. Despite being one of the most tectonically active area on the Earth, Turkey lacks any national-scale, dense permanent GPS/GNSS network aiming at tectonic monitoring, unfortunately. High costs of long-term operation and maintenance of such a network is probably the primary reason of this lacking. Although there are some micro-geodetic networks, such as Turkish National Permanent GNSS Network (Kılıçoğlu et al., 2003), they concentrate on some designated region with limited number of stations.

On the other hand, a homogeneous national scale Real Time Kinematic (RTK) type permanent network, CORS-TR, (<http://www.tusaga-aktif.gov.tr/Map/SensorMap.aspx>; [http://cors-tr.iku.edu.tr/corstr\\_projeozetigenel.htm](http://cors-tr.iku.edu.tr/corstr_projeozetigenel.htm)) has been established since 2008 in Turkey. The distribution of the CORS-TR sites, together with the general tectonic setting in Anatolia (McClusky et al., 2000; Emre et al., 2013)

is displayed in Figure 5.1. The main purpose of CORS-TR system is to provide RTK corrections to the users on the field, and hereby to ensure cm-level coordinate precision. Since the large-scale map production is officially based on the CORS-TR-derived coordinates in Turkey, it has become extremely popular, especially in the cadastral studies. As of June, 2019, there are ~11.500 users registered on the system. Besides, the system is being augmented by the addition of new reference stations. For example, 12 new reference stations have been installed during 2019. Therefore, to ensure the reliability and the stability of the system, and to make the coordinate time series and velocities employable in the tectonic studies (considering the lacking of any other such network) which necessitates ultra-high precision, processing the CORS-TR GPS data and the time series with high-quality standards is of utmost importance. In addition to the developments in the GPS satellites' and receivers' technology, GPS data processing strategies have also been evolved with the inclusion of the new models, products and approaches. Whenever a severe effect on the results due to a mismodeled or unmodeled phenomenon is discovered, reprocessing of the whole data set might be needed, which can be very time consuming.

Hence, a thorough investigation about the performances of the CORS-TR reference stations has been carried out and a high-precision GPS data analysis strategy has been developed within the scope of a project supported by Scientific and Technological Research Council of Turkey (TUBITAK) under the grant number 113Y511 (Karşlıoğlu et al., 2017).

### **5.1.2 CORS-TR Data**

CORS-TR network stations had been installed between June 28, 2008 and June 30, 2011 in Turkey and in Turkish Republic of Northern Cyprus (TRNC). It consists of 146 homogeneously distributed permanent GNSS stations, originally. But as of June

2019, this number reached 158 with the addition of 12 new stations in 2019 (see Figure 5.1). Inter-station distances decrease down to ~100 km, and increase up to ~40 km in some regions. Yet, the average distance between the stations is ~70 km. 141 stations are installed on top of the buildings, and 17 stations are on the ground (see Figure 5.2)

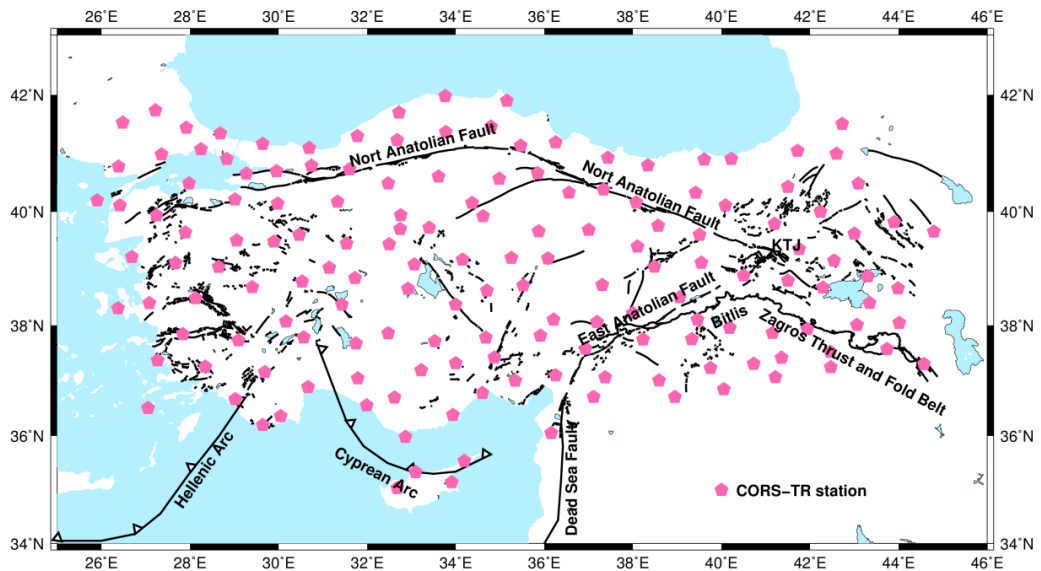


Figure 5.1. 158 CORS-TR stations (as of June, 2019) and general tectonic setting in Anatolia. KTJ, Karliova Triple Junction. Major tectonic structures are adapted from McClusky et al., 2000 and Emre et al., 2013.

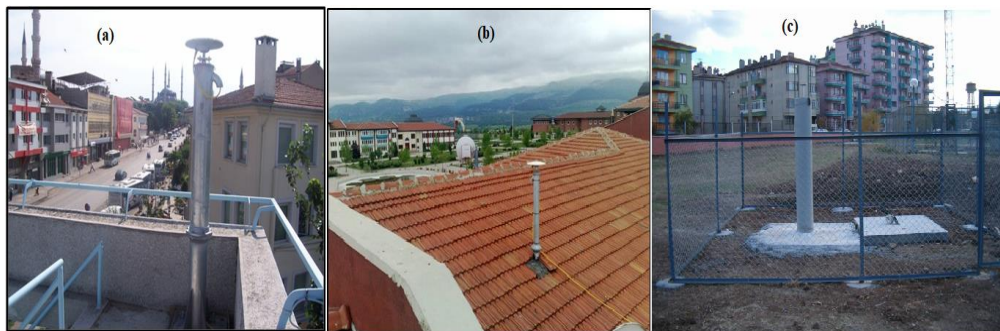


Figure 5.2. CORS-TR monument types: (a) terrace (EDIR), (b) roof (KUTA), (c) ground (AFYN).

CORS-TR data are being processed routinely (see e.g., Ozdemir et al. 2011) in General Directorate of Mapping (GDM), who is the responsible institution of calculating the precise coordinates and velocities of the stations. The daily GPS data collected at CORS-TR stations between June 28, 2008 and January 01, 2015 (see Ozdemir, 2016) are processed first in this study. Results are compared with those generated in GDM. It has been proved that the strategy used here produces superior results (since then, the developed strategy has also been adopted by GDM). Later, we increased the number of the IGS sites (which tie the solutions to a global frame) included in the analyses from 12 to 22 (to reach even more robust results), and reprocessed the whole data set between June 28, 2008 and March 17, 2018 (see Ozdemir and Karslıoğlu 2019).

### **5.1.3 GPS Data Processing**

Since we have a network that is large in geographic extent, we first appointed the stations to a number of sub-groups to increase the speed of the data processing. To this end, we formed five sub-groups considering base lengths by using the “netsel” subnetting program (Herring et al., 2018a). The study area was spaced with a 1x1 degree graticule. The sum of the reciprocals of the distances to the stations was assigned as a density value to each grid point. The grid point with the largest density value was selected as the centre of the first sub-group to which 50 closest stations were assigned. The procedure was applied to the remaining stations iteratively, and four sub-groups were formed. To tie these groups, a fifth group was created which is composed of several common stations.

In addition, for the reference frame definition, 12 IGS stations (ADIS, ANKR, BUCU, GRAS, GRAZ, KOSG, NICO, NOT1, POLV, POTS, RAMO, ZECK) were included in all groups. The number of the IGS stations was increased to 22 (ANKR, ARTU,

BOR1, CRAO, GLSV, GRAZ, ISTA, KIT3, MATE, NICO, NOT1, POLV, POL2, POTS, RAMO, TUBI, VILL, WSRT, WTZR, YEBE, ZIMM, ZWE2) in the second round of processing (Ozdemir and Karşlıoğlu, 2019), taking into account the geographic coverage and repeatabilities. The IGS sites included in the analyses are displayed in Figure 5.3.

We processed the GPS phase data by using GAMIT (GPS Analysis at MIT) software [release 10.61 (Herring et al. 2015a)], and produced the solutions including the parameter estimates and the corresponding variance-covariance matrices. These solutions were later combined by using the GLOBK (Global Kalman filter VLBI and GPS analysis program) software (Herring et al., 2015b), to generate the time series and to estimate the final positions and the velocities.

Relative positioning was implemented in the analyses by using the single and double differenced phase data. Correlations due to differencing were taking into account (Schaffrin and Bock, 1988). Triple differenced phases were used only to get the preliminary estimates of the parameters and to detect the cycle slips. Unrepaired cycle slips were included in the adjustment as extra parameters to be estimated. Differencing techniques and their purposes are explained in Chapter 2. On the other hand, relative positioning including clock estimation (without eliminating the clock bias through differencing) was used to compute the undifferenced phase residuals through which the atmospheric and ionospheric slant delays can be monitored.

We used the Melbourne-Wübbena combination (Melbourne, 1985; Wübbena, 1985) to resolve the L1-L2 cycles first, and then L1 cycles, and fixed the ambiguities to integers. Unresolved ambiguities were left as real-valued estimates.

IGS reprocessed final orbits (SP3 final) were used for the satellite positions. The accuracy and the latency of these orbits are  $\sim 2.5$  cm, and 12-18 days, respectively (see Table 2.1). In addition to the initial positions and the velocities of the satellites, the gravitational and the non-gravitational forces acting on the satellites must be modeled to accurately describe the trajectories. The positions of the satellites as a function of time were generated by numerical integration.

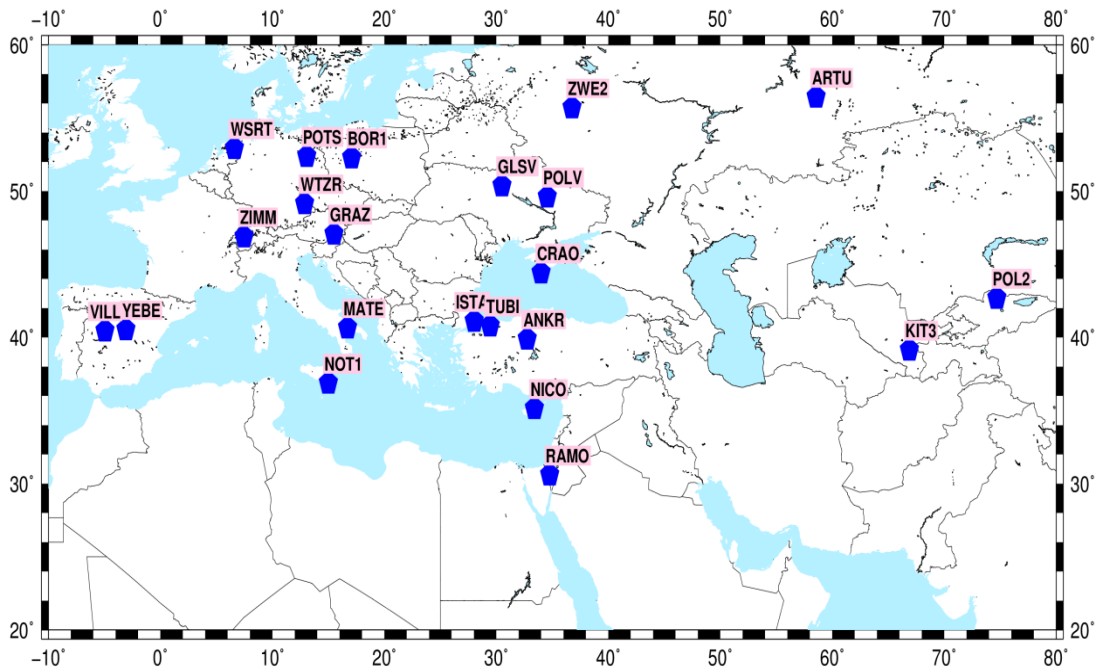


Figure 5.3. IGS sites included in the analyses

The phase and code pseudo-range observations may change due to the variations in the phase centers of the antennas, both at the satellite and receiver stations. Thus, for satellite antenna phase center corrections, nadir angle-dependent absolute phase center variations (PCVs) were used. For ground antenna phase center corrections, elevation and azimuth-dependent absolute phase center variations were incorporated.



The model of Bar-Sever (Bar-Sever, 1995) was applied to account for the yaw-axis attitude of the satellites.

For zenith hydrostatic delays and mapping functions (to extend the delays to other elevation angles), Vienna Mapping Function 1 (Boehm et al., 2006) grid files were used. The first order effects of the ionosphere were reduced to negligible levels, by using the combinations of the phase measurements. Higher order ionospheric effects were neglected. These effects are worthy of regard at the equatorial zones mainly (Petrie et al., 2010).

To consider the atmospheric loading, we included the non-tidal atmospheric loading files (Tregoning and Watson, 2009). Following the 2010 IERS (International Earth Rotation and Reference Systems Service) conventions (Gerard and Luzum, 2010), we took account of the solid Earth and pole tide corrections. For the ocean tide loading corrections, we used FES2004 tide model (Lyard et al., 2006).

The functional model between the parameters (relative positions of the stations and tropospheric zenith delays, and associated variance-covariance matrices) and the measurements (double differenced phase observations) were established through a weighted least squares algorithm. Since this model is non-linear, we produced two solutions. We received the a priori coordinates of the stations with a precision up to one meter in the first solution, and we examined the residuals. We realized the second solution with the updated coordinates. We applied loose constraints to the final estimates (10 m for coordinates, 0.5 m for zenith delays), not to bias the combinations which are realized later by GLOBK. The details of the analyses and the processing strategy can also be found in Ozdemir and Karşlıoğlu (2019) and in <http://www.epncb.oma.be/densification/analysiscentres.php>.

## 5.1.4 Quality Assessment

### 5.1.4.1 Satellite Visibility

We calculated the average number of satellites observed, for at least one hour per day for each station. AGRD is the station with the largest average number of satellites observed daily (9.74). Stations with the poorest satellite visibility are given in Table 5.1. We examined the environmental conditions of these stations and detected the presence of large natural barriers which can block the GPS signals. This can be also seen in the sky plots (satellite visibility graphics) which display the phase residuals. Temporary or constant high residuals are generally due to tropospheric fluctuations, or multipath, respectively. It is seen in Figure 5.4 that a hill located on the west side of the CATK station obstructs the GPS signals at the lower elevation angles. No considerable degrading effect of the satellite visibility was detected on the position estimates of the stations listed in Table 5.1.

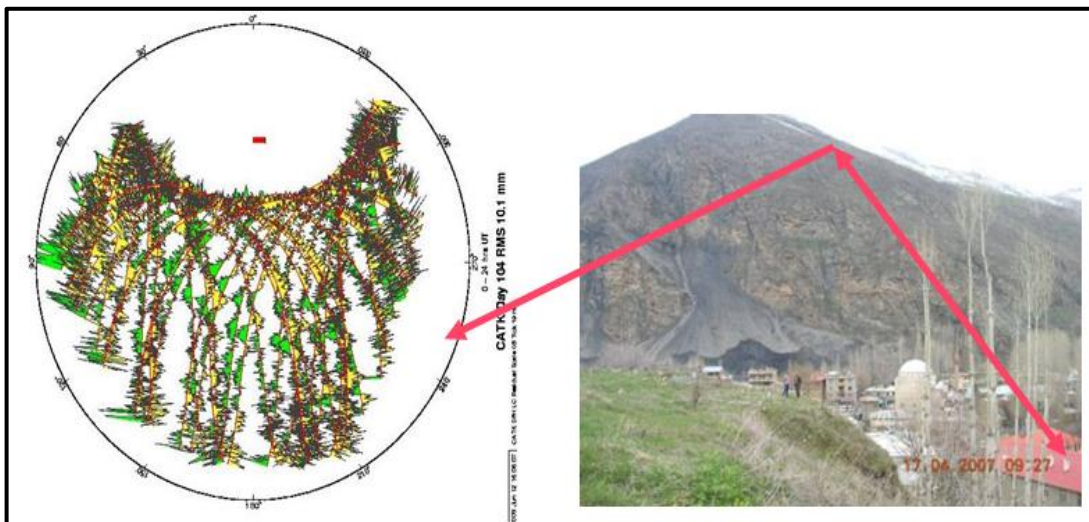


Figure 5.4. The sky plot (yellow: positive residuals, green: negative residuals) of the CATK station, and the hill blocking the GPS signals.

Table 5.1. CORS-TR stations which have the poorest satellite visibility (Table from Ozdemir, 2016).

Station	Average number of satellites observed daily
CATK	7,47
SIRT	7,89
GUMU	7,94
FEEK	8,06
GIRS	8,14

#### 5.1.4.2 Antenna Phase Center Models

The GPS observations are referred to the antenna phase centre which does not necessarily coincides with the geometric centre of the antenna. We plotted the LC phase residuals as a function of time for each station to see whether there is a problem in the antenna phase center models. Such a plot is given in Figure 5.5. It is seen that the residuals are distributed normally with a low level of noise, decreasing with the increase of the elevation angle.

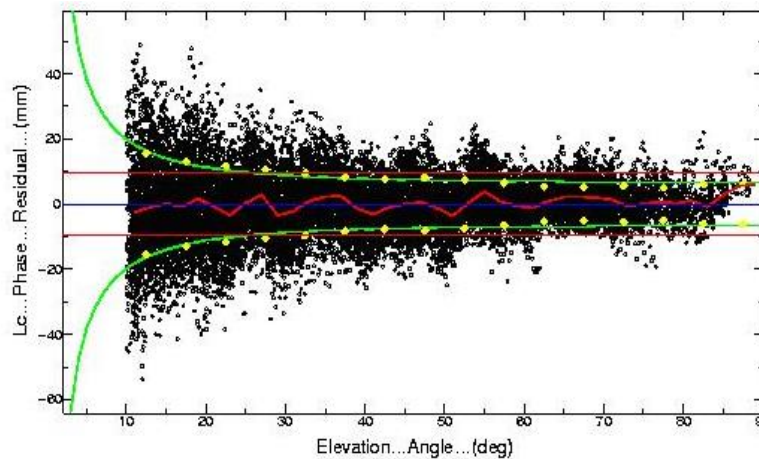


Figure 5.5. LC phase residuals vs. elevation angles for EDIR station.

A problematic plot is illustrated in Figure 5.6, where the residuals display a systematic pattern, possibly due to the misidentification of the antenna. We examined the LC phase residuals of all the CORS-TR stations. No bias was detected originating from the antenna phase center problems.

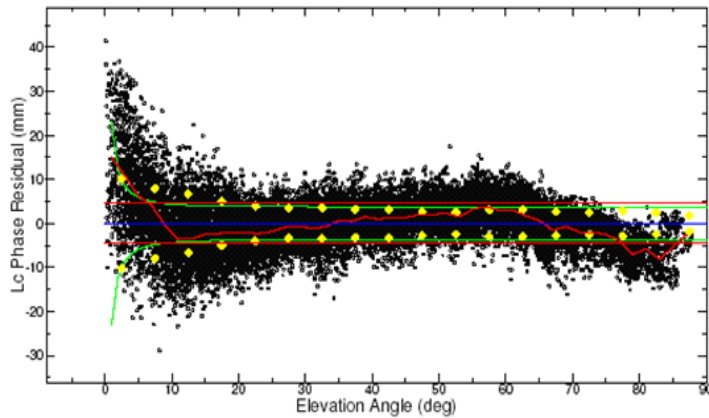


Figure 5.6. LC phase residuals showing bad pattern (Figure from Herring (2012)).

### 5.1.4.3 One-way LC Phase Residuals

For each station, we calculated the averages and the standard deviations of the daily LC phase residuals' RMS (root mean square) values to evaluate the quality of the basic observables used in the estimation of the parameters. Typically we expect to have values between 3 and 9 mm. Although values between 10 and 15 mm are high, the noise can still be considered as acceptable. Values greater than 15 mm might be due to receiver problems, multipath, bad weather conditions, short data span, bad a priori coordinates (Herring et al., 2018). We present the histogram of the mean RMS of the LC phase residuals in Figure 5.7. We see that, although there are some CORS-TR stations with high level of noise, all RMS values are below 15 mm. We give the stations which have the highest RMS values in Table 5.2. As expected consequently, the daily coordinate uncertainties of these stations are also high.

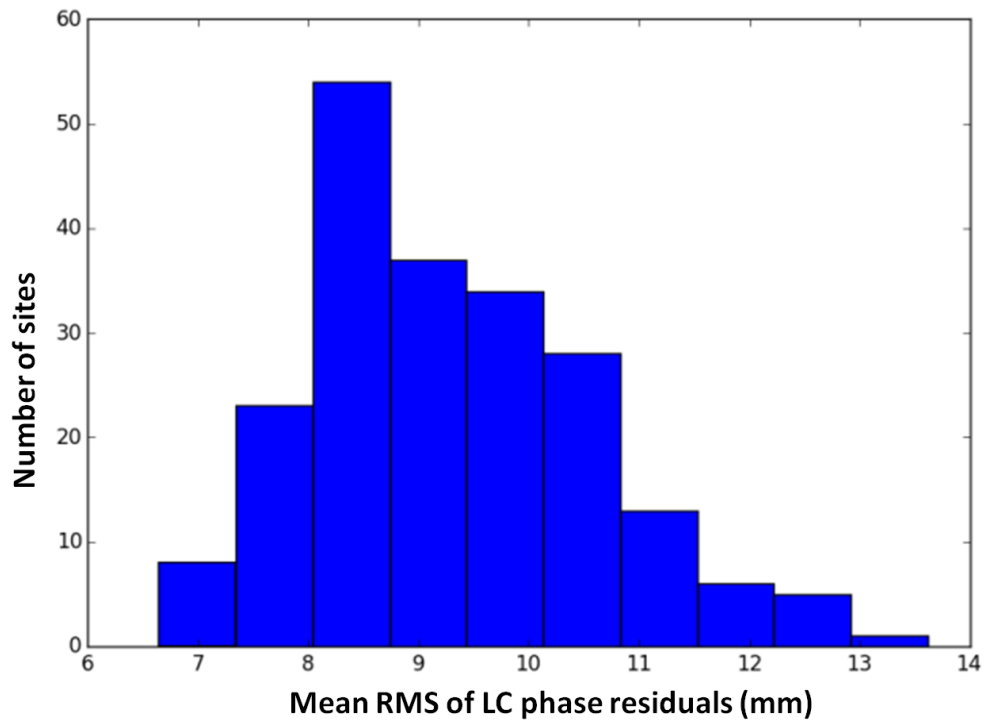


Figure 5.7. The histogram of the mean RMS of the LC phase residuals. (Figure from Ozdemir (2016)).

Table 5.2. The highest mean RMS values and associated standard deviations.

<b>STATION</b>	<b>Mean RMS of LC residuals</b>	<b>Standard Deviation of LC residuals</b>
DATC	13.62	1.92
AYD1	12.60	1.52
RDIY	12.37	1.12
IPS1	12.30	2.01
HAT1	12.29	2.66
RZE1	12.22	1.96
MUR1	12.06	1.09
SIRT	11.94	1.44

#### 5.1.4.4 Multipath

We obtained the daily multipath values (mp1 and mp2) in meters for the *L1* and *L2* signals collected at each station, by using the TEQC software (Estey et al., 1999). Later we calculated the mean values of the multipaths for the analysis period. Multipaths stay  $\geq 3\sigma$  away from the means were also examined to see whether the outliers are constant or temporary. In Table 5.3, we give the stations which are exposed to high multipath effects.

Table 5.3. Stations with the highest multipaths (Table from Ozdemir (2016))

STATION	MEAN MP1	# MP1 OUTLIER	STATION	MEAN MP2	# MP2 OUTLIER
BTMN	0,7782	156	BTMN	0,7829	157
BAYB	0,5524	5	BAYB	0,5695	8
GIRS	0,4766	20	KAYS	0,5538	5
KIRS	0,4722	34	ERZR	0,5432	12
RDIY	0,4633	16	ANRK	0,5168	27
AKDG	0,4529	30	RDIY	0,5144	20

We plotted the multipaths at BTMN station as a function of time (see Figure 5.8), to understand the behavior of the multipaths. High multipath values are not constant, but concentrated in the summer seasons. This is also the explanation of the high number of outliers seen at BTMN station in the Table 5.3. This situation also causes high uncertainties in the coordinates of the station in the summer months.

#### 5.1.4.5 Proximity to the Active Faults

We investigated the closeness of the CORS-TR stations to the active faults presented in Figure 5.1. The motion of the stations very close to the faults might be governed

mainly by the creep rates along the faults. In Table 5.4, the stations within 2 km of the active faults are listed.

Table 5.4. The stations within 2 km of the active faults (Table from Karşlıoğlu et al. (2017))

YENC	MUGL	BURS	HATA	ERZI	SEMD
KIKA	DENI	ESKS	MARA	BING	OZAL
IZMI	DINA	IZMT	TOKA	ERZR	
AYDI	KUTA	HEND	RDIY	HAKK	

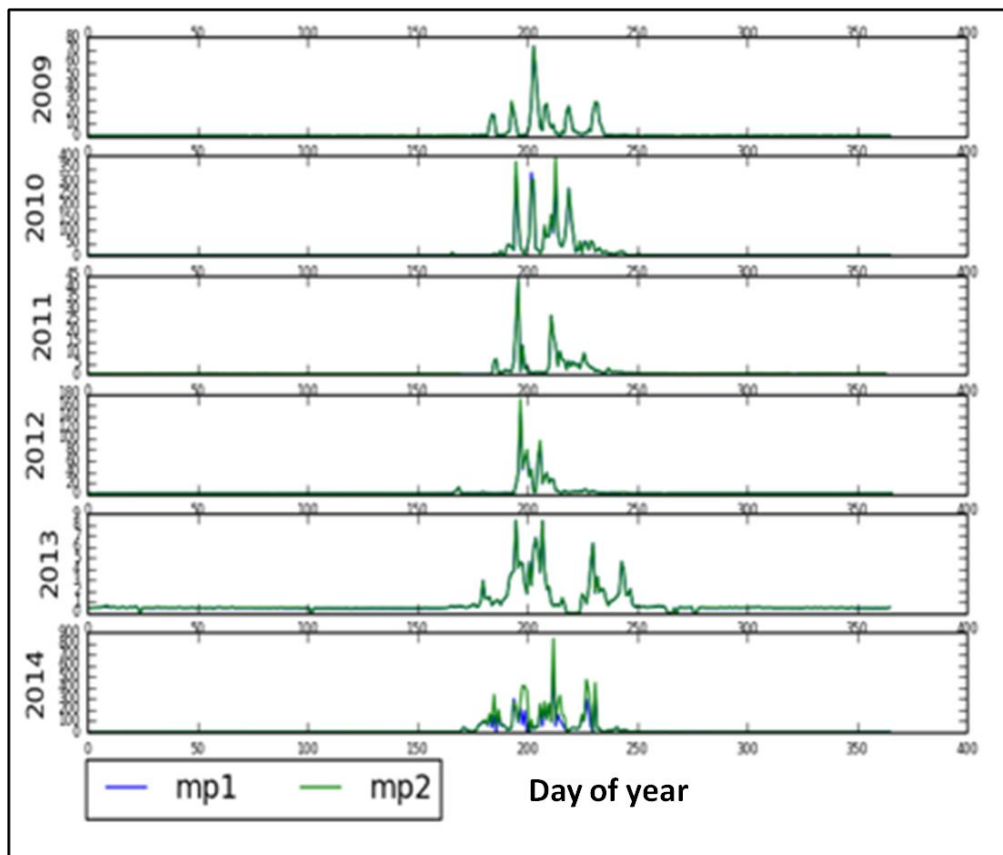


Figure 5.8. The multipaths at the BTMN station as a function of time. (Figure from Ozdemir, 2016).

### 5.1.5 Time Series Analysis

We generated the time series twice. The first set of time series are in a global frame. The purposes of the first generation are to (1) detect and clean the outliers, (2) handle the jumps due to known or unknown signals, (3) manage the data gaps considering their lengths (to interpolate or to divide the time series into pieces), (4) examine the repeatabilities and evaluate the precision of the results, and (5) obtain the random walk noise models. Following the optimization of these processes, precise coordinates and velocities, and associated realistic uncertainties were estimated. The second set of time series were expressed in a regional frame based on the coordinates of the carefully selected local sites, for the purpose of reducing Common Mode Error.

To express the daily solutions in the International Terrestrial Reference Frame 2008 (ITRF2008) (Altamimi et al., 2011), a six-parameter transformation (3 translation and 3 rotation parameters) was performed. The transformation parameters were estimated iteratively (in four iterations). In each iteration, the IGS sites with high uncertainties and discordant with the published ITRF2008 coordinates were eliminated in the stabilization. The obtained RMS values in reference frame definition are demonstrated in Figure 5.9, together with those obtained through the GDM's old strategy (which was abandoned in 2015). In the old strategy, the reference frame was defined through the "global stabilization" method, where the regional solutions were combined with the global solutions analyzed by the SOPAC (Scripps Orbit and Permanent Array Center, <http://sopac-csrc.ucsd.edu/>) analysis centers. The RMS values are around 2 mm, and the improvement with respect to the old strategy is clear.

We scrutinized the daily coordinate uncertainties of the stations. In Table 5.5, stations with the highest mean coordinate uncertainties are presented. We achieved also improvements with our strategy in the daily coordinate uncertainties of the stations.



An example of this improvement is shown in Figure 5.10, where the daily uncertainties of IZMI station are displayed.

Table 5.5. Stations which have high mean (M) daily coordinate uncertainties in mm.

STATION	EAST M ( $\sigma$ )	EAST $\sigma$ ( $\sigma$ )	STATION	NORTH M ( $\sigma$ )	NORTH $\sigma$ ( $\sigma$ )	STATION	UP M ( $\sigma$ )	UP $\sigma$ ( $\sigma$ )
SIRT	3,16	0,48	SIRT	3,67	0,48	SIRT	16,85	2,37
DATC	3,10	0,54	DATC	3,34	0,49	DATC	13,23	2,18
DATC	2,78	0,37	RDIY	3,03	0,29	CATK	11,12	1,48
AYD1	2,71	0,33	DATC	2,98	0,39	ANRK	11,07	8,70
RDIY	2,60	0,26	ARTV	2,95	0,34	RDIY	10,99	1,12
DIYB	2,60	0,27	RZE1	2,94	0,46	DATC	10,95	1,45
MURA	2,58	0,36	MURA	2,90	0,39	CATK	10,75	1,38
MUR1	2,56	0,26	DIYB	2,85	0,28	ARTV	10,65	1,28
IPS1	2,56	0,37	AYD1	2,84	0,35	MURA	10,63	1,36
CATK	2,55	0,34	TRBN	2,83	0,67	SEMD	10,49	1,48
RZE1	2,52	0,40	MUR1	2,81	0,28	AYD1	10,47	1,33
SEMD	2,52	0,41	IPS1	2,80	0,34	DIYB	10,32	1,05
HAT1	2,49	0,24	TVAN	2,80	0,57	MUR1	10,32	1,07
TRBN	2,49	0,64	CATK	2,78	0,35	IPS1	10,18	1,38
CATK	2,49	0,34	MURA	2,75	0,29	TVAN	10,13	2,34

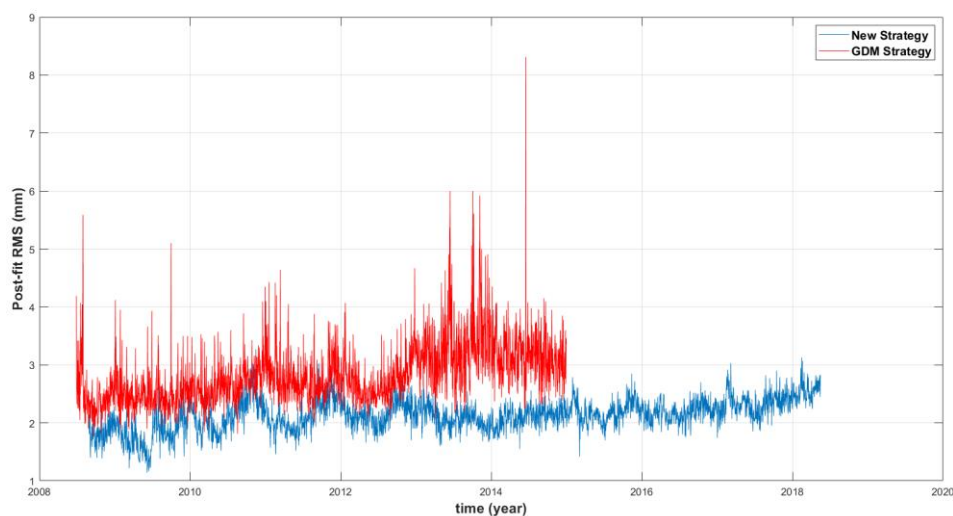


Figure 5.9. The RMS values obtained in the reference frame definition (red: obtained through the old strategy which was abandoned in 2015, blue: obtained through the new strategy).

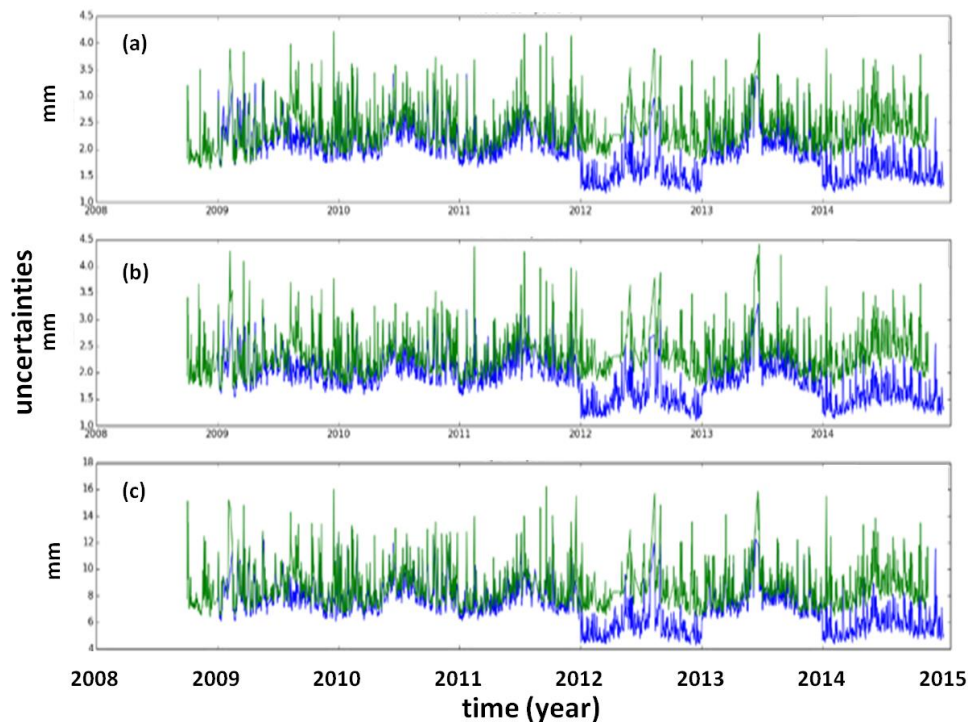


Figure 5.10. The daily coordinate uncertainties of IZMI station obtained with the old (green) and the new (blue) strategy, (a) north, (b) east, (c) up components (Figure from Karshoğlu et al., 2017).

We present the means of the daily uncertainties during the analysis period in Figure 5.11. Decrease in the uncertainties of all sites with respect to the old strategy is clearly seen.

One of the statistical measures of goodness of fit is the WRMS (Weighted Root Mean Square) which expresses how the individual observations (e.g., daily coordinate estimates) are distributed about a fit (might be obtained e.g., with a linear regression) to the observations. Thus, it gives an opinion about the precision (repeatabilities) of the observations. WRMS is defined as,

$$WRMS = \left[ \frac{\frac{1}{N-1} \sum_{i=1}^N \frac{e_i^2}{\sigma_i^2}}{\sum_{i=1}^N \frac{1}{\sigma_i^2}} \right]^{1/2}, \quad (5.1)$$

where  $N$  is the number of the observations,  $e_i$  is the  $i$ th residual, and  $\sigma_i$  is the uncertainty of the  $i$ th observation (Spinler et al., 2010). The histograms of the repeatabilities of all sites are displayed in Figure 5.12. The final coordinate and velocity estimates of the sites with high repeatabilities (especially  $> 3$  mm) are of high uncertainties.

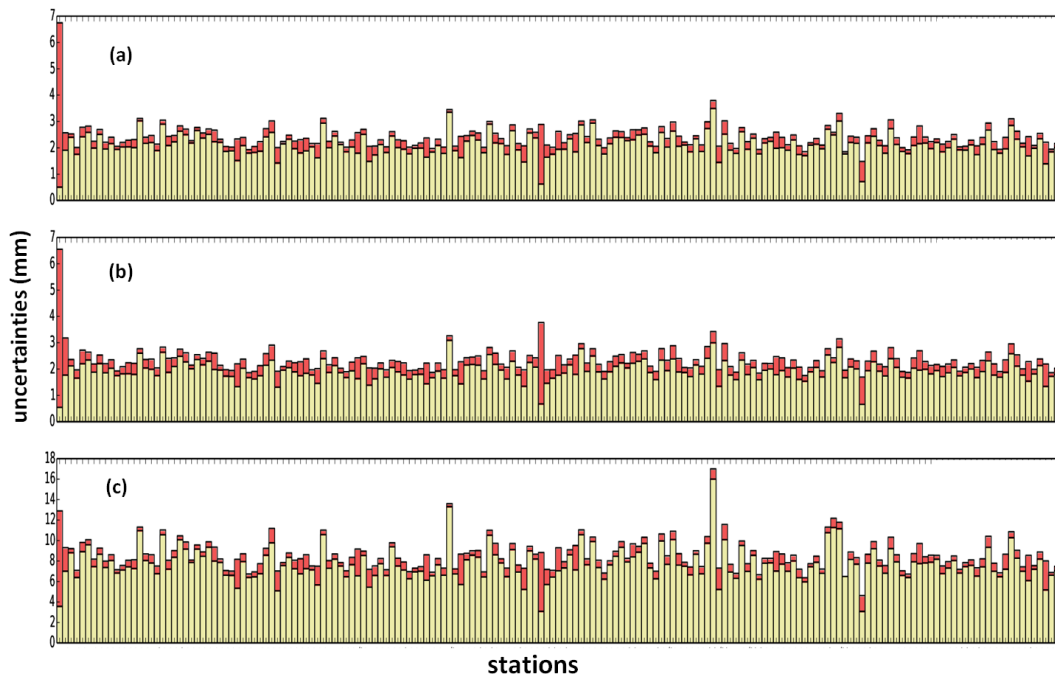


Figure 5.11. Daily coordinate uncertainties of all CORS-TR stations (red: old strategy, yellow: new strategy) for the (a) north, (b) east, and (c) up components (Figure from Karshioğlu et al., 2017).

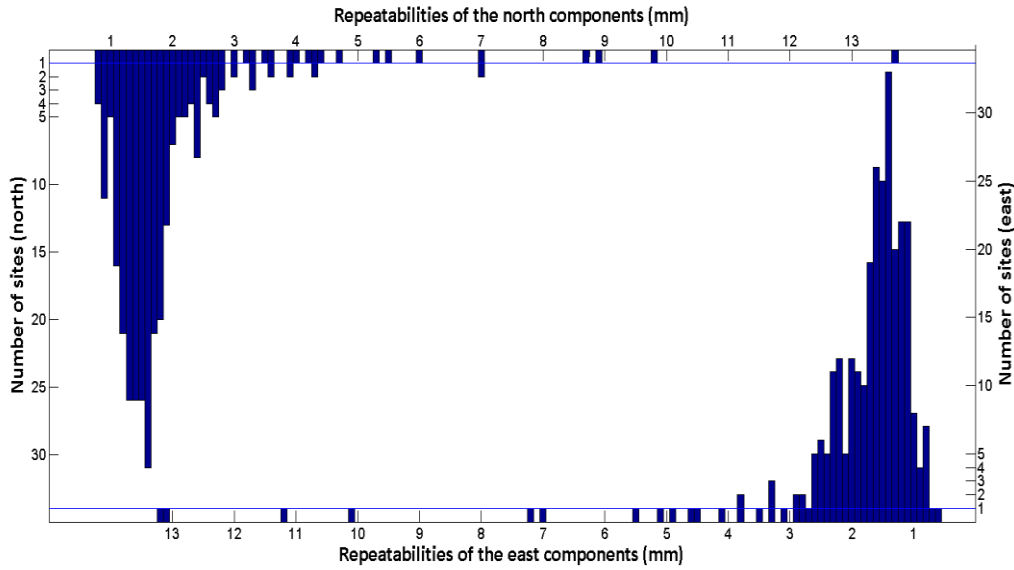


Figure 5.12. Repeatabilities (obtained after cleaning the outliers) of the north (top-left) and the east (bottom-right) components of the CORS-TR stations (Figure from Ozdemir and Karshoğlu, 2019).

After the inspection of the generated time series, we detected that 24 sites experienced coseismic displacements due to five earthquakes with magnitudes over 6.0 (see Table 5.6 and Figure 5.13). Antenna mast at the site DIYB was raised up on November 04, 2011. The data between July 15, 2013 and January 09, 2014 at the EMIR station were excluded. The lightning rod mounted on the antenna mast between these days caused anomalous behavior in the time series. On the other hand, unknown sources led to trend changes in the time series of 9 stations (AFYN, ANKR, DATC, EDIR, GYUR, RZE1, SARV, SEMD, ZONG). 35 stations have been replaced due to mostly operational reasons during the analysis period.

Table 5.6. Sites experienced coseismic displacements during the analysis period (Table from Ozdemir and Karshioğlu, 2019).

Earthquake	Epicenter		Date	M	Affected CORS-TR Sites
	$\lambda^*$	$\phi^*$			
Elazig	39.99	38.86	08.03.2011	6.1	BING
Van	43.51	38.72	23.10.2011	7.1	AGRD, BASK, CATK, HAKK, HORS, IGIR, KRS1, MURA, OZAL, SEMD, SIRN, TVAN, VAAN
Gokceada	25.39	40.29	24.05.2014	6.9	AYVL, BALK, CANA, IPSA, YENC
Karaburun	26.37	38.93	12.06.2017	6.3	AYVL, CESM
Gokova	27.41	36.93	20.07.2017	6.6	AYD1, DATC, DIDI

\* Longitude and latitude in decimal degrees  
(Earthquake information is from USGS earthquake catalog)

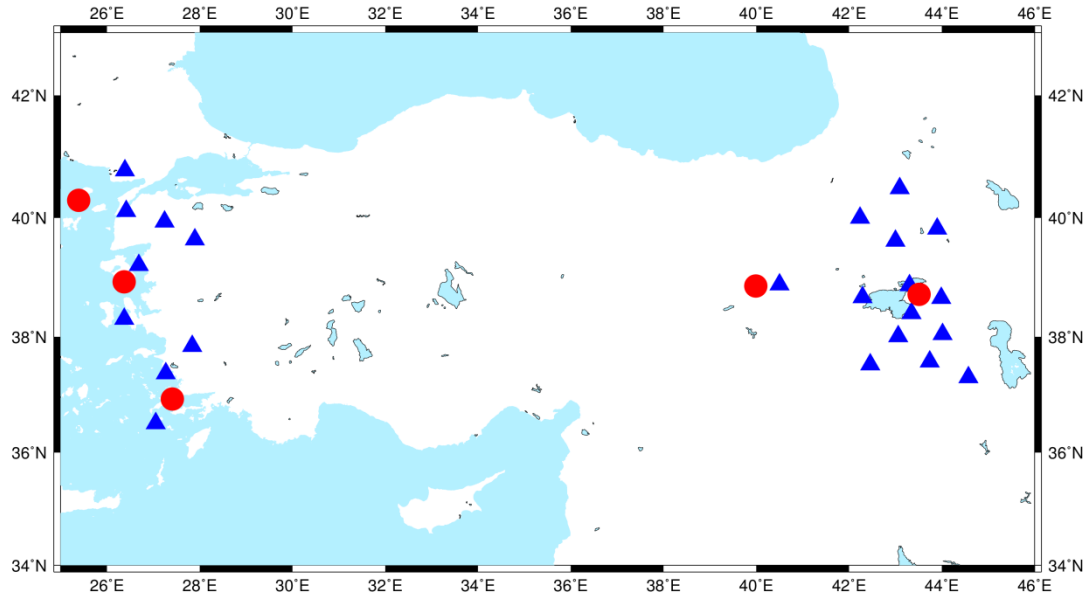


Figure 5.13. The earthquakes (red circles) and the affected CORS-TR sites (blue triangles)

Detecting the outliers in GPS time series visually is common. However this is a subjective and very time-consuming approach which necessitates deep experience. We first detected and cleaned the daily solutions which have uncertainties over 10 cm as outliers. Later, we calculated the inter-quartile ranges (IQR) of the time series which were detrended by using the iteratively reweighted least squares (IRLS) algorithm. Lower (LB) and upper (UP) bounds were calculated as follows,

$$LB = Q_1 - \alpha/2 * IQR , \quad (5.2)$$

$$UB = Q_3 + \alpha/2 * IQR , \quad (5.3)$$

where  $Q_1$  and  $Q_3$  are the lower and upper quartiles, respectively (Tukey 1977). Daily solutions beyond these bounds were removed also as outliers. To avoid removing the informative data, which might be a part of e.g., some periodic or nonperiodic signals existent in the time series, rather than being outliers, only the extreme outliers were cleaned by selecting  $\alpha$  as 6 (resulted in 1.22% data removal). If we had selected  $\alpha$  as 3 (which is equivalent to retaining data within about  $\pm 3.0\sigma$ ), we would have removed 5.42% of the data in total. The outlier detection is illustrated in Figure 5.14.

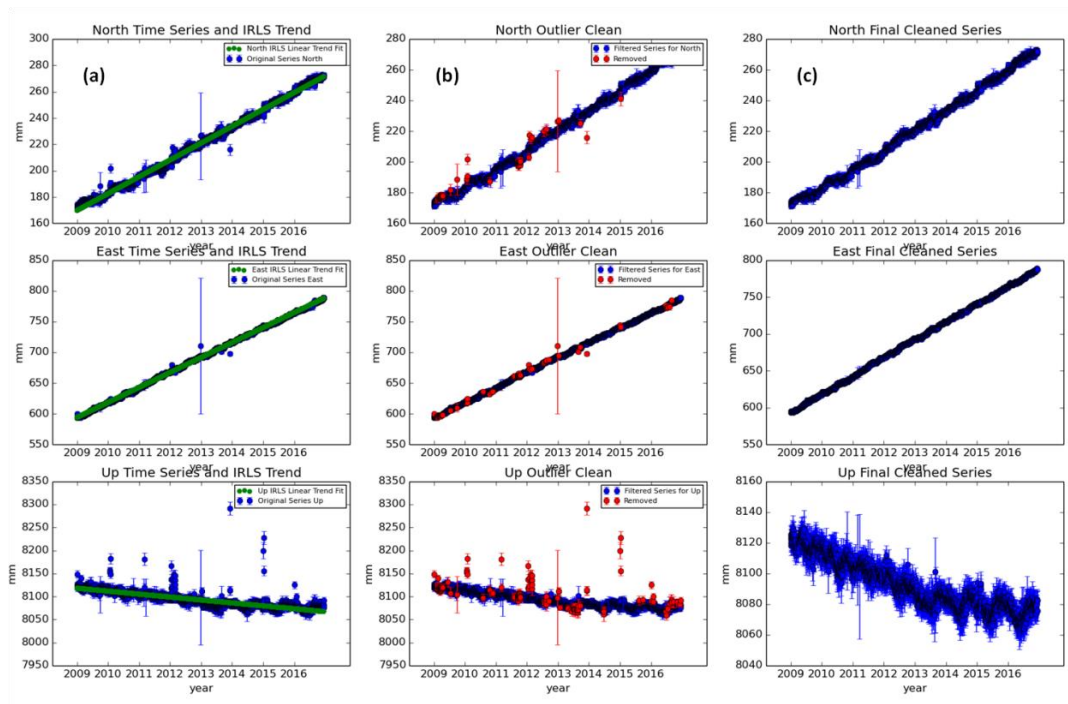


Figure 5.14. The outlier detection in the north, east and up components (from top to bottom) of ZONG station , (a) the original time series and the trend, (b) detected outliers, (c) cleaned time series.

Several studies have shown that noise in GPS time series cannot be assumed simply white in time, but also exhibits colored characteristics (e.g., Zhang et al., 1997; Mao et al., 1999; Williams et al., 2004; Beavan, 2005; Amiri-Simkooei et al., 2007; Langbein, 2008; Santamaria-Gomez et al., 2011; Wang et al., 2011). Pure white noise assumption leads to unrealistically optimistic uncertainties of the parameters. We used the time series residuals to attain the random walk noise models by using the “realistic sigma” algorithm (Herring, 2003), which were later implemented in the GLOBK software in the parameter estimation. With the realistic sigma model, the averages of the residuals for each coordinate component are calculated for increasingly growing time intervals. The increase in the  $\chi^2/dof$  ( $dof$  : degrees of freedom) values are computed for these averages and the correlation time is estimated. In a white noise

assumption,  $\chi^2/dof$  values are independent of the time averages. However, we see in GPS time series that the change in these values are correlated with time (see Figure 5.15).

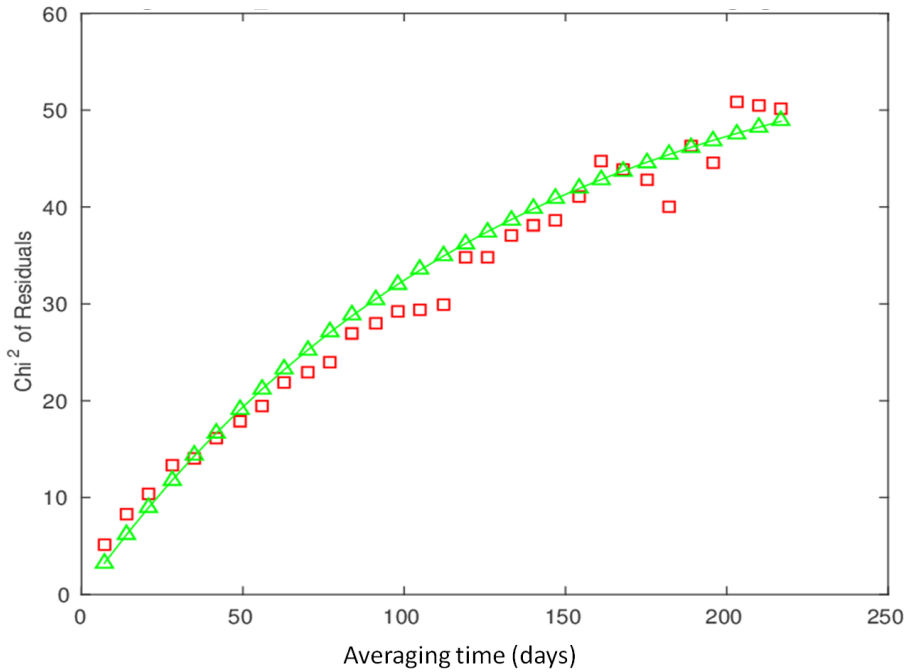


Figure 5.15. The realistic sigma curve (green) for the north component of BAYB station.

### 5.1.6 Overview of Analysis Results

CORS-TR system is gaining growing importance in Turkey. Today, the cadastral works realized based on the CORS-TR derived coordinates are recognized officially by General Directorate of Land Registry and Cadastre (GDLRC). Although the subscription to the system is not free of charge, it has become an indispensable tool especially for the land surveyors, since it provides cm-level precision in a couple of



minutes without long lasting GPS surveys. On the other hand, static GNSS data collected at base stations might be utilized in various Earth science studies. Thus, the quality of the observations collected at the reference stations must be determined well, and the coordinates and velocities of the stations must be estimated precisely.

These studies are carried out in General Directorate of Mapping (GDM) since the establishment of the system (late 2008s). However the GPS analysis strategies evolve over time, and those adopted in GDM have never been tested and validated externally. Hence, we processed the whole CORS-TR GPS data set twice independently within the scope of a project supported by Scientific and Technological Research Council of Turkey (TUBITAK) under the grant number 113Y511 (Karşlıoğlu et al., 2017). Since the superiority of our approach has been proven, it has been also adopted in GDM. The main differences between the strategies are summarized in Table 5.7.

The daily uncertainties of the coordinates have been lowered with the new strategy. The RMS values in the reference frame definition have been decreased. The time-consuming subjective outlier detection phase has been eliminated. By accounting for the random walk noise models, realistic velocity uncertainties have been obtained. The problematic stations with high WRMS values and/or poor receiver performance have been reported. Many of these stations (such as, ADAN, DENI, KAPN, INEB, MALZ) have been relocated later by GDLRC. The time series have been expressed in a regional frame based on the selected fiducial CORS-TR stations which have low uncertainties and are homogeneously distributed. Hereby we reduced the daily dispersion on the time series (to be demonstrated in the following sections). Such CME-reduced CORS-TR time series were generated for the first time in the literature.

Table 5.7. Comparison of the GPS analysis strategies between General Directorate of Mapping and this study.

	<b>GDM</b>	<b>This study</b>
subnetting	visual	base-length based
zenith hydrostatic delays	GPT2	VMF1
atmospherial loading	neglected	considered
satellite orbits	estimated	fixed
reference frame definition	global stabilization	regional stabilization
outlier detection	visual	automatic
noise	white	white + random walk

### 5.1.7 Velocity Field

The reference frame for the coordinate and velocity estimation was defined through a 12-parameter (3 rotations, 3 translations and their rates) transformation, by imposing general constraints (Dong et al., 1998) on the positions and velocities of the IGS stations. The transformation parameters were estimated by minimizing the residuals of the IGS stations with respect to ITRF2008. An iterative least squares estimation was used, and the height components were downweighted by 10 in variance. We obtained 2.4 mm and 0.3 mm/yr post-fit RMS values for the coordinates and velocities of the IGS stations, respectively.

Pre-earthquake and post-earthquake velocities were estimated separately for the stations listed in Table 5.6. For these stations, we accepted the velocities which were derived from a longer data span as the final velocity estimates. Only the sites having over 2.5 yrs of data were included in the velocity solution, since the velocity estimates from shorter data span can be biased largely due to the annual signals (Blewitt and Lavallee, 2002). To view the velocities with respect to Eurasian tectonic block near



where  $\mathbf{P}$  is the weight matrix,  $n$  is the number of the observations, and  $u$  is the number of the parameters. The properly weighted and independent random observations yield  $\hat{\sigma}_0^2$  to be 1.0, ideally. If our assumption about the covariances of the observations is correct,  $\hat{\mathbf{e}}^T \mathbf{P} \hat{\mathbf{e}}$  random variable would be  $\chi^2$  (chi-square) variable, and equal to the degrees of freedom ( $n - u$ ). The *NRMS* (normalized root mean square) is just the square root of the variance scale factor, and can be calculated explicitly as:

$$NRMS = \left[ \frac{1}{N-1} \sum_{i=1}^N \frac{e_i^2}{\sigma_i^2} \right]^{1/2}, \quad (5.5)$$

where  $N$  is the number of data,  $e_i$  is the  $i$ th residual, and  $\sigma_i$  is the uncertainty of the  $i$ th data point. *NRMS* of 1.0 shows a consistency between the data, model and the assumed observation uncertainties. Values greater than 1.0 indicate that either there are rough errors in the observations, or the associated covariances are worse than we assumed. Values lesser than 1.0 imply that the covariances are actually better than we assumed. We demonstrate the improvements we achieved in the *NRMS* values of the velocity estimates of the IGS sites which were used in the reference frame definition, by incorporating the random walk noise models, in Table 5.8.

Table 5.8. *NRMS* values of the velocity estimates of the IGS sites used in the reference frame definition.

	<b>NRMS</b>		
	<b>East</b>	<b>North</b>	<b>Up</b>
white noise	29.52	21.95	16.52
white + random walk	2.58	2.38	2.02

After the first round of processing between June 28, 2008 and January 01, 2015, we validated our results externally. To this end, we re-estimated the coordinates and velocities of the included stations by applying tight constraints on the coordinates and the velocities of the six IGS stations (ANKR, NICO, NOT1, GRAS, POLV, RAMO). In the selection of these IGS sites, we considered their coordinate uncertainties in the solution published by IGS (IGb08.snx). We compared the coordinates of the other loosely constrained IGS sites (ADIS, BUCU, GRAZ, POTS, ZECK) in our solution later to those published by IGS in ITRF2008 at the epoch 2005.0. We present the obtained differences in the cartesian coordinates, which are mostly about couple mm, in Table 5.9.

Table 5.9. Differences in cartesian coordinates of the selected IGS sites between our and IGS solutions.

<b>Station</b>	<b><math>\Delta X(mm)</math></b>	<b><math>\Delta Y(mm)</math></b>	<b><math>\Delta Z(mm)</math></b>
ADIS	1.44	2.13	1.92
BUCU	0.49	1.75	2.19
GRAZ	0.87	2.11	1.11
POTS	4.74	5.08	9.85
ZECK	3.26	2.65	0.04

### 5.1.8 Common Mode Error Reduction

GPS time series suffer from spatially correlated noise. Such noise is also called “Common Mode Error” (CME). Possible causes of CME might be errors of satellite orbits and reference frame. (Wdowinski et al., 1997; Dong et al., 2006). It originates most likely from the nontectonic sources, since its extent is large in space. CME can

be reduced by stacking/filtering approach (Wdowinski et al., 1997) in which epochwise mean values of the stacked residuals are removed from the individual positions. This approach works well when the assumption of spatial uniformity of CME holds. Spatial filtering was improved more in later studies by taking into account the correlations and distances between neighboring sites (e.g., Nikolaidis, 2002; Tian and Shen, 2016). However, spatial scale of the CME could not be described well. This approach bears the risk of filtering also e.g., slow slips, which might be common to all sites in the study area.

Spatiotemporal filtering of Dong et al. (2006) utilizes PCA and allows non-uniformity in the estimation of CME. PCA and its modified versions later were used widely in spatiotemporal filtering (e.g., Shen et al., 2014; He et al., 2015; Li et al., 2015). However, PCA results need to be studied visually further, and contamination might exist between Principal Components (PCs), due to the orthogonality in PCA, which might cause preventing the detection of the subtle geophysical transients in the initial PCs. Another approach to minimize the CME is to transform the reference frame by a Helmert transformation into a regional reference frame using fiducial local sites (Szeliga et al., 2004; Melbourne et al., 2005; Ji and Herring, 2011). These methods which mitigate the CME, facilitate the detection of the transient signals and have been employed in many geodetic studies (e.g., Lin et al., 2010; Ji and Herring, 2012; Jiang et al., 2012; Blewitt et al., 2013).

We reduced the CME in our time series by translation, rotation and scaling of our network (seven-parameter Helmert transformation). We transformed data in the Eurasia-fixed system into those in a regional frame. We inspected the precise velocity field (see Figure 5.16) which was derived by the techniques explained in the previous sections, and selected 78 CORS-TR stations, whose horizontal and vertical velocity uncertainties are below 0.2 mm/yr and 0.4 mm/yr, respectively. These stations were



the residuals. On the other hand, we also applied a stacking/filtering approach to the detrended Eurasia-fixed time series. We stacked the available individual residuals of each station and calculated their averages at each epoch:

$$R(d) = \frac{\sum_{i=1}^N R_i(d)}{N}, \quad (5.7)$$

where  $R(d)$  is the average of the residuals for day  $d$ , and  $N$  is the number of the stations which have a solution on day  $d$ . The time series were filtered by subtracting the averages from the individual residuals:

$$\hat{O}_s(d) = O_s(d) - R(d), \quad (5.8)$$

where  $\hat{O}_s(d)$  is the filtered residual of the station  $s$  on day  $d$ , and  $O_s(d)$  is the residual of the station  $s$  on day  $d$  before filtering.

As an example, we demonstrate the reduction in the daily dispersion ( $\sigma$ ), by means of the common-mode correction on the north, east and up components of ADIY station in Figure 5.18. In Table 5.10, we display the average improvements in the dispersions after the application to all CORS-TR stations. The overall dispersions were decreased through reference frame transformation by 13%, 17% and 12% in the north, east and up components, respectively. We used the CME reduced time series through reference frame transformation for further investigations.



Table 5.10. The overall daily dispersion in the original and common-mode corrected time series.

	<b>Standard Deviation (mm)</b>		
	<b>North</b>	<b>East</b>	<b>Up</b>
Original	2.01	2.04	5.04
Stacking/filtering	1.79	1.74	4.53
Regional frame	1.75	1.69	4.43

## 5.2 Transient Signal Detection

At present, weak signal detection (WSD) is of great significance in signal processing. WSD refers to an approach which is used to detect and recover the useful (but weak) signal which is usually buried in noise. The “weak” here might have two meanings: (1) compared with that of the noise, the amplitude of the signal in search is low (low signal-to-noise ratio (SNR)), and (2) the absolute amplitude of the signal in search is very small to be detected.

Since the signals are of endlessly varied nature, the success of the WSD methods depends on the signal properties. Thus, there are tens of various techniques, such as fast fourier transform, wavelet transform, filtering, correlation detection, lock-in amplifier, sparse decomposition, chaotic oscillator, differential oscillator, neural networks, higher-order statistics, stochastic resonance etc. The vast majority of the WSD algorithms focus on improving the SNR.

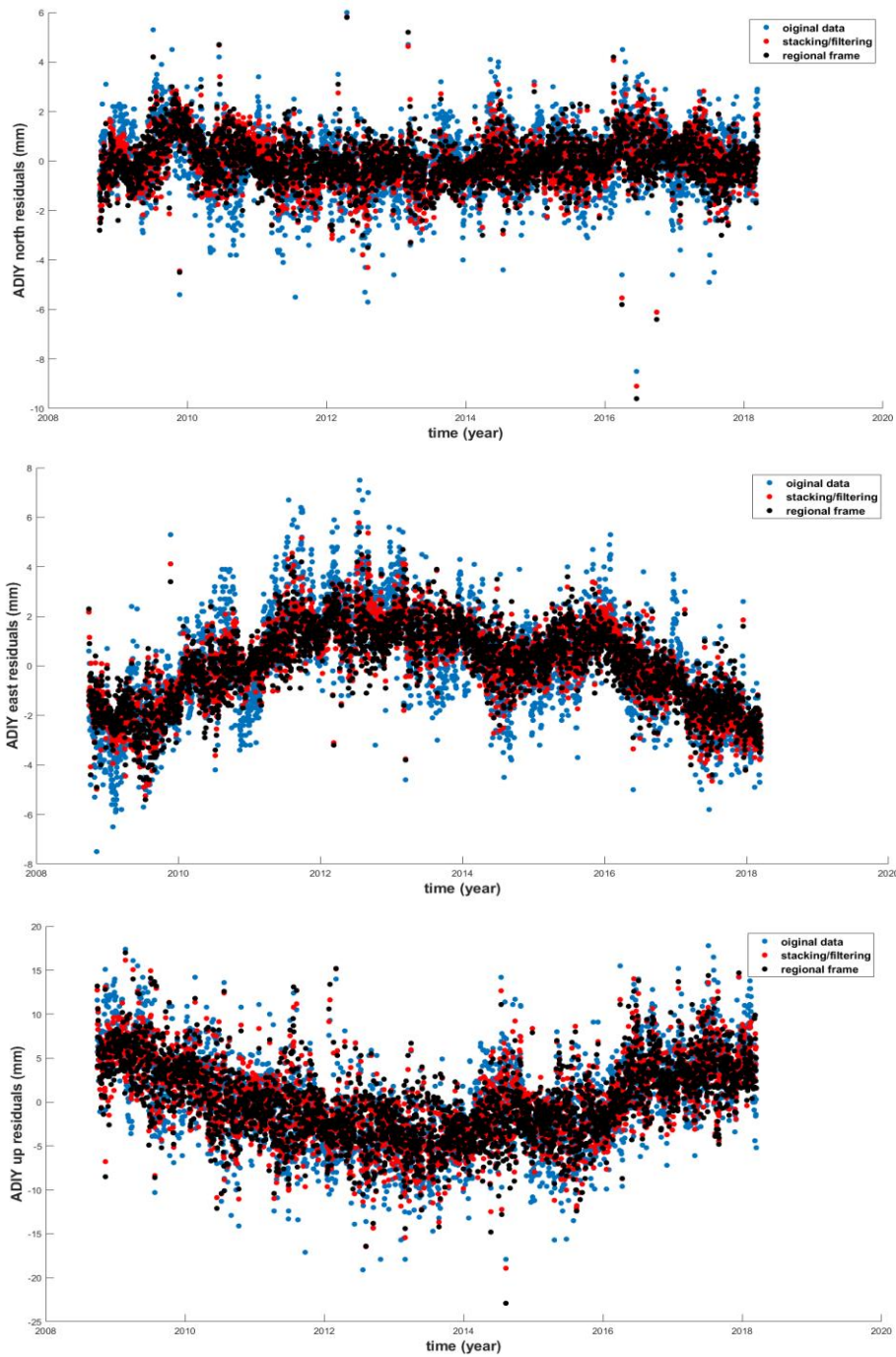


Figure 5.18. The original (blue) and the CME corrected (through stacking/filtering (red), and regional frame transformation (black)) time series of ADIY station (top: north, middle: east, bottom: up components).

A transient signal in GPS time series is also a weak signal which we cannot detect from the actual data. On the other hand, to investigate all time series in a large GPS network one by one is hard. Since the GPS time series include outliers, data gaps, offsets, secular rates, annual and semi-annual signals, spatially and temporally correlated noise, environmental and anthropogenic effects etc., first, it is good to define the characteristics of the transients we are looking for. The features of the transient signals we are searching for can be summarized as follows:

- Their temporal patterns are not similar to those originate from constant motions (e.g., linear plate motions and seasonal signals),
- Their temporal patterns are different from a stochastic noise model,
- They are coherent (seen in multiple sites) in space,
- They are localized (not seen in all sites) in space,
- Their models are of diversified nature that usually cannot be parameterized.

Considering the above statements, it should be also noted that:

- The duration of the data span may be shorter than the temporal extent of the transient signal. Hence, a transient signal might seem to exist persistently in the time series,
- There might be propagating transient signals due to, e.g., slow slip events, which are not coherent in space,
- The geographic extent of a transient might be larger than the GPS network size,
- The spatially correlated CME might not be distributed uniformly in space and in time.

To detect the transient signals having the characteristics listed above, we first processed the GPS data collected at the stations with ultra-high precision analysis techniques explained in section 5.1. We detected and cleaned the outliers. Later we estimated the precise coordinate and velocity field, and diminished the CME using a reference frame transformation by translation, rotation and scaling of the network. We subtracted the known signals from the time series, such as, secular velocities, annual and semi-annual signals and offsets (due to earthquakes, antenna and receiver changes). Hereby, we obtained the CME-suppressed residual time series which contain the noise (white and colored) and the possible transients.

Afterwards, to enhance the SNR in time, we applied Ensemble Empirical Mode Decomposition (EEMD) with the library provided by Luukko et al (2015), and later denoised the residual time series with the denoising procedure explained in Chapter 3. We used cubic splines with the “not-a-knot” end conditions (Wu and Huang, 2009) in envelope interpolation. If the number of extrema is only 2, we used linear interpolation, and if it is only 3, we used polynomial interpolation. To reduce the end effects, we added additional extrema to the ends of the data using linear interpolation of the previous two extrema (Wu and Huang, 2009). We fixed the number of siftings to 10 to promote the dyadic filter bank property of the EMD. The missing data were interpolated using a linear plus seasonal trend. We created an ensemble of a thousand white noise (amplitude of 0.2 of the standard deviation of the corresponding data) added signals, and applied EMD to each of them. The averages of the resulting IMFs were accepted as the true IMFs. An example of the decomposition is illustrated in Figure 5.19 where we used the east component of the ERGN station as the input signal.

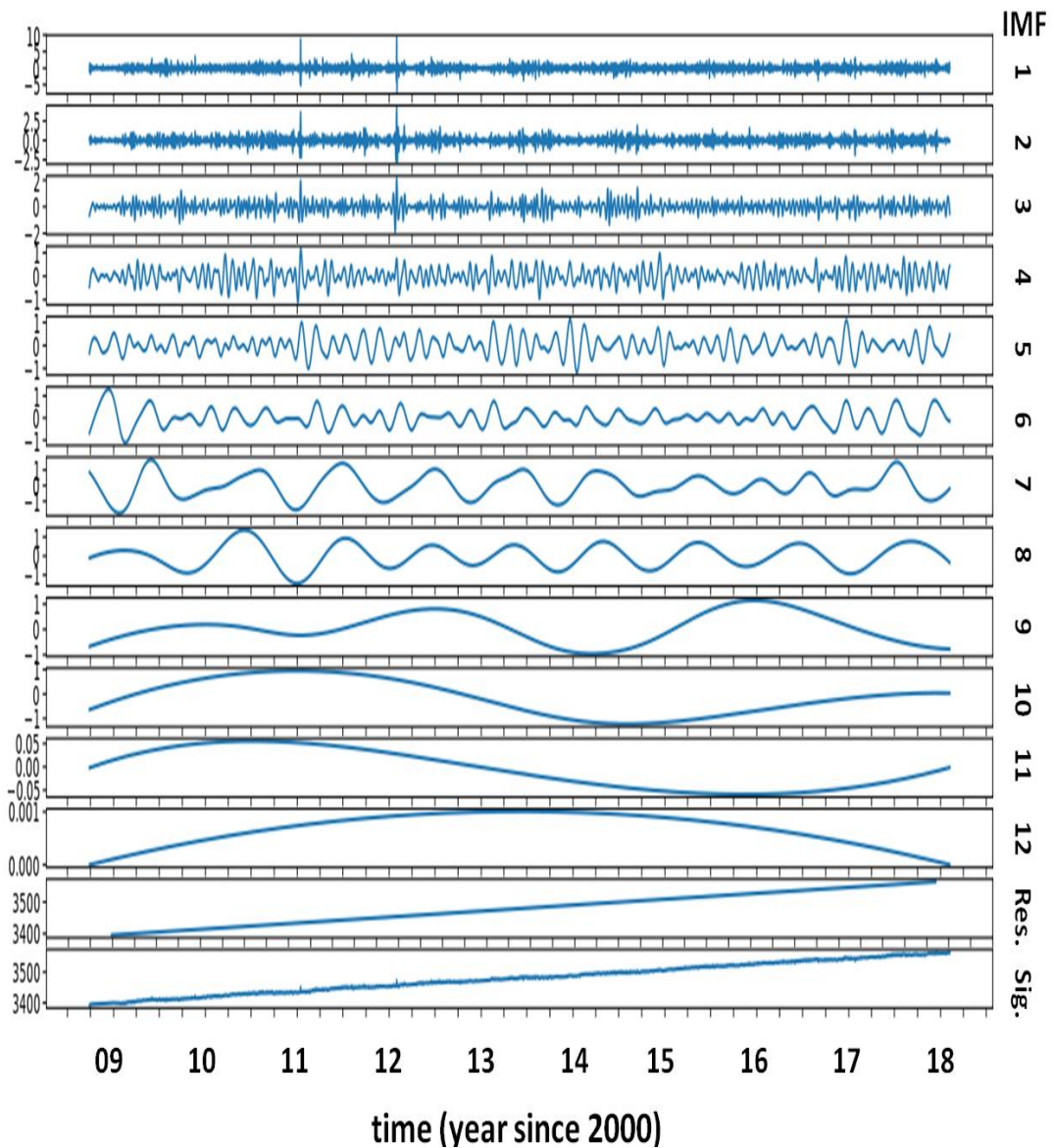


Figure 5.19. EEMD decomposition of the ERGN east component.

As explained previously, the sifting process generates zero references for each IMF, except the residue. So, the signal consists in a slowly varying trend superimposed to a fluctuating process. Thus, observing the cumulative sum of the standardized means of the IMFs starting from the first IMF (which has the highest frequency), and

identifying the point where it significantly departs from zero is the first approach that comes to mind to detect the components of the trend.

In Figure 5.20 we present the evolution of the standardized means of the EEMD results of the ERGN east component. It is seen that after the fifth IMF (detection point), the cumulative sum of the standardized means of the IMFs deviates significantly from zero. Hence, the trend can be constructed by summing up the IMFs with higher indices (6, 7, 8, 9, 10, 11, 12) after the detection point.

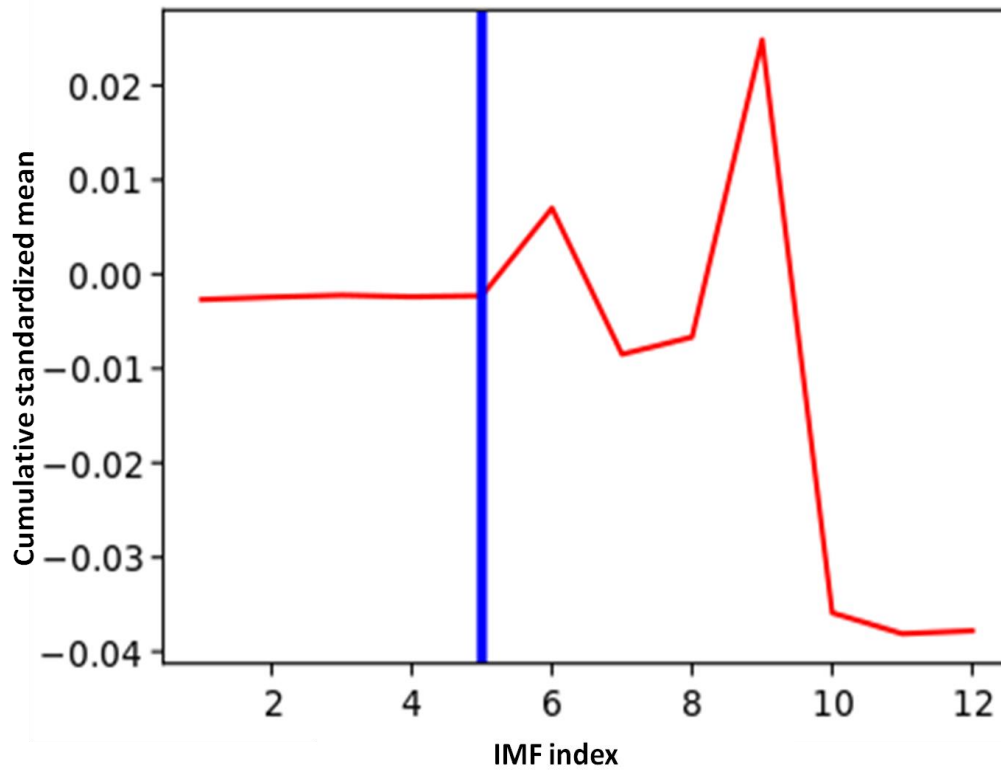


Figure 5.20. Cumulative sum of the standardized means of the EEMD IMF components of the ERGN east component. Addition of sixth standardized mean causes significant deviation from the zero line.

However this is a rough and subjective approach. There is not any strict way of determining the “significant” level of deviation from the zero line. GPS time series are of miscellaneous nature. Too loose a threshold might lead to the exclusion of the IMFs which are actually components of the trend, and the obtained trend might have been contaminated by the noise due to a tight threshold.

As a more precise model, we plotted the logarithm of the variances of the estimated IMFs as a function of the IMF index, and compared them to the IMF statistics in noise only situations, which are controlled by the Hurst index ( $H$ ) and presented in Flandrin et al. (2004, 2005, 2014). We denoised the signals by keeping only the IMFs whose variances exceed the 95% confidence interval determined for  $H = 0.5$  (white noise). The details of the denoising algorithm can be found in Section 3.5. In Figure 5.21, we illustrate the identification of the significance of the IMFs obtained by the EEMD of the ERGN east displacements. It is seen that the IMFs with 5, 6, 7, 8, 9, 10 and 12 indices are considered significant. In Figure 5.22, we display the denoising results of both standardized mean and IMF statistics methods.

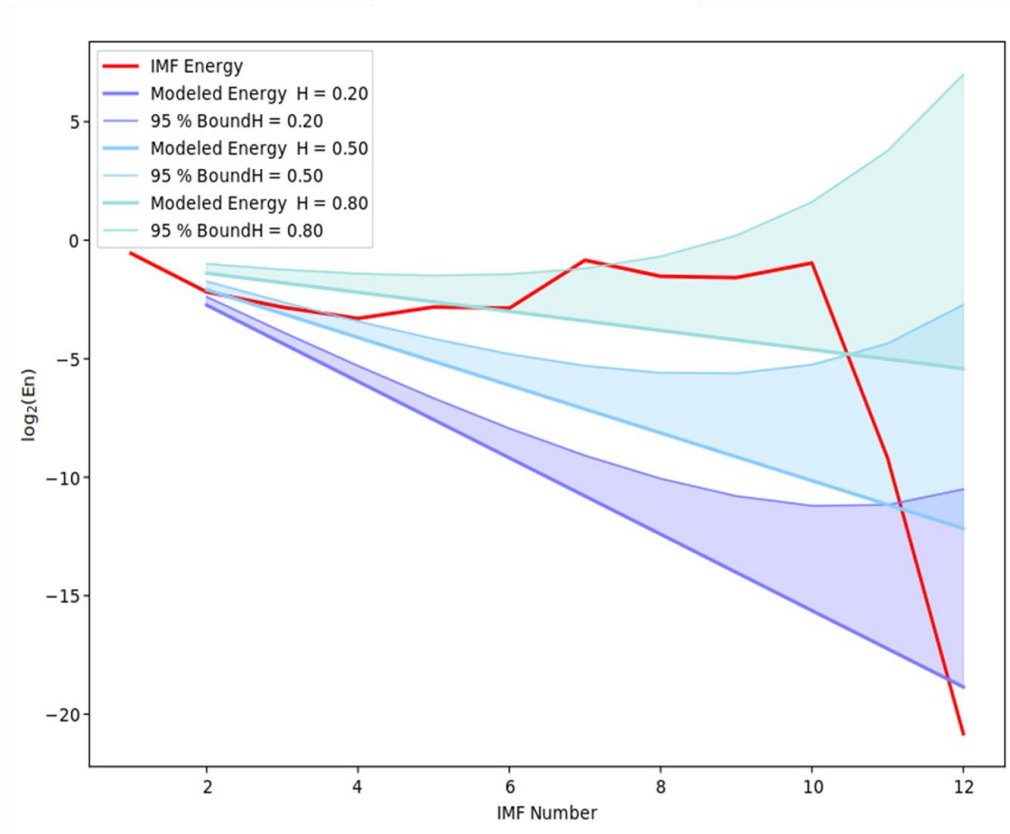


Figure 5.21. The logarithm of the estimated EEMD variances of the ERGN east component, as a function of the IMF index, and the confidence intervals for the three values of  $H$  (0.2, 0.5, 0.8)

The noise in the GPS time series is correlated in time. Since this correlation is mostly site specific, it is not usually possible to describe the noise in the time series with a single model or with a single combination of the models (although there are generalizations to some degree, see section 2.5). The advantage of the signal denoising using EMD stems from the adaptive nature of the algorithm. Since the method is fully data-driven, a pre-determined model about the noise is not assumed, which might be inappropriate. Here we chose  $H$  as 0.5, which corresponds to white noise, in determining the thresholds for denoising. Because choosing a higher  $H$ , might cause



suppressing also the transient signals which we are looking for, in addition to the correlated noise. To discriminate between the correlated noise and the transient signals, we rely on the coherence of the transients in space. We incorporated the Principal Component Analysis to detect this coherency.

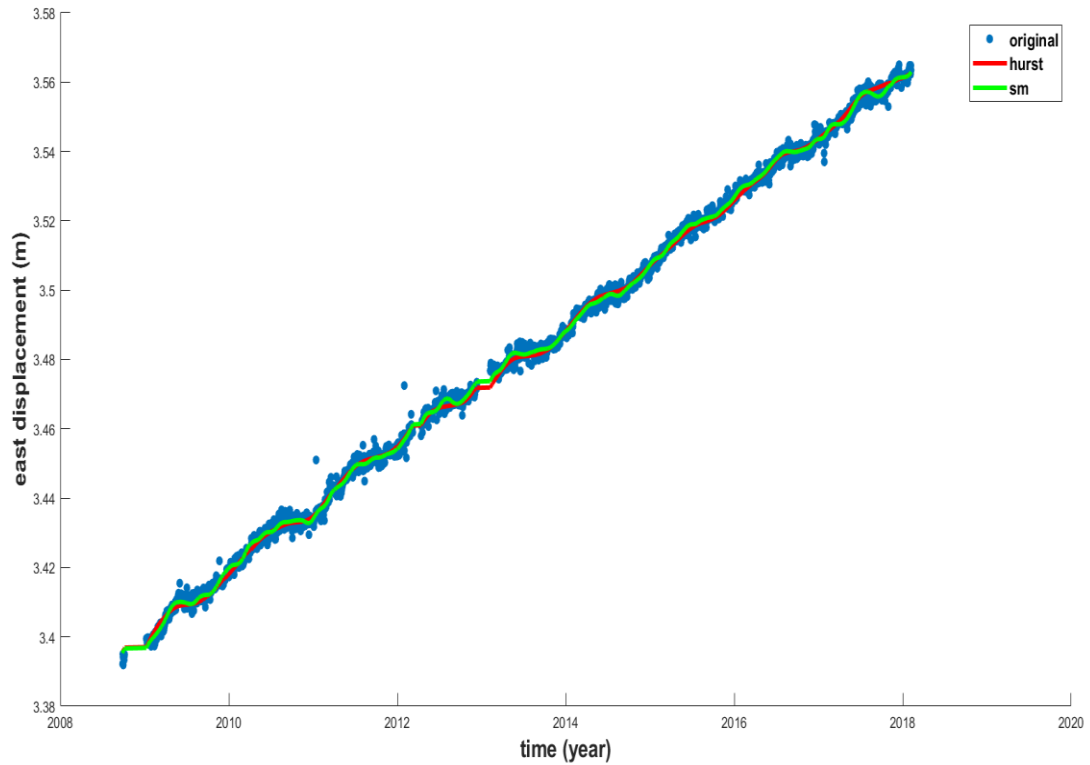


Figure 5.22. Denoising of the ERGN east time series (blue dots), by using standardized means (green line) and IMF statistics (red line).

In the final step of our transient signal detection approach, we utilized the Principal Component Analysis (PCA). We first formed a  $n$  by  $p$  data matrix  $\mathbf{X}$ . The element  $x_{ij}$  of the data matrix corresponds to the  $i$ th sample of the  $j$ th variable. Here, samples are the timely EEMD-based denoised residuals of the original coordinate time series, and the variables are the direction coordinates (i.e., north, east, up). Column vectors of the

data matrix can be composed of only north, east or up components of the stations, or a combination of the north and east components (i.e., horizontal component). A row vector is composed of the residuals measured at different sites but at the same epoch. We then normalized the data matrix by subtracting the average of each variable from the associated samples.

Later we applied classical PCA to the data matrix (see Chapter 4 for details) and obtained the  $p$  by  $p$  eigenvalue ( $\mathbf{L}$ ) and the eigenvector ( $\mathbf{A}$ ) matrices of the covariance matrix of the data matrix. The principal components ( $\mathbf{Z}$ ) are the projections of the data on the principal directions (eigenvectors), i.e.,  $\mathbf{Z} = \mathbf{XA}$ , where  $z_{ij}$  is the  $i$ th sample of the  $j$ th PC. The PCs have the units of the original variables. When we rank the eigenvectors with respect to their associated eigenvalues from highest to lowest, the principal components are in the order of significance.

To detect the transient signals, we investigated the systematic temporal patterns in the PCs, especially in the first PC. To determine the significance of the detected transient signal, we examined how much of the total data variance is explained by the associated eigenvalue (i.e., variance explanation percentage (VEP): eigenvalue of the associated component\*100/overall sum of the eigenvalues). We also calculated the rate between the variance explanation percentages of the first and second PCs ( $VEPR = VEP^1/VEP^2$ ). Lastly, we investigated the deviation of the  $\chi_{dof}^2$  values of the components from 1.0 (which corresponds to simply random noise).

We demonstrate the capability of our method in the Cascadia subduction zone, located in the Pacific Northwest first, by detecting the slow slip events. Since these events are also detectable from the actual GPS data, we primarily aimed at showing the SNR improvement of our approach. Secondly, we applied our algorithm to the Alaskan

GPS time series to detect the transient inflation at Akutan volcano. Since the transient is aseismic (that is, it cannot be associated with earthquakes), and has low SNR, it cannot be identified in the original data. Finally, we exhibit the effect of the CME reduction in the detection of the postseismic deformation after the October 23, 2011 Van earthquake.

### **5.2.1 Slow Slip Events in Cascadia**

Slow slip events (SSEs) are regular displacement episodes that occur in up to months, in contrast to the immediate co-seismic displacements due to a typical earthquake. They were first discovered through continuous GPS measurements at Nankai (Japan) and Cascadia subduction zones (Hirose et al., 1999; Dragert et al., 2001). Later it was discovered that SSEs are correlated with the non-volcanic tremors (Obara, 2002). Since then, correlated episodic tremor and SSE phenomena together have been called Episodic Tremor and Slip (ETS) (Rogers and Dragert, 2003; Obara et al., 2004). The Cascadia subduction zone is convergent plate boundary where the Explorer, Juan de Fuca and Gorda plates move to the east and slide below continental North American Plate (see Figure 5.23).

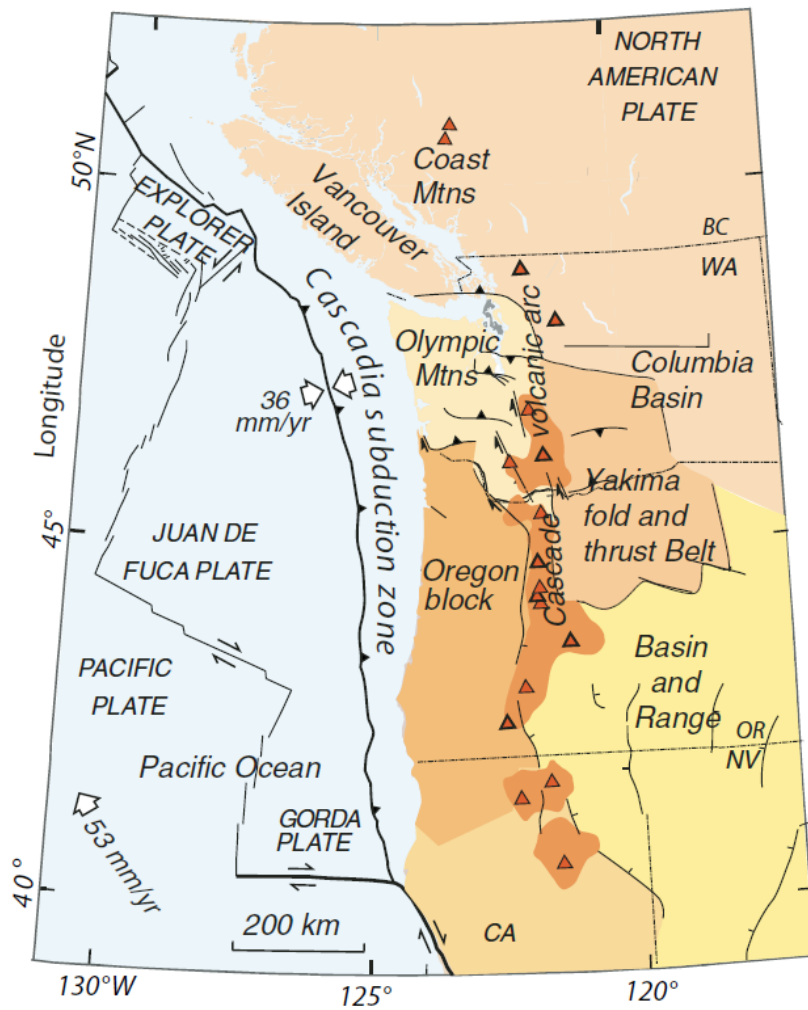


Figure 5.23. Tectonic map of Cascadia. Triangles denote volcanoes (Figure from Gomberg, 2010, which is modified from Wells and Simpson, 2001).

Today, there is an extensive collection of studies about the SSEs in Cascadia (e.g., Schmidt and Gao, 2010; Dragert and Wang, 2011; Bartlow et al., 2011; Schmalzle et al., 2014; Haines et al., 2019). The SSEs at the Cascadia subduction zone recur every 10-19 months (Brudzinski and Allen, 2007; Szeliga et al., 2008). The recurrence and the correlation with the tremor activity are illustrated in Figure 5.24.

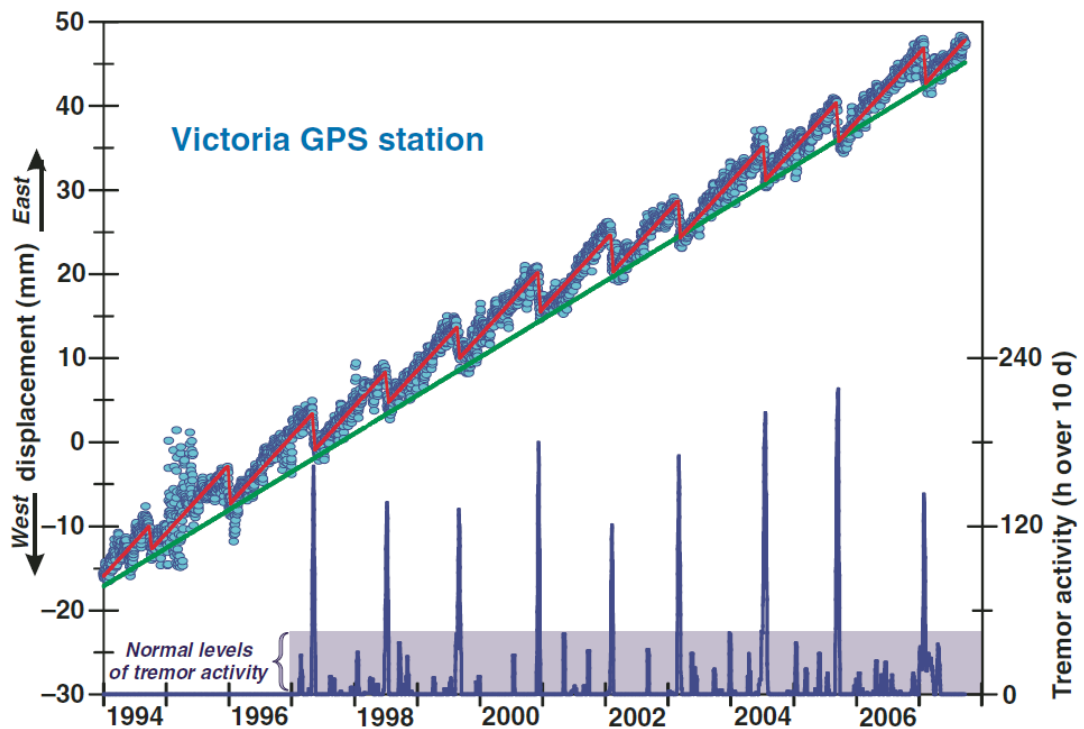


Figure 5.24. The east motion (relative to stable North America) of the Victoria (British Columbia) station in a sawtooth fashion, and the tremor activity (Figure from Gomberg, 2010, which is updated from Rogers and Dragert, 2003).

The previously detected slow slips and episodic tremors between 2007 and 2009 are displayed in Figure 5.25. To apply our detection method, we have downloaded the available daily GPS position data at 10 stations (ALBH, NEAH, SC02, SEDR, P436, P438, SEAT, KTBW, PCOL, TWHL) of Plate Boundary Observatory (PBO) network located in the Washington State section of the Cascadia zone from the PBO archives (<https://www.unavco.org/data/gps-gnss/gps-gnss.html>). These stations experienced both 2007 and 2008 SSEs during approximately the same time periods (i.e., SSE signals were not propagated).

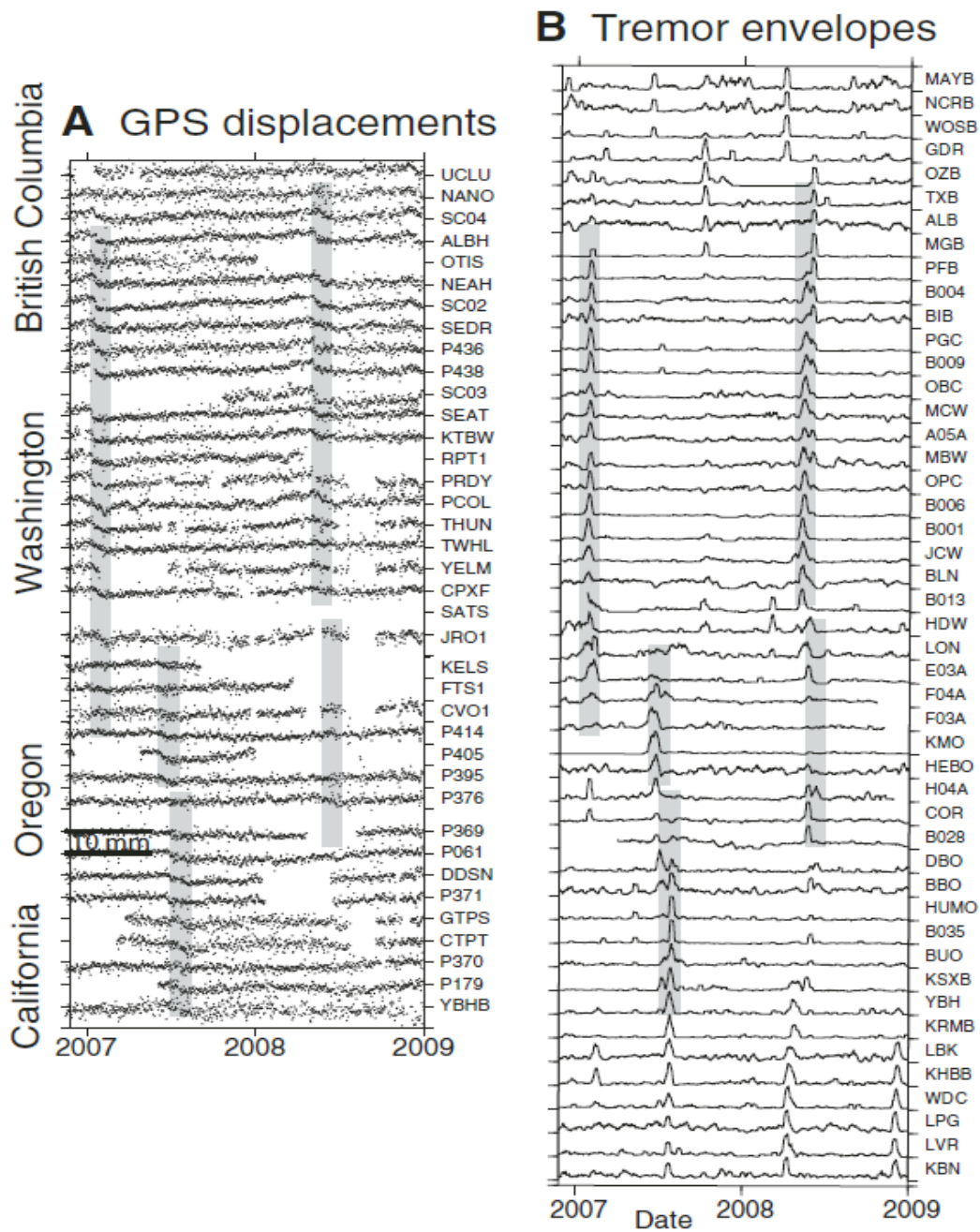


Figure 5.25. The 2007 and 2008 ETS events (gray vertical lines) observed in the (a) east motions of the GPS sites, (b) seismic-wave amplitudes (Figure from Gomberg, 2010).

The locations of the selected sites are displayed in Figure 5.26. Considering the data gaps, we used the displacement data in the east direction between November 01, 2006 and January 01, 2009. We interpolated the missing values by using piecewise cubic hermite interpolating polynomial. Later, we detrended the data by accounting for the secular rates and seasonal components.

We present the stacked residuals in Figure 5.27. The time locations of the SSEs are highlighted with vertical red blocks. The maximum displacements are about 7 mm.

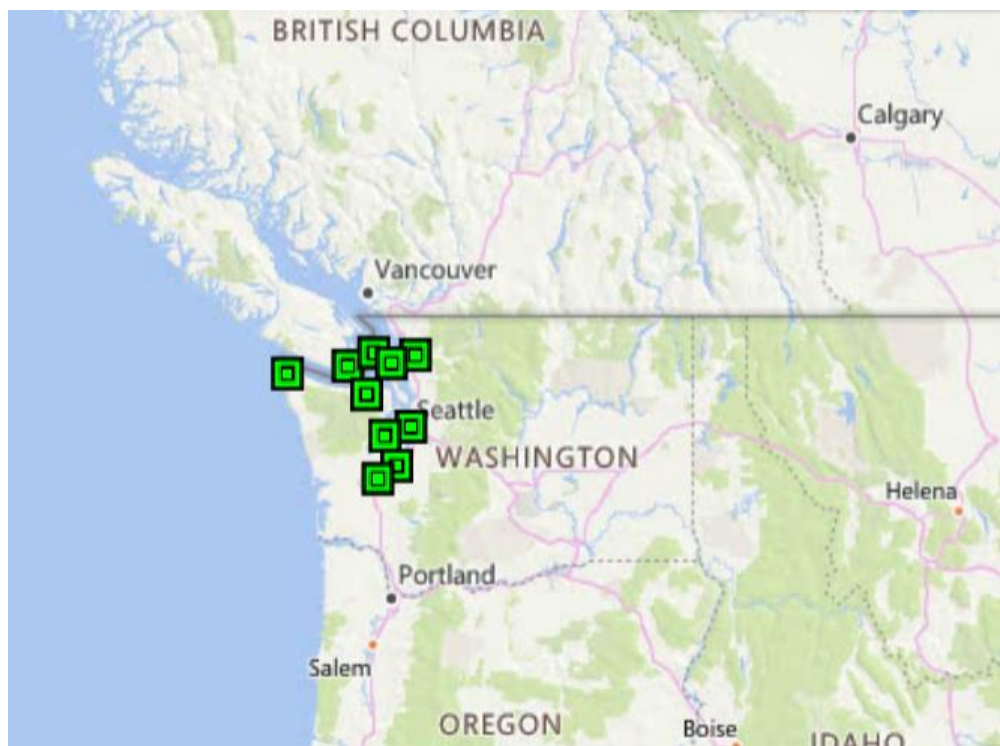


Figure 5.26. The locations (green squares) of the selected sites for transient signal detection (<https://www.unavco.org/data/gps-gnss/data-access-methods/dai2/app/dai2.html#grouping=PBO;scope=Station;sampleRate=normal;groupingMethod=contains>).

Next, to reduce CME (if present), we applied the stacking/filtering approach explained in Section 5.1.8 to the residuals. The resulting time series are displayed in Figure 5.28. Later, without attempting to reduce CME by filtering, we improved the SNR of the residual time series by suppressing the white noise using Ensemble Empirical Mode Decomposition. The white noise reduced time series are presented in Figure 5.29.

To be able to show the improvements brought by our method and to make comparison, we first applied PCA directly to the detrended, and to the filtered residuals shown in Figure 5.27 and Figure 5.28, respectively.

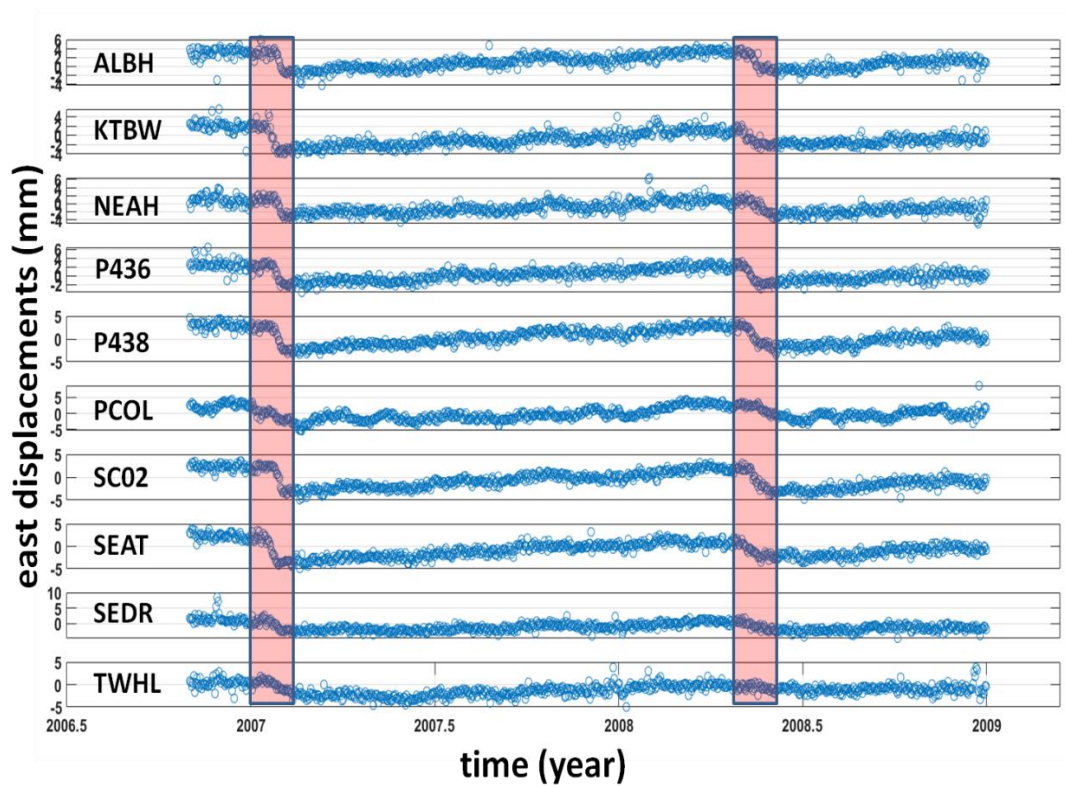


Figure 5.27. The detrended GPS time series used in the transient signal detection. The time locations of the SSEs are highlighted with vertical red blocks.



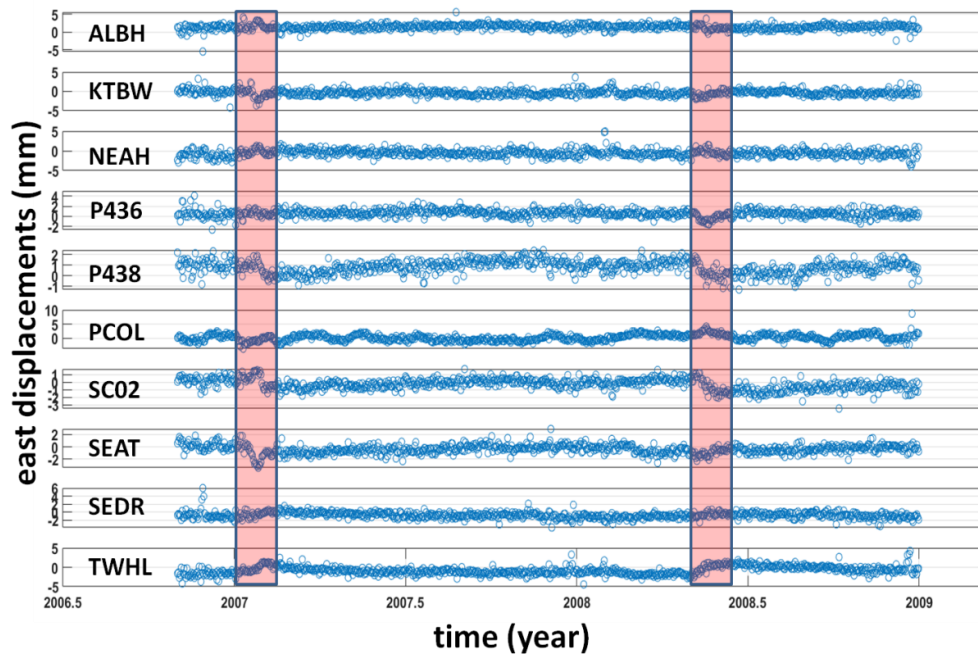


Figure 5.28. The filtered GPS time series used in the transient signal detection. The time locations of the SSEs are highlighted with vertical red blocks.

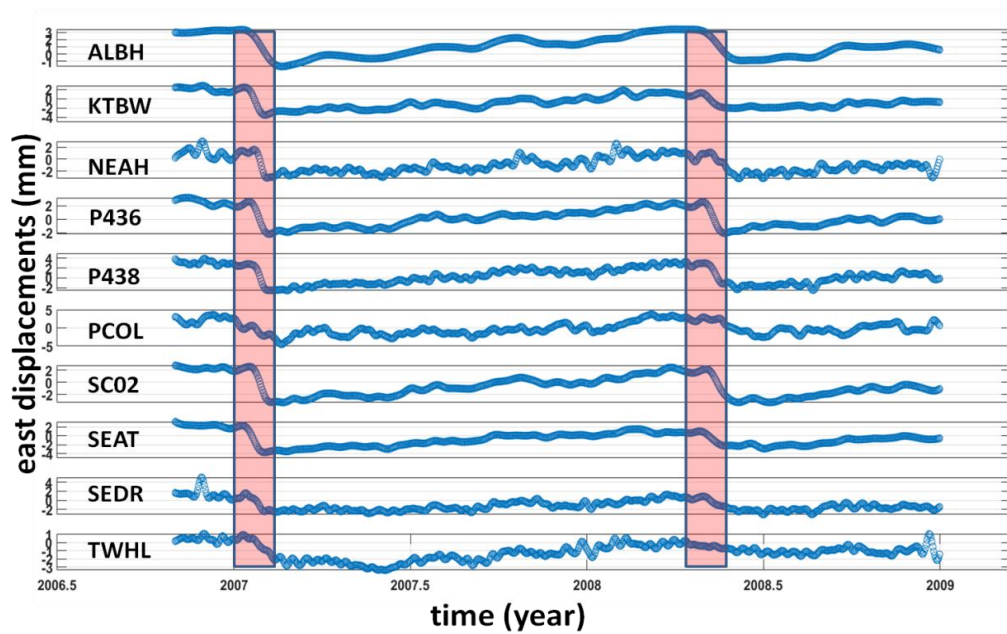


Figure 5.29. The SNR-improved GPS time series used in the transient signal detection. The time locations of the SSEs are highlighted with vertical red blocks.

In the last step we applied PCA to the residual time series whose SNR values were improved by suppressing the white noise using the EEMD. The obtained first PCs through the analyses of all three sets of time series are plotted in Figure 5.30. As mentioned in section 5.1.8, the stacking/filtering approach for the purpose of common mode correction is risky in transient signal detection studies. Since the average of the residuals are subtracted from the individual positions, the common signals like SSEs (especially when the number of the time series is small and the SSEs are present in the majority of the time series) might also be removed as common mode errors. This is clearly seen in both the filtered time series (see Figure 5.28) and PCA results (see Figure 5.30).

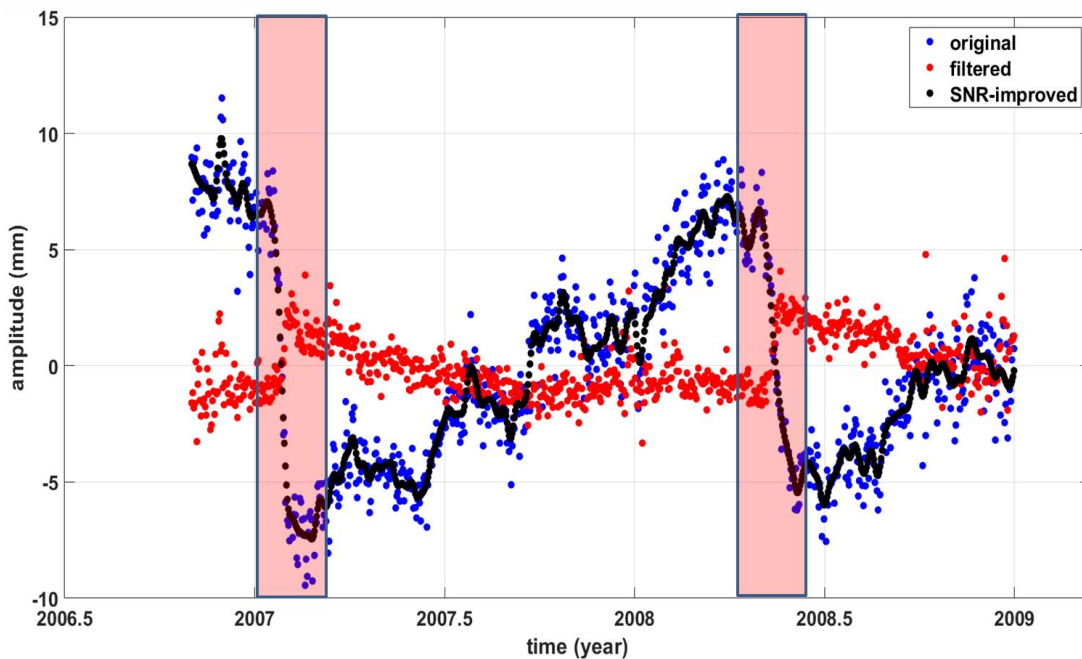


Figure 5.30. The first PCs from the PCA applied to the original detrended time series, regional filtered residuals, and SNR-improved residuals (blue, red, and black dots, respectively). The time locations of the SSEs are highlighted with vertical red blocks.

Since the SSEs here are even detectable in the raw time series, their temporal patterns are also obvious in the first PC (from the PCA of the original residual time series) at the beginning of 2007 and through the mid-2008 (emphasized by red vertical columns). First PCs are the only PCs having systematic temporal patterns. Thus, other PCs are not presented here.

We demonstrate the refinements in the PCA results after the implementation of our method by illustrating the variance explanation percentages (VEPs) in a scree plot. In Figure 5.31, the first seven out of ten VEPs (77.45%, 5.46%, 4.03%, 3.06%, 2.45%, 2.29%, 1.70%, 1.51%, 1.18%, 0.78%) of the PCs obtained from the raw time series are displayed. The figure shows only the first seven PCs since they explain 95% of the total variance. The only clear break is between the first and the second PCs ( $VEPR = \frac{VEP^1}{VEP^2} = 13.97$ ). However, it might be hard to explain the variation in the data only with the first PC when its VEP is not sufficiently high. This is what happened when we filtered the time series before PCA. In Figure 5.32, we display the scree plot of the PC VEPs (24.25%, 22.08%, 12.44%, 10.19%, 9.32%, 6.99%, 6.11%, 5.48%, 3.15%, 0.01%) obtained from the filtered data. Eight of the ten PCs are needed to explain the 95% of the variation. First PC has a VEP of 24.25%, and the  $VEPR$  is only 1.10. There is not any clear break between the PCs.

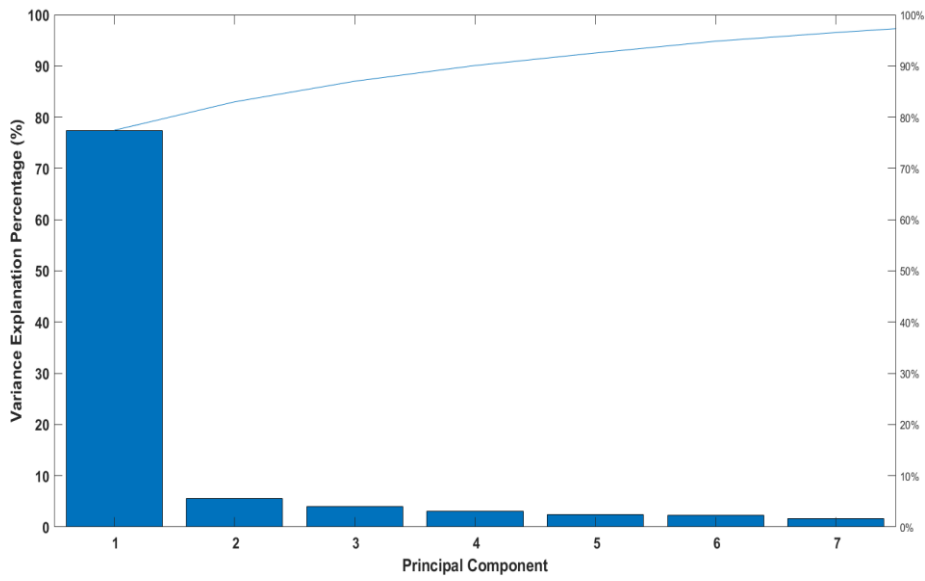


Figure 5.31. The percent variability explained by the PCs obtained from the original detrended time series (see the explanation in the text). The blue curve is the cumulative sum curve of the VEPs.

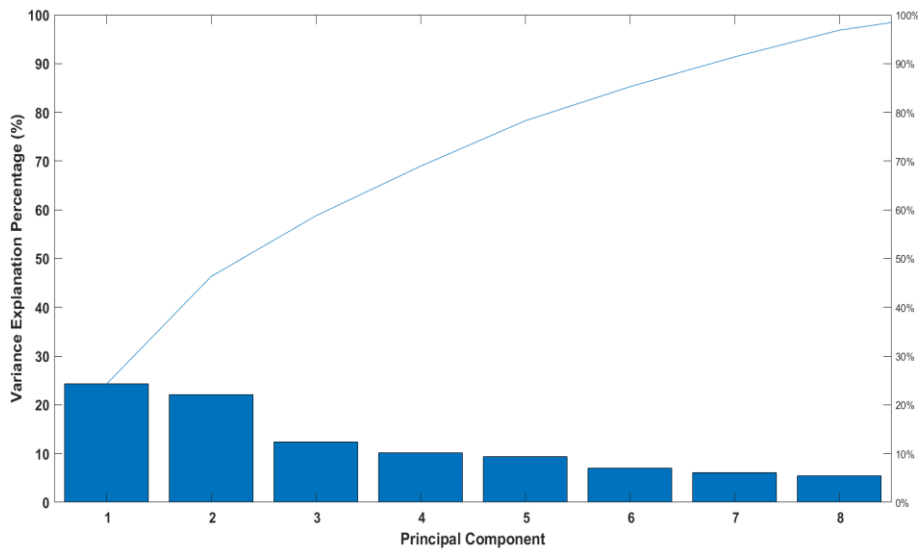


Figure 5.32. The percent variability explained by the PCs obtained from the filtered time series (see the explanation in the text). The blue curve is the cumulative sum curve of the VEPs.

On the other hand, the PC VEPs (87.52%, 5.12%, 2.33%, 1.82%, 1.03%, 0.83%, 0.52%, 0.36%, 0.27%, 0.20%) of the denoised residual time series exhibit the significant increase in the first PC VEP (from 77.45% to 87.52%), and hence the extended capability of detecting the spatially coherent transient signals. The break between the first and the second PC is more distinct ( $VEPR = 17.09$ , increased 22.33% in comparison to the raw series). Furthermore, only the first four PCs are capable of explaining the 95% of the total variability.

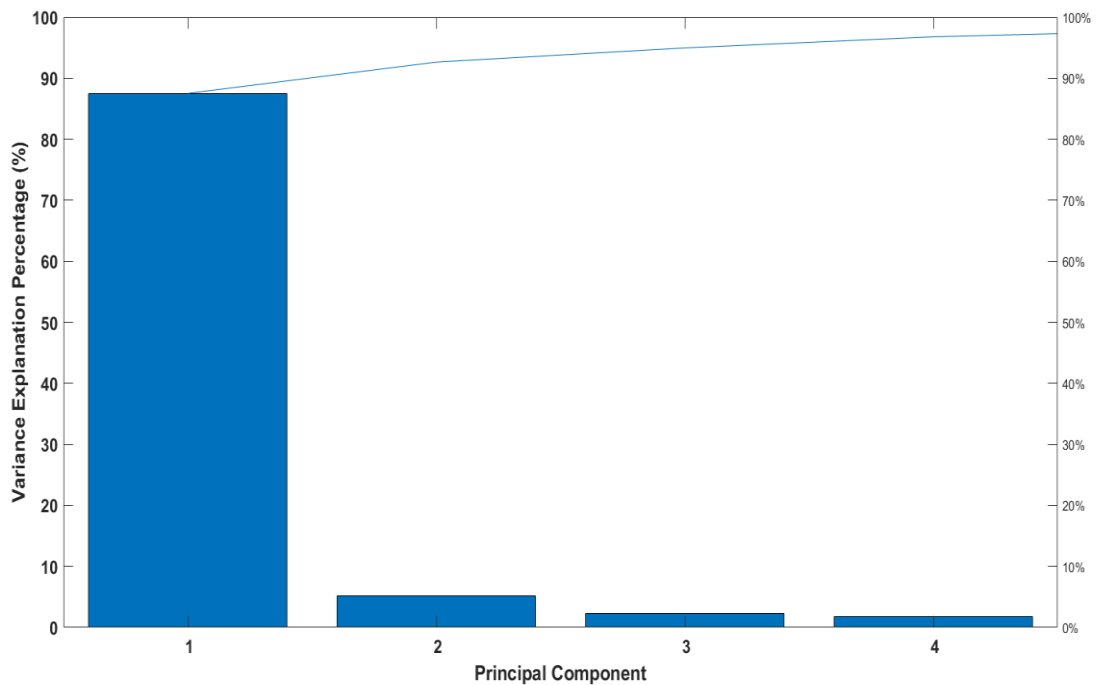


Figure 5.33. The percent variability explained by the PCs obtained from the SNR-improved residual time series (see the explanation in the text). The blue curve is the cumulative sum curve of the VEPs.

### 5.2.2 Transient inflation at Akutan Volcano

We now demonstrate the capability of our method by attempting to detect a more subtle transient signal which cannot be easily identified in the raw time series, due to its aseismic nature, low SNR, spatially and temporally correlated noise, and large number of sites in the network.

The Aleutian Arc in the Alaska state of the United States is a large volcanic arc formed due to the subduction of the Pacific Plate beneath the North American Plate (see Figure 5.23). One of the most active volcanoes in the arc is Akutan Volcano which also frequently produces low-level eruptive activity (localized steam and ash emissions), with the latest being in 1992 (Miller et al., 1998). Small inflation events at the volcano in 2008 (Ji and Herring, 2011; Li et al., 2016), in 2011 (Walwer et al., 2016; Ji et al., 2017), in 2014 and 2016 (Ji et al., 2017) were discovered using the continuous GPS data. These events might be due to the magma accumulation in a shallow reservoir. We aimed at detecting the transient signal occurred during 2008. Ji and Herring (2011) used a Mogi point source (Mogi, 1958) to model the displacements (transients) they detected in the GPS time series by using Kalman filtering and PCA, and estimated the location of the Mogi source as being at a shallow depth (~3.9 km below sea level) near the volcano summit.

We have downloaded the daily GPS data in Stable North America Reference Frame (SNARF) of 151 Alaska sites between 130°W-175°W and 50°N-75°N from <https://www.unavco.org/data/gps-gnss/gps-gnss.html>. Since the wavelength of the CME is longer than the size of Alaska and may hide the 2008 inflation (Ji and Herring, 2011), we aligned the data to a regional reference frame to diminish the spatially correlated noise. In the reference frame definition, we used the sites whose horizontal and vertical velocity uncertainties are below 0.45 mm/yr and 0.9 mm/yr, respectively.

Later, we removed the linear rates and periodic terms from the time series. For uniform site distribution as much as possible, and for more samples in time, the 3-year time interval between 2007 and 2010 was selected. The sites used in the transient signal detection exercise are displayed in Figure 5.34. We applied PCA first directly to the downloaded raw (but detrended) time series. Afterwards, we applied PCA to the CME-suppressed and SNR-improved time series. The comparison of the results over VEPs is illustrated in Figure 5.35. The VEP of the first PC increased from 17.95% to 30.80%, and *VEPR* increased from 1.87 to 3.28. Further, the first 10 PCs of the CME-suppressed and SNR-improved time series can explain 75.46% of the variability, while the first 10 PCs of the raw time series can explain 60.95% of the total variance,

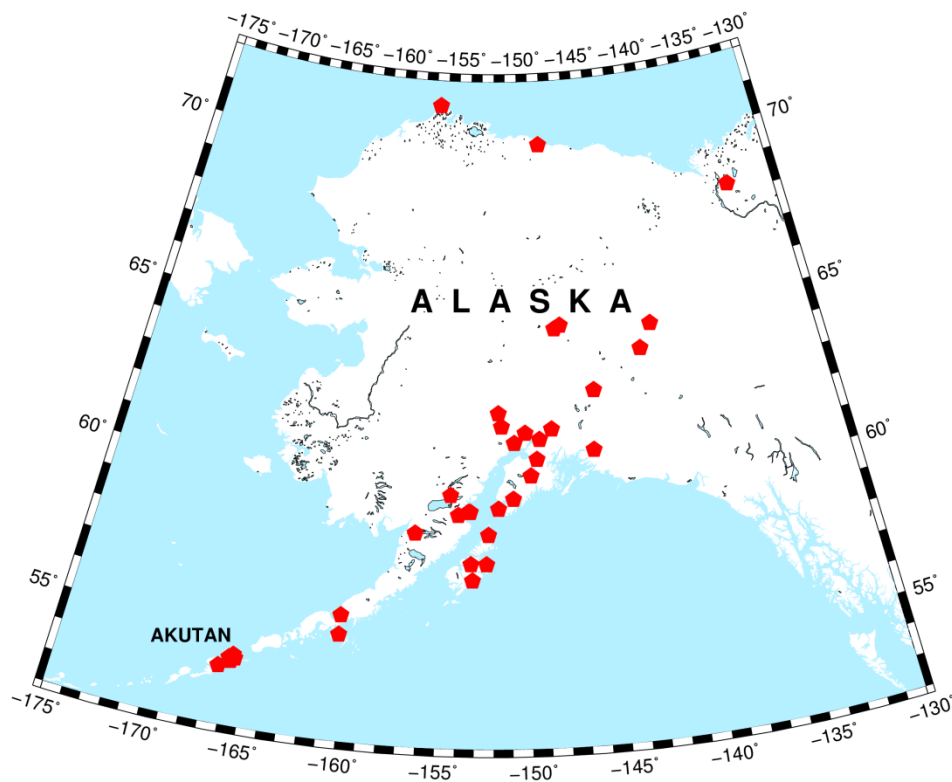


Figure 5.34. The Alaska sites (red pentagons) used in the transient signal detection exercise.

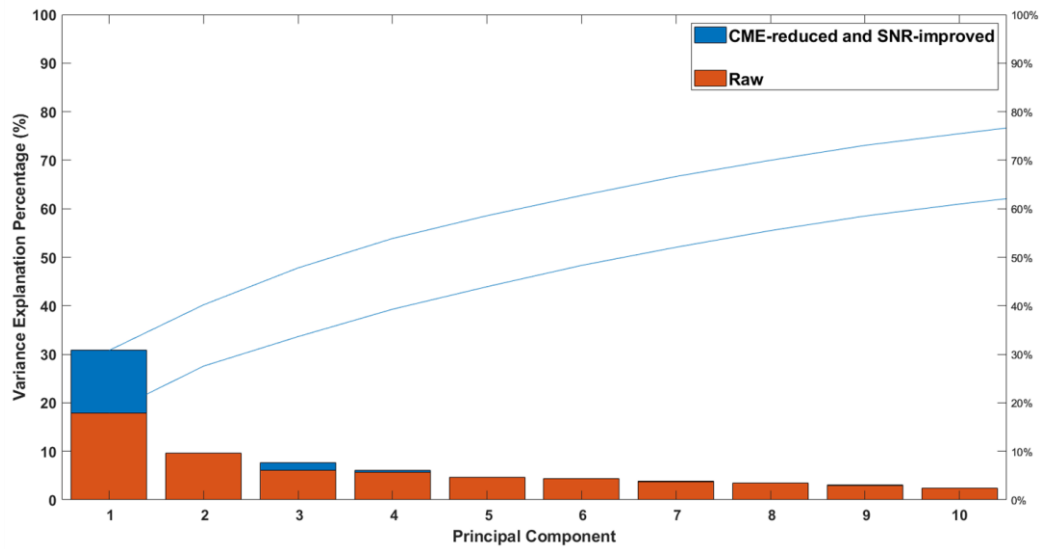


Figure 5.35. The percent variability explained by the PCs obtained from the raw (red) and CME-suppressed-SNR-improved time series (blue). The blue curves are the cumulative sum curves of the VEPs.

The resulting first PC obtained by using our method is displayed in Figure 5.36. It reveals a transient event during the first half of 2008.

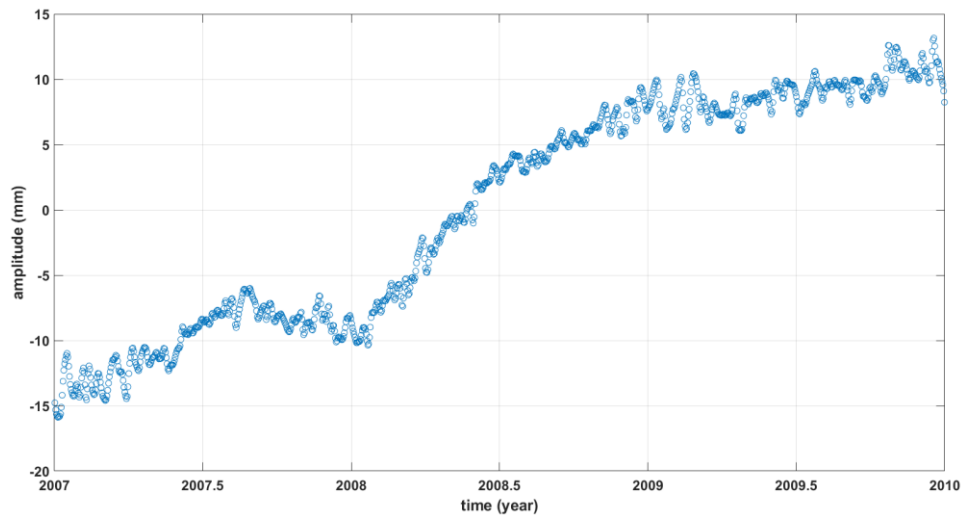


Figure 5.36. The first principal component of the CME-reduced-SNR-improved time series.



We then isolated the detected signal by including in the PCA only the sites located in the Akutan Island (see Figure 5.37), and the time interval (October 01, 2007 – October 01, 2008) experiencing the transient signal.

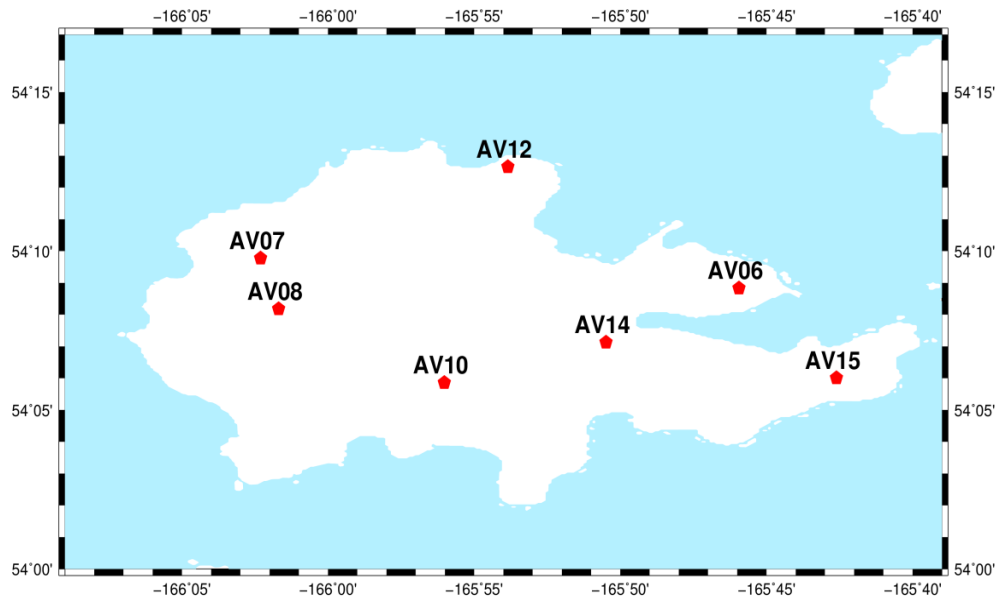


Figure 5.37. The 7 sites on the Akutan Island used in the analysis.

Figure 5.38 shows the first and the second horizontal PCs of the CME-suppressed and SNR-improved time series of the 7 sites located in the Akutan Island. The first PC is the only PC having a systematic temporal pattern among all PCs.

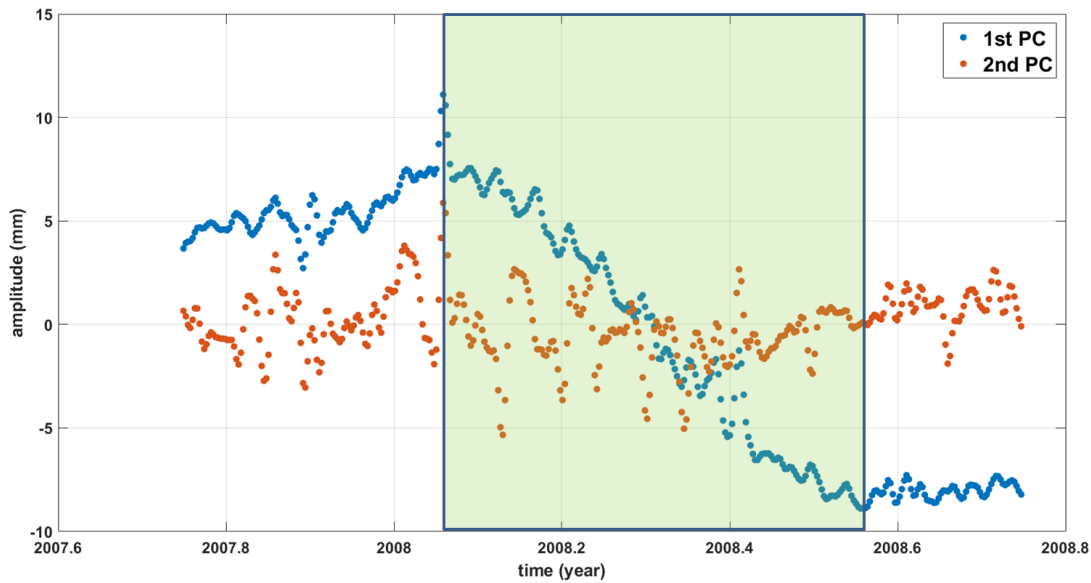


Figure 5.38. The first (blue) and second horizontal (red) PCs of the CME-suppressed and SNR-improved time series of the 7 sites located in the Akutan Island. The period experienced the transient signal is highlighted with a green column.

We present the VEPs of the resulting PCs in Figure 5.39. Compared to the Figure 5.35, increase in the VEP of the first PC is substantial (from 30.80% to 83.05%). The break between the first and the second PCs is distinct ( $VEPR$  is 14.67). The first 5 PCs (out of 14 PCs) explain the 96.54% of the total variance.

The transient signal we detected cannot be easily identified in the raw GPS position time series. Its maximum horizontal displacement is  $\sim 9$  mm (Ji and Herring, 2011). It is an aseismic signal since it is not associated with the seismicity. Ji and Herring (2011) detected the same transient signal by using exactly the same set of 7 stations in the Akutan Island. Their approach is to apply Kalman filtering to improve the SNR in the time domain before PCA. They could obtain a VEP of 64.5% for the first PC.

Therefore, we think that our method, by applying the data-adaptive Ensemble Empirical Mode Decomposition in denoising the time series, suppresses the noise more successfully and produces superior results.

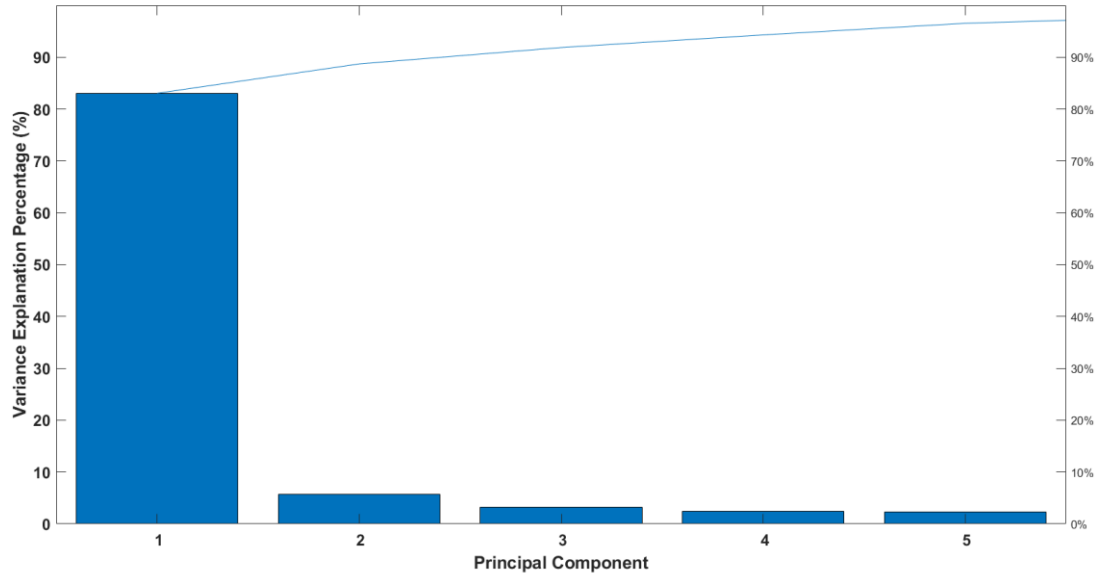


Figure 5.39. The percent variability explained by the horizontal PCs of the 7 Akutan sites, after the implementation of our method. The blue curve is the cumulative sum curve of the VEPs.

### 5.2.3 Postseismic deformation following the October 23, 2011 Van earthquake

The earthquake happened in eastern Turkey (north of the city of Van, the eastern edge of Lake Van) on October 23, 2011 is the largest earthquake ( $M_w$  7.1 - United States Geological Survey (USGS) earth catalogue) occurred in Turkey, since the establishment of the CORS-TR Network. Continuous GPS data are used in the earthquake studies to investigate the interseismic, coseismic and postseismic motions (see e.g., Tiryakioğlu et al., 2017) of the geodetic points, in addition to the

interferometric synthetic aperture radar (InSAR), seismology and satellite imagery which are utilized in constraining the fault parameters (e.g., Elliot et al., 2013). Determination and modeling of these motions are needed to obtain precise and reliable velocity fields which are the basis of the strain analyses.

Ozdemir and Karşlıoğlu (2019) reported 13 CORS-TR stations (AGRD, BASK, CATK, HAKK, HORS, IGIR, KRS1, MURA, OZAL, SEMD, SIRN, TVAN and VAAN) that have experienced coseismic displacements following the Van earthquake. How far a point on the surface from the earthquake epicenter which experiences displacement and following deformation depends on many parameters, such as earthquake magnitude, fault type and fault geometry.

Often, closer sites to the epicenter are exposed to larger displacements, and the size of the displacement decreases as the distance between the site and the epicenter increases. Thus, coseismic and postseismic motions can be easily identified in the long-term continuous GPS time series of the stations located closer to the epicenter, even through a simple visual inspection (see Figure 5.40). However, the farther the distance between the site and the epicenter becomes, the more advanced techniques are needed to detect the existence and the level of the deformation.

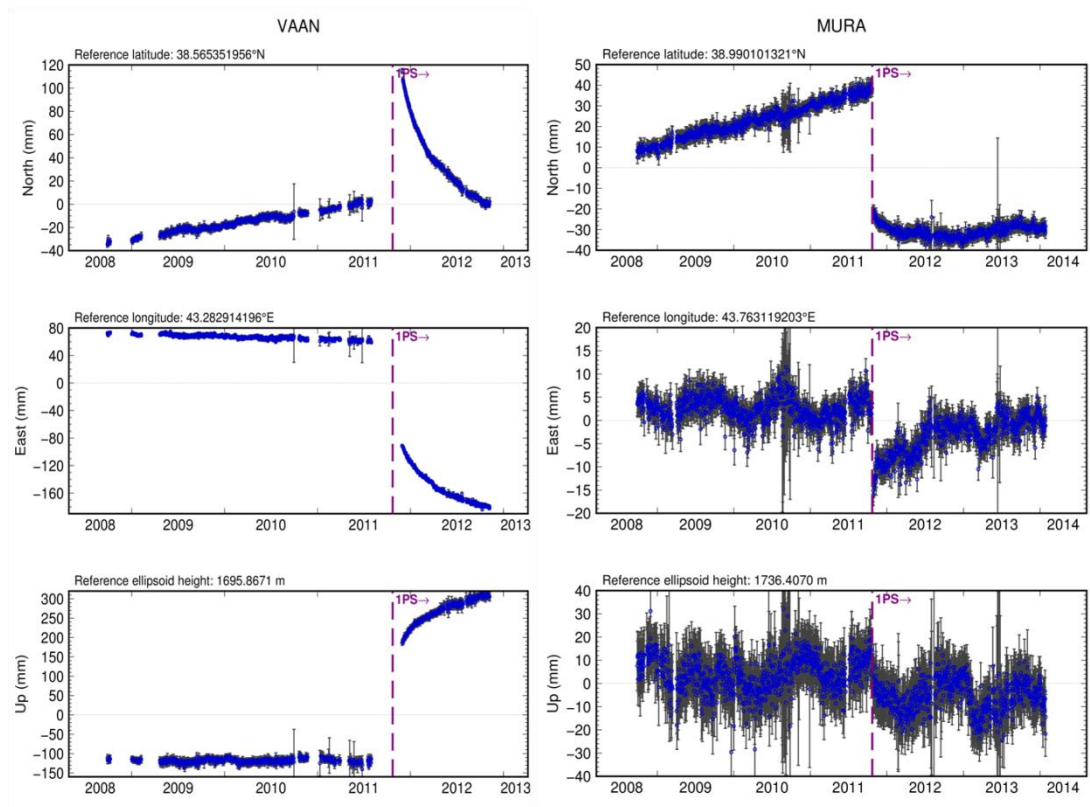


Figure 5.40. The coseismic and postseismic motions of VAAN (left) and MURA (right) in a Eurasia-fixed system due to the Van earthquake (purple vertical line).

Since we are looking for coherent transient signals in space, it is important to see such signals in multiple sites. However, considering the average inter-station distance between the CORS-TR sites which is about 70 km, it is not easy to detect a transient signal whose geographic extent is small. Therefore, we demonstrate the capability of our method on the detection of the postseismic deformation subjected to multiple sites following the destructive Van earthquake.

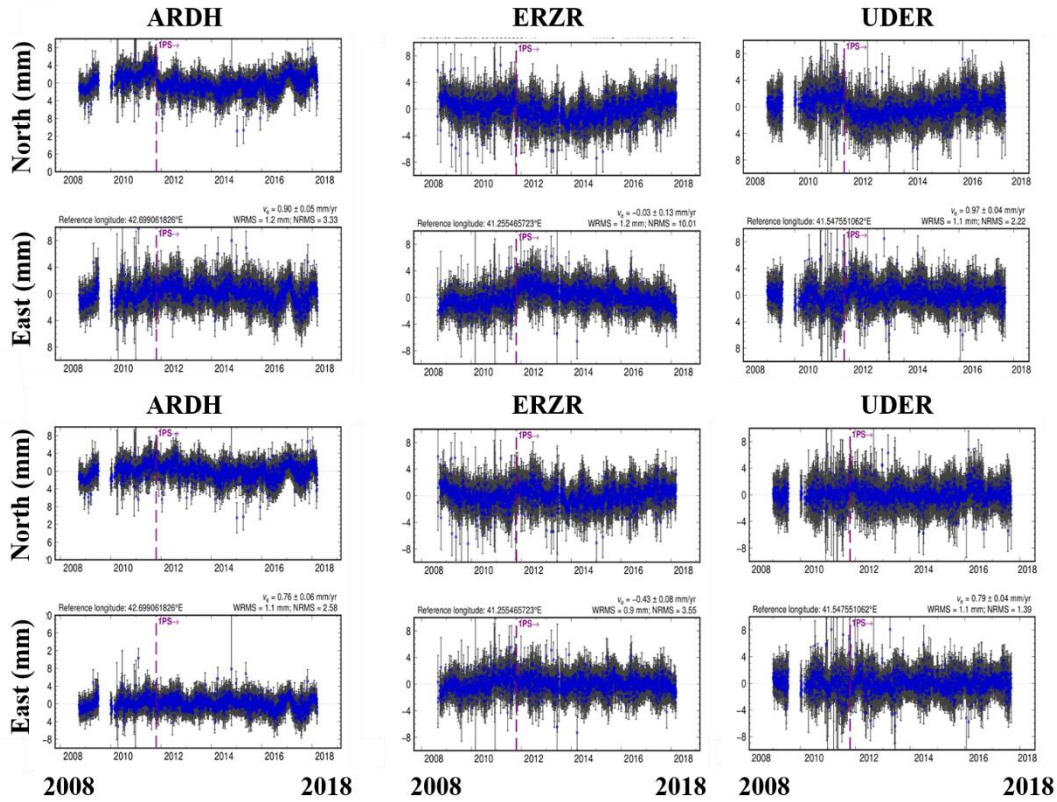


Figure 5.41. The horizontal residual time series of ARDH (left), ERZR (middle) and UDER (right) stations before (top) and after (bottom) the coseismic correction. The dashed purple vertical lines indicates the time of the Van earthquake.

We used the time series in the regional frame (i.e., CME-reduced time series) transformed from the Eurasia-fixed system (see the procedure explained in the section 5.1.8). In addition to the 13 stations reported in Ozdemir and Karshoğlu (2019), we detected very low-size coseismic displacements ( $\leq 5$  mm) in the residual time series of ARDH, ERZR and UDER stations, which cannot be seen in the raw position time series. However, we could not detect any postseismic deformation visually at these sites, after removing the coseismic displacements. The horizontal residual time series of these stations before and after the coseismic correction are displayed in Figure 5.41.

In order not to bias the results due to large deformations observed at close stations to the earthquake epicenter, we did not include the closest VAAN, OZAL and MURA stations in our exercises. We used the 13 stations exposed to coseismic displacements and presented in Figure 5.42 in our transient signal detection analysis. We did not include MALZ station due to its high repeatabilities (North: 9.8 mm, East: 13.1 mm). To isolate the signal in time, we selected the time interval between August 01, 2011 and June 29, 2012. We interpolated the missing values by using piecewise cubic hermite interpolating polynomial.

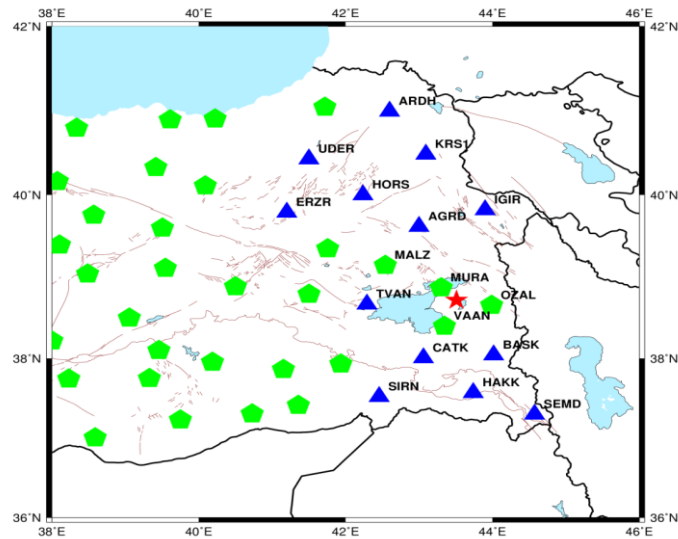


Figure 5.42. CORS-TR stations used in the transient signal detection exercise (blue triangles), other CORS-TR stations (green pentagons) and the epicenter of the Van earthquake (red star).

We illustrate in Figure 5.43 the first and the second PCs obtained from the PCA applied to the raw residual time series, and the first PC obtained from the PCA applied to the CME-reduced-SNR-improved time series. It is seen that the first PC from the raw series shows approximately random behavior. However the first PC from the

CME-reduced-SNR-improved series has a systematically increasing temporal pattern which might be associated with the postseismic deformation.

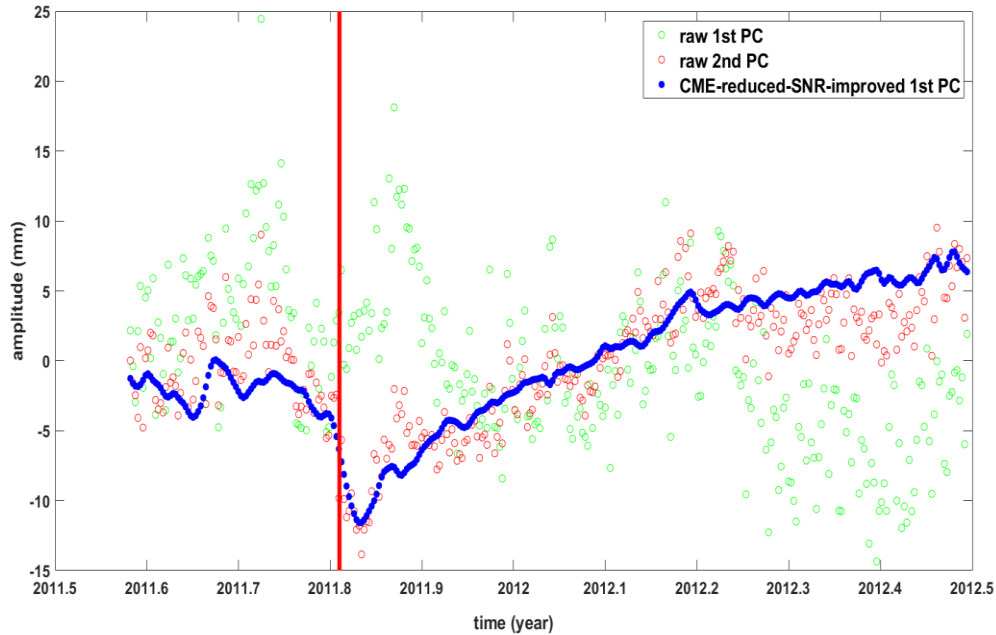


Figure 5.43. The first (green circles) and the second (red circles) PCs obtained from the PCA applied to the raw residual time series, and the first (blue filled circles) PC obtained from the PCA applied to the CME-reduced-SNR-improved time series. Red vertical line indicates the time of the Van earthquake.

Figure 5.44 displays the VEPs of the resulting PCs from both PCA. After applying our method, the VEP of the first PC increased from 34.10% to 58.13%. The break between the first and the second PCs is more distinct ( $VEPR$  increased from 1.68 to 3.38). The first 9 PCs (out of 26 PCs) from our method explain the 95.50% of the total variance. The explanation percentage of the first 9 PCs from the raw time series is 83.04%.



It should be noted that the size and the duration of the postseismic deformation are not the same for all 13 sites included in the analysis. It is likely that the closer sites to the epicenter experience more severe and longer deformations. It is demonstrated, e.g., in Figure 5.41 that the distant ARDH, UDER and ERZR stations reveal negligible deformation (possibly below current GPS resolution), and thus they might add simply random noise, instead of information, to the obtained PCs. Analyzing only the closer 4 stations to the epicenter (BASK, CATK, TVAN, AGRD) with our method produces a first PC which explains the 75.12% of the data variability.

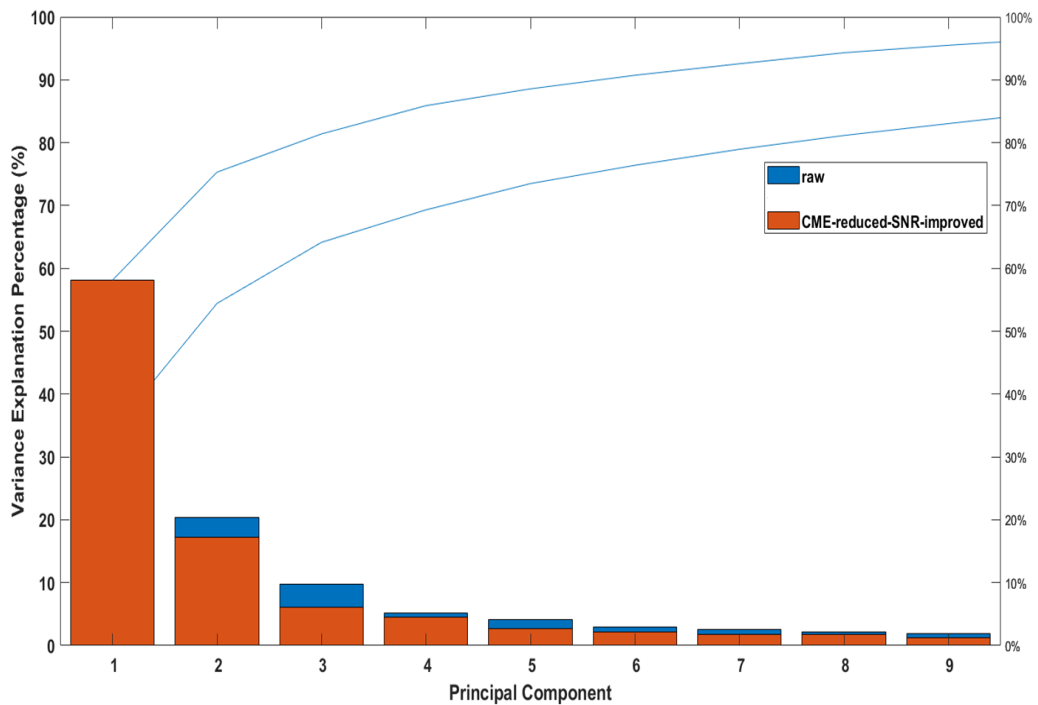


Figure 5.44. The VEPs of the resulting PCs from PCA of both the raw time series (blue) and the CME-reduced-SNR-improved time series (red). The blue curve is the cumulative sum curve of the VEPs.

Figure 5.43 proves the existence of CME in the CORS-TR time series. The largest PC of the raw residual time series (VEP: 34.10%,  $\chi^2_{dof} = 34.51$ ) shows the CME whose

temporal pattern is not only non-systematic but also non-random. The spatial pattern of the first PC is displayed in Figure 5.45 which looks relatively uniform over the stations.

It is not possible to detect the transient signal in the first PC. To suppress CME, the first PC can be ignored, and the second PC might be examined. Although it explains only the 20.32% of the total variance, the second PC could catch the transient signal by showing a systematic increase after the earthquake. In addition, its  $\chi^2_{dof}$  value of 20.56 is significantly inconsistent with the simply random noise ( $\chi^2_{dof} = 1.0$ ). But the temporal pattern of the second PC is still noisy, which might be related to the contamination by the first PC due to the orthogonality in PCA.

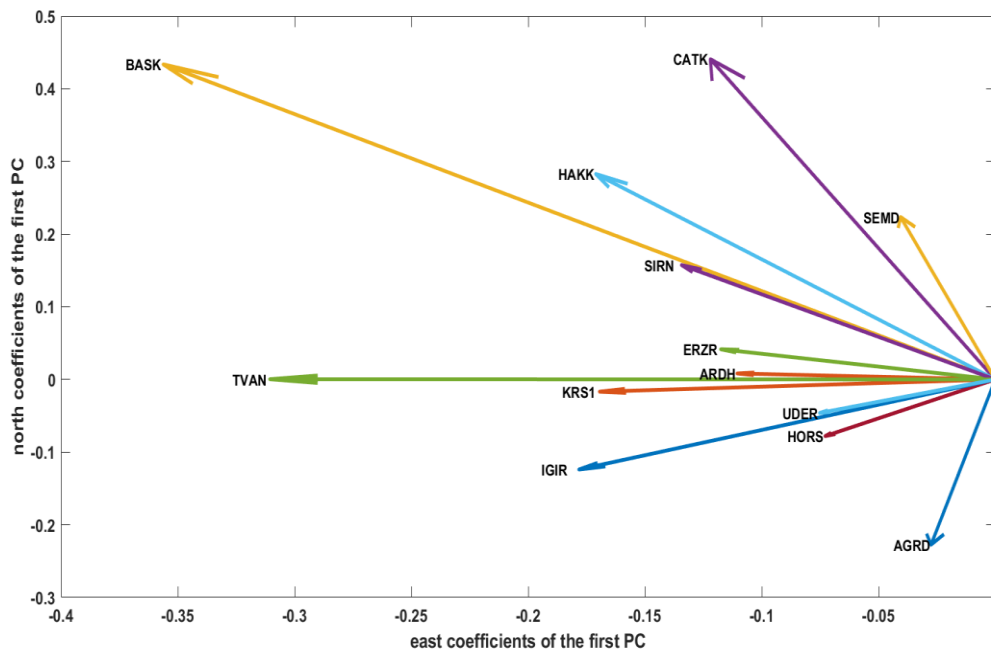


Figure 5.45. The spatial pattern of the first PC of the raw residual time series which looks relatively uniform over the stations.

On the other hand, aligning the data to a regional reference frame has successfully reduced the spatially correlated noise. We present the spatial pattern of the first PC which was obtained after applying PCA to the CME-corrected and SNR-improved (with Ensemble Empirical Mode Decomposition) time series in Figure 5.46. The spatial pattern of the first PC looks non-uniform. Both first PCs have large coefficients (loadings) at the sites closer to the earthquake epicenter (see Figure 5.42).

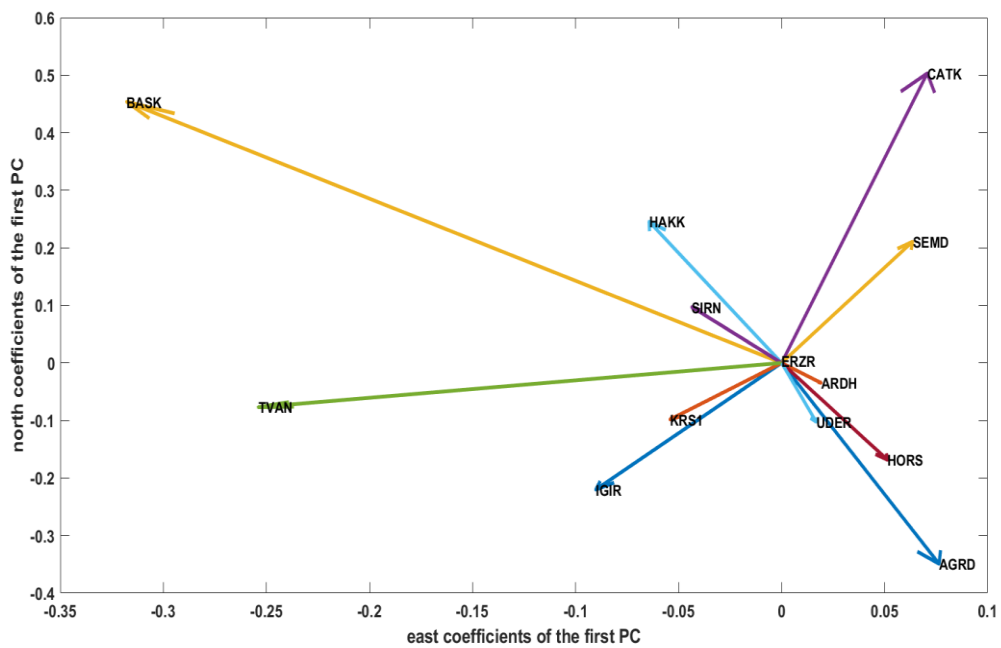


Figure 5.46. The spatial pattern of the first PC which was obtained after applying PCA to the CME-corrected and SNR-improved (with Ensemble Empirical Mode Decomposition) time series.



## CHAPTER 6

### DISCUSSION, CONCLUSIONS AND FUTURE WORK

#### 6.1 Discussion

The main goal of the CORS-TR system is to provide RTK corrections to make users achieve positioning within the tolerance of couple centimeters. Although the stations were installed on the large and low-rise buildings where possible, to reduce the oscillation effects of the building, the priority in site selection was given to several other design parameters such as, homogeneity, being in urban areas (to increase the population coverage), easy logistics, security, 7/24 power and internet supply etc. (Uzel et al., 2012). Thus, the utilization of the CORS-TR sites in tectonic monitoring necessitates very careful and precise GPS data analysis. Many sites are exposed to local effects such as ADAN, BTMN, HAKK, INEB, INE1, KNY1, MALZ, MUUS (Ozdemir, 2016; Ozdemir et al., 2017; Ozdemir and Karshoglu, 2019). Sites having high WRMS values (see Figure 5.12) must be treated with care. Such stations can dominate the Principal Components due to their large site-specific noise.

The velocity estimates of the sites with short data span (below 2.5 yrs) can be biased largely due to the annual signals (Blewitt and Lavallee, 2002). Hence, these sites should not be included in the fiducial sites list which is used in the definition of the regional reference frame, for the purpose of CME reduction.

Since the Empirical Mode Decomposition is deprived of a definite mathematical foundation, its soundness and effectiveness only could have been validated empirically. The uniqueness of the decomposition results is not guaranteed. Selected stopping criterion in the sifting process, interpolation technique used in the formation of the envelopes, method of handling boundary effects, and mode mixing might change the obtained IMFs (see section 3.3).

It is common to have missing data in the GPS time series due to, e.g., receiver malfunction and problems in power supply. In addition, anomalous daily coordinate solutions might have been deleted as outliers. Often, there is not any robust solution for predicting the missing values in non-linear/non-stationary process. However, both EMD and PCA (in our approach) require the included time series to be full and of the same length. Thus, the missing values have to be interpolated. The interpolation technique used has a gross effect on the decomposition, especially when the data gap is large. It might lead to large swings which can distort the results largely. On the other hand, the interpolated data might cause over-smoothed PCs.

The complex nature of the geophysical signals might complicate the transient signal detection. The large-scale signals may go unnoticed due to their non-localized PC patterns in comparatively small-scale networks. Such signals might not be separated from the CMEs easily. There might be overlapped or distinct multiple transient signals in the time series. The larger signals can hide the smaller signals in such cases. There might be propagating transient signals originating from the same source but incoherent in space and time, such as slow slip events observed at multiple sites at different epochs and/or during different time segments. Propagating signals can reveal themselves in multiple PCs.

It should be kept in mind that we estimate the initial trend (i.e., secular rates and seasonal signals), which is removed from the time series before applying our method, by accounting for the whole data, including the transient signals. This might decrease the detection capability of the method. For example, in the SSE detection exercise presented in section 5.2.1, estimating the SSEs by offsets and excluding them from the trend estimation, might produce sharper systematic patterns in the PCs. However, the primary goal of the transient signal detection is to detect the previously unrecognized transient signals.

EMD is a data-driven adaptive method which is more suitable than the classical methods such as Fourier Transformation, for the decomposition of the non-linear/non-stationary time series. We could apply EMD directly to the original position time series, instead of the residual time series which are obtained by removing the steady motions, for denoising purposes. However, the obtained non-linear trend (i.e., denoised signal) would have been dominated by the steady motions so strongly (e.g., the counter-clockwise rotation of the western Anatolia with respect to the fixed Eurasia reaches up to 3 cm/yr, see Figure 5.16) that it would be impossible to detect the transient signals whose magnitudes are a couple of millimeters. Our intention in initial trending is to remove the strong “known” signals which can mask the transient signals.

It should be noted that the tectonic transient signals which have been detected in this study with the developed method are the signals which have been already discovered (and associated with the source mechanisms) with different approaches in the literature. We only demonstrate here the detection capability of our method in the GPS time series. Driving forces underlying the transients must be investigated further and other supporting evidences must be searched. For example, slow slip events detected in the GPS time series are generally correlated with the seismic tremor activity.

Detection of this correlation at Alaskan sites, or relating the inflation events at Akutan Volcano to magma accumulation would give physical sense to the detected transients in the GPS time series.

## **6.2 Conclusions**

This study is about detecting transient signals in continuous GPS coordinate time series. To this end, we developed a novel method which combines the Empirical Mode Decomposition (EMD) and Principal Component Analysis (PCA). EMD improves the signal-to-noise ratio (SNR) in time by filtering out the white noise in the time series. PCA improves the SNR in space by considering the spatial coherence of the transient signals. Our main interest is the tectonically-driven transient signals. The main geographic area of interest is Turkey, where major tectonic plates meet and that is abundant of diversified deformation. Since Turkey lacks a countrywide continuous GPS network specifically designed for tectonic monitoring, we first focus on analyzing the data collected in CORS-TR network, which has been established lately to serve for cadastral studies primarily by supplying Real-Time-Kinematic (RTK) positioning, with high-precision techniques. Hereby, we investigate the convenience of the generated CORS-TR time series for tectonic studies, and prepare the data for transient signal detection. Our transient signal detection method for CORS-TR network can be summarized in general as follows:

- Processing the GPS data with high-precision techniques and generating the time series,
- Reducing the Common Mode Error (CME) by aligning the data to a regional reference frame,



- Assessing the quality of the time series and determining the appropriate sites for tectonic monitoring,
- Removing the dominant secular rates and seasonal motions from the time series,
- Suppressing the white noise in the residual time series by means of the filtering properties of the EMD method,
- Applying PCA to the selected sites and seeking for the spatial coherence of the transient signals.

We demonstrate the capability of our method in detecting the relatively weak transient signals with also applications to real data sets obtained from Plate Boundary Observatory (PBO) archives.

Turkish National Permanent GNSS Network-Active (CORS-TR), is the one and only countrywide permanent GNSS network in Turkey. The main purpose of the CORS-TR system is to provide RTK corrections to the users on the field, and hereby to ensure cm-level coordinate precision. Since the large-scale map production is officially based on the CORS-TR-derived coordinates in Turkey, it has become extremely popular, especially in the cadastral studies. As of June, 2019, there are ~11.500 users registered on the system. According to the “Large Scale Maps and Map Information Production Regulation (LSMMIPR)”, the coordinates obtained in the works related to large scale map applications have to be estimated in a national datum called Turkish National Reference Frame (TUREF). TUREF is a reference frame that coincides with the International Reference Frame 1996 (ITF96) at epoch 2005.0 (Aktuğ et al., 2011). Thus, although CORS-TR users on the field collect GPS data at the current epoch, the system provides them with the coordinates at epoch 2005.0. This is accomplished by using the velocities of the reference CORS-TR stations nearby. Hence, if the velocities

of the CORS-TR base stations are not correct or consistent with their vicinity, users will have erroneous coordinates at epoch 2005.0. Therefore, to ensure the reliability and the stability of the system, and to make the coordinate time series and velocities employable in the tectonic studies, CORS-TR data were processed with the state-of-the-art approaches, models and products. Findings and suggestions were presented and the problematic sites were reported in a national conference (Ozdemir et al., 2017). Some of these sites have been relocated, consequently.

The data collected at CORS-TR stations are processed in GDM routinely. The GPS analysis strategies evolve over time, and those adopted in GDM have never been tested and validated externally. Hence, we processed the whole CORS-TR GPS data set twice independently. Since the superiority of our approach has been proven, it has also been adopted in GDM. The daily uncertainties of the coordinates have been lowered with the new strategy. The RMS values in the reference frame definition have been decreased.

Taking into consideration the uncertainties, homogeneity and various performance criteria, a sufficient number of local stations were selected, and the solutions (time series) were expressed in a Turkey-fixed reference frame based on the coordinates of the selected stations. This way, the effect of Common Mode Error, which might hinder the detection of the transient signals, is diminished. Such a procedure has been implemented for the first time in the literature in the analyses of CORS-TR stations. We proved the existence of CME in CORS-TR stations by applying our method to the time series both in Eurasia-fixed and regional reference frames, and by comparing the results. Generated precise velocity fields were published in national and international journals (Ozdemir, 2016, Ozdemir and Karshoğlu, 2019).

The secular rates and seasonal motions were removed from the precise and CME-reduced time series. Ensemble Empirical Mode Decomposition (EEMD) was applied to the residual time series. Since it is an experimental approach as its name implies, and hence lacks of exact mathematical description, it depends on pre-determined parameters. This may result in obtaining unstable results. We presented the effects of the user-defined parameters on the obtained results in an international conference (Ozdemir and Karşlıoğlu, 2015). GPS time series may contain white and various kinds of colored noise. Thanks to the adaptive nature of the EMD, we did not make any a priori assumptions about the type of the noise present in the time series. We suppressed the white noise by means of the filtering properties of the EMD method.

We decomposed the precise, CME-reduced, steady motions-removed, white noise-suppressed time series into uncorrelated and variance maximizing principal components (PCs) by employing PCA. Amplitudes of the PCs and eigenvectors were examined for temporal variations and spatial distributions, respectively. The significance of the detected signals is determined by looking for systematic temporal patterns, and by assessing the largeness of the eigenvalues and  $\chi^2$  values of the foremost PCs.

We demonstrated the capability of our method in the Cascadia subduction zone, located in the Pacific Northwest first, by detecting the slow slip events. We applied our method to 10 stations located in the Washington State section of the Cascadia zone, which experienced both 2007 and 2008 SSEs during approximately the same time periods. The SSEs have been detected successfully. Since these events are also detectable from the actual GPS data, we primarily aimed at showing the SNR improvement of our approach.

Secondly, we applied our algorithm to the Alaskan GPS time series to detect the transient inflation at Akutan volcano. Since the transient signal is aseismic (that is, it cannot be associated with earthquakes), and has low SNR, it cannot be identified in the original data. We detected the transient signal and demonstrated the superiority of our method against the one proposed by Ji and Herring (2011), who originally discovered the transient inflation at Akutan volcano.

Finally, we showed the capability of our method by detecting the postseismic deformation at CORS-TR sites following the October 23, 2011 Van earthquake. We used the far-field stations from the earthquake epicenter in order not to be dominated by the closer stations in the first PCs, which experienced large displacements. We proved the existence of CME in the CORS-TR time series and exhibited the effect of CME reduction in the detection of the postseismic deformation.

We conclude that the transient signal detection method proposed in this thesis can successfully detect the relatively weak tectonically-driven transient signals buried in noise in continuous GPS time series. It has high potential to be used especially in the geophysical studies where non-linear/non-stationary real-world signals are commonly investigated.

### **6.3 Future work**

Transient signal detection by generating precise coordinate time series, reducing common mode errors, removing steady motions, suppressing white noise with EMD, and decomposing into principal components with PCA has been successfully implemented in this thesis. However, following further developments in the transient signal detection are envisaged:

- The measure of signal coherence in the principal components has been realized by visually evaluating the temporal patterns and the spatial distribution of the eigenvectors. A more quantitative threshold (in addition to the variance explanation percentages) in signal detection might contribute to the robustness of the developed method.
- The adaptiveness of EMD to the input data saves us from making erroneous assumptions about the type of the noise present in the time series, in the denoising procedure. However, considering the lacking of a firm mathematical foundation for EMD, denoising results might be unstable due to several predefined parameters. Recently, significant developments have been made in EMD mathematics which can be seen as the most exciting breakthroughs since the introduction of the EMD. These developments should be followed closely, and user intervention should be minimized in the EMD process.
- We have searched the postseismic deformation following 23 October, 2011 Van earthquake at the CORS-TR stations. The effects of the other large earthquakes such as March 08, 2011 Elazig earthquake, May 24, 2014 Gokceada earthquake, June 12, 2017 Karaburun earthquake and July 20, 2017 Gokova earthquake at the CORS-TR stations might also be investigated.
- Since PCA considers spatial coherence, as the number of the stations which record the same transient signal increases, PCA tends to display the signal in the foremost PCs. Introducing PCA only the more localized transient signals in time and space increases the chances of detecting the transients. Thus, a search algorithm might be developed which maximizes the variance

explanation percentages by using a sliding window in time, and by seeking the stations of highest spatial coherence.

- All time series included in PCA have unit weight. A weighting algorithm which considers the repeatabilities of the original position time series and the uncertainties of the daily solutions might be injected to the PCA.

## REFERENCES

- Abdi, H., & Williams, L. J. (2010). Principal component analysis. *Wiley interdisciplinary reviews: computational statistics*, 2(4), 433-459.
- Aggarwal, C. C. (2015). Outlier analysis. In *Data mining* (pp. 237-263). Springer, Cham.
- Agnew, D. C. (1992). The time-domain behavior of power-law noises. *Geophysical research letters*, 19(4), 333-336.
- Aktug, B., Nocquet, J. M., Cingöz, A., Parsons, B., Erkan, Y., England, P., ... & Tekgül, A. (2009). Deformation of western Turkey from a combination of permanent and campaign GPS data: Limits to block-like behavior. *Journal of Geophysical Research: Solid Earth*, 114(B10).
- Aktuğ, B., Sezer, S., Özdemir, S., Lenk, O., & Kılıçoğlu, A. (2011). Türkiye Ulusal Temel GPS Ağı Güncel Koordinat ve Hızlarının Hesaplanması (Computation of the Actual Coordinates and Velocities of Turkish National Fundamental GPS Network). *Harita Dergisi*, (145).
- Aktuğ, B., Parmaksız, E., Kurt, M., Lenk, O., Kılıçoğlu, A., Gürdal, M. A., & Özdemir, S. (2013). Deformation of central anatolia: GPS implications. *Journal of Geodynamics*, 67, 78-96.
- Aktug, B., Ozener, H., Dogru, A., Sabuncu, A., Turgut, B., Halicioglu, K., ... & Havazli, E. (2016). Slip rates and seismic potential on the East Anatolian Fault System using an improved GPS velocity field. *Journal of Geodynamics*, 94, 1-12.
- Altamimi, Z., Collilieux, X., & Métivier, L. (2011). ITRF2008: an improved solution of the international terrestrial reference frame. *Journal of Geodesy*, 85(8), 457-473.
- Altamimi, Z., Métivier, L., & Collilieux, X. (2012). ITRF2008 plate motion model. *Journal of geophysical research: solid earth*, 117(B7).
- Altamimi, Z., Rebischung, P., Métivier, L., & Collilieux, X. (2016). ITRF2014: A new release of the International Terrestrial Reference Frame modeling nonlinear station motions. *Journal of Geophysical Research: Solid Earth*, 121(8), 6109-6131.

- Amiri-Simkooei, A. R., Tiberius, C. C. J. M., & Teunissen, S. P. (2007). Assessment of noise in GPS coordinate time series: methodology and results. *Journal of Geophysical Research: Solid Earth*, 112(B7).
- Barnhart, B. L., Nandage, H. K. W., & Eichinger, W. (2011). Assessing discontinuous data using ensemble empirical mode decomposition. *Advances in Adaptive Data Analysis*, 3(04), 483-491.
- Barnhart, B. L., Eichinger, W. E., & Prueger, J. H. (2012). Introducing an Ogive method for discontinuous data. *Agricultural and forest meteorology*, 162, 58-62.
- Bar-Sever, Y. E. (1996). A new model for GPS yaw attitude. *Journal of Geodesy*, 70(11), 714-723.
- Bartlow, N. M., Miyazaki, S. I., Bradley, A. M., & Segall, P. (2011). Space-time correlation of slip and tremor during the 2009 Cascadia slow slip event. *Geophysical Research Letters*, 38(18).
- Beavan, J. (2005). Noise properties of continuous GPS data from concrete pillar geodetic monuments in New Zealand and comparison with data from US deep drilled braced monuments. *Journal of Geophysical Research: Solid Earth*, 110(B8).
- Bedrosian, E. (1963). A product theorem for Hilbert transform. *Proc. IEEE* 51, 868-869
- Bennett, R. A. (2008). Instantaneous deformation from continuous GPS: Contributions from quasi-periodic loads. *Geophysical Journal International*, 174(3), 1052-1064.
- Blewitt, G. (1997). Basics of the GPS technique: observation equations. *Geodetic applications of GPS*, 10-54.
- Blewitt, G., & Lavallée, D. (2002). Effect of annual signals on geodetic velocity. *Journal of Geophysical Research: Solid Earth*, 107(B7), ETG-9.
- Blewitt, G. (2009). GPS and Space-Based Geodetic Methods. In *Treatise on Geophysics-Geodesy* (pp. 351-390). Elsevier.



- Blewitt, G., Kreemer, C., Hammond, W. C., & Goldfarb, J. M. (2013). Terrestrial reference frame NA12 for crustal deformation studies in North America. *Journal of Geodynamics*, 72, 11-24.
- Boashash, B. (1992). Estimating and interpreting the instantaneous frequency of a signal. I. Fundamentals. *Proceedings of the IEEE*, 80(4), 520-538.
- Boashash, B. (2015). *Time-frequency signal analysis and processing: a comprehensive reference*. Academic Press.
- Bock, Y., Prawirodirdjo, L., & Melbourne, T. I. (2004). Detection of arbitrarily large dynamic ground motions with a dense high-rate GPS network. *Geophysical Research Letters*, 31(6).
- Boehm, J., Werl, B., & Schuh, H. (2006). Troposphere mapping functions for GPS and very long baseline interferometry from European Centre for Medium-Range Weather Forecasts operational analysis data. *Journal of geophysical research: solid earth*, 111(B2).
- Boudraa, A. O., & Cexus, J. C. (2006). Denoising via empirical mode decomposition. *Proc. IEEE ISCCSP*, 4, 2006.
- Brockwell, P. J., Davis, R. A., & Fienberg, S. E. (1991). *Time Series: Theory and Methods: Theory and Methods*. Springer Science & Business Media.
- Brudzinski, M. R., & Allen, R. M. (2007). Segmentation in episodic tremor and slip all along Cascadia. *Geology*, 35(10), 907-910.
- Chang, W. L., Smith, R. B., Farrell, J., & Puskas, C. M. (2010). An extraordinary episode of Yellowstone caldera uplift, 2004–2010, from GPS and InSAR observations. *Geophysical Research Letters*, 37(23).
- Chen, Q., Huang, N., Riemenschneider, S., & Xu, Y. (2006). A B-spline approach for empirical mode decompositions. *Advances in computational mathematics*, 24(1-4), 171-195.
- Cheng, J., Yu, D., & Yang, Y. (2007). Application of support vector regression machines to the processing of end effects of Hilbert–Huang transform. *Mechanical Systems and Signal Processing*, 21(3), 1197-1211.

Christy, J. R., Spencer, R. W., & Braswell, W. D. (2000). MSU tropospheric temperatures: Dataset construction and radiosonde comparisons. *Journal of Atmospheric and Oceanic Technology*, 17(9), 1153-1170.

Cohen, L. (1995). *Time-frequency analysis* (Vol. 778). Prentice hall.

Colombo, O. L. (2008). Real-time, wide-area, precise kinematic positioning using data from internet NTRIP streams. *Proceedings of ION-GNSS-2008, Institute of Navigation, Savannah, Georgia*, 327-337.

Colominas, M. A., Schlotthauer, G., TORRES, M. E., & Flandrin, P. (2012). Noise-assisted EMD methods in action. *Advances in Adaptive Data Analysis*, 4(04), 1250025.

Colominas, M. A., Schlotthauer, G., & Torres, M. E. (2014). Improved complete ensemble EMD: A suitable tool for biomedical signal processing. *Biomedical Signal Processing and Control*, 14, 19-29.

Dach, R., Lutz, S., Walser, P., & Fridez, P. (2015). Bernese GNSS Software version 5.2. User manual, Astronomical Institute. *Bern: University of Bern, Bern Open Publishing*.

Daubechies, I. (1992). *Ten lectures on wavelets* (Vol. 61). Siam.

Daubechies, I., Lu, J., & Wu, H. T. (2011). Synchrosqueezed wavelet transforms: An empirical mode decomposition-like tool. *Applied and computational harmonic analysis*, 30(2), 243-261.

Dong, D., Herring, T. A., & King, R. W. (1998). Estimating regional deformation from a combination of space and terrestrial geodetic data. *Journal of Geodesy*, 72(4), 200-214.

Dong, D., Fang, P., Bock, Y., Cheng, M. K., & Miyazaki, S. I. (2002). Anatomy of apparent seasonal variations from GPS-derived site position time series. *Journal of Geophysical Research: Solid Earth*, 107(B4), ETG-9.

Dong, D., Fang, P., Bock, Y., Webb, F., Prawirodirdjo, L., Kedar, S., & Jamason, P. (2006). Spatiotemporal filtering using principal component analysis and Karhunen-Loeve expansion approaches for regional GPS network analysis. *Journal of geophysical research: solid earth*, 111(B3).

- Donoho, D. L. (2006). Compressed sensing. *IEEE Transactions on information theory*, 52(4), 1289-1306.
- Dow, J. M., Neilan, R. E., & Rizos, C. (2009). The international GNSS service in a changing landscape of global navigation satellite systems. *Journal of geodesy*, 83(3-4), 191-198.
- Dragert, H., Wang, K., & James, T. S. (2001). A silent slip event on the deeper Cascadia subduction interface. *Science*, 292(5521), 1525-1528.
- Dragert, H., & Wang, K. (2011). Temporal evolution of an episodic tremor and slip event along the northern Cascadia margin. *Journal of Geophysical Research: Solid Earth*, 116(B12).
- Eckl, M. C., Snay, R. A., Soler, T., Cline, M. W., & Mader, G. L. (2001). Accuracy of GPS-derived relative positions as a function of interstation distance and observing-session duration. *Journal of geodesy*, 75(12), 633-640.
- Elliott, J. R., Copley, A. C., Holley, R., Scharer, K., & Parsons, B. (2013). The 2011 Mw 7.1 van (eastern Turkey) earthquake. *Journal of Geophysical Research: Solid Earth*, 118(4), 1619-1637.
- Emre, Ö., Duman, T. Y., Özalp, S., Şaroğlu, F., Olgun, Ş., Elmacı, H., & Can, T. (2018). Active fault database of Turkey. *Bulletin of Earthquake Engineering*, 16(8), 3229-3275.
- Estey, L. H., & Meertens, C. M. (1999). TEQC: the multi-purpose toolkit for GPS/GLONASS data. *GPS solutions*, 3(1), 42-49.
- Firuzabadi, D., & King, R. W. (2012). GPS precision as a function of session duration and reference frame using multi-point software. *GPS solutions*, 16(2), 191-196.
- Flandrin, P., & Goncalves, P. (2004). Empirical mode decompositions as data-driven wavelet-like expansions. *International Journal of Wavelets, Multiresolution and Information Processing*, 2(04), 477-496.
- Flandrin, P., Rilling, G., & Goncalves, P. (2004). Empirical mode decomposition as a filter bank. *IEEE signal processing letters*, 11(2), 112-114.

- Flandrin, P., Goncalves, P., & Rilling, G. (2004, September). Detrending and denoising with empirical mode decompositions. In *2004 12th European Signal Processing Conference* (pp. 1581-1584). IEEE.
- Flandrin, P., Gonçalves, P., & Rilling, G. (2005). EMD equivalent filter banks, from interpretation to applications. In *Hilbert-Huang transform and its applications* (pp. 57-74).
- Freymueller, J. T., & Kaufman, A. M. (2010). Changes in the magma system during the 2008 eruption of Okmok volcano, Alaska, based on GPS measurements. *Journal of Geophysical Research: Solid Earth*, *115*(B12).
- Gabor, D. (1946). Theory of communication. Part 1: The analysis of information. *Journal of the Institution of Electrical Engineers-Part III: Radio and Communication Engineering*, *93*(26), 429-441.
- Gao, Y., & Shen, X. (2002). A New Method for Carrier-Phase-Based Precise Point Positioning. *Navigation*, *49*(2), 109-116.
- Geng, T., Xie, X., Fang, R., Su, X., Zhao, Q., Liu, G., ... & Liu, J. (2016). Real-time capture of seismic waves using high-rate multi-GNSS observations: Application to the 2015 Mw 7.8 Nepal earthquake. *Geophysical Research Letters*, *43*(1), 161-167.
- Gomberg, J., & Cascadia 2007 and Beyond Working Group. (2010). Slow-slip phenomena in Cascadia from 2007 and beyond: A review. *Bulletin*, *122*(7-8), 963-978.
- Grapenthin, R., & Freymueller, J. T. (2011). The dynamics of a seismic wave field: Animation and analysis of kinematic GPS data recorded during the 2011 Tohoku-oki earthquake, Japan. *Geophysical Research Letters*, *38*(18).
- Gunawan, E., Widiyantoro, S., Meilano, I., & Pratama, C. (2019). Postseismic deformation following the 2 July 2013 Mw 6.1 Aceh, Indonesia, earthquake estimated using GPS data. *Journal of Asian Earth Sciences*.
- Haines, J., Wallace, L. M., & Dimitrova, L. (2019). Slow slip event detection in Cascadia using vertical derivatives of horizontal stress rates. *Journal of Geophysical Research: Solid Earth*.

- He, X., Hua, X., Yu, K., Xuan, W., Lu, T., Zhang, W., & Chen, X. (2015). Accuracy enhancement of GPS time series using principal component analysis and block spatial filtering. *Advances in Space Research*, 55(5), 1316-1327.
- He, Z., Shen, Y., & Wang, Q. (2012). Boundary extension for Hilbert–Huang transform inspired by gray prediction model. *Signal Processing*, 92(3), 685-697.
- Herring, T. (2003). MATLAB Tools for viewing GPS velocities and time series. *GPS solutions*, 7(3), 194-199.
- Herring, T. A., Floyd, M. A., King, R. W., & McClusky, S. C. (2015). GLOBK reference manual, release 10.6. *Massachusetts Institute of Technology, Cambridge*.
- Herring, T. A., King, R. W., Floyd, M. A., & McClusky, S. C. (2018). GAMIT reference manual, release 10.7. *Massachusetts Institute of Technology, Cambridge*.
- Hirose, H., Hirahara, K., Kimata, F., Fujii, N., & Miyazaki, S. I. (1999). A slow thrust slip event following the two 1996 Hyuganada earthquakes beneath the Bungo Channel, southwest Japan. *Geophysical Research Letters*, 26(21), 3237-3240.
- Hofmann-Wellenhof, B., Lichtenegger, H., & Waskle, E. (2007). *GNSS—global navigation satellite systems: GPS, GLONASS, Galileo, and more*. Springer Science & Business Media.
- Hotelling, H. (1933). Analysis of a complex of statistical variables into principal components. *Journal of educational psychology*, 24(6), 417.
- Hou, T. Y., & Shi, Z. (2011). Adaptive data analysis via sparse time-frequency representation. *Advances in Adaptive Data Analysis*, 3(01n02), 1-28.
- Hou, T. Y., & Shi, Z. (2013). Data-driven time–frequency analysis. *Applied and Computational Harmonic Analysis*, 35(2), 284-308.
- Hou, T. Y., & Shi, Z. (2013). Sparse time-frequency representation of nonlinear and nonstationary data. *Science China Mathematics*, 56(12), 2489-2506.
- Huang, N. E., Shen, Z., Long, S. R., Wu, M. C., Shih, H. H., Zheng, Q., ... & Liu, H. H. (1998). The empirical mode decomposition and the Hilbert spectrum for nonlinear and non-stationary time series analysis. *Proceedings of the Royal Society of London. Series A: Mathematical, Physical and Engineering Sciences*, 454(1971), 903-995.

- Huang, N. E., Shen, Z., & Long, S. R. (1999). A new view of nonlinear water waves: the Hilbert spectrum. *Annual review of fluid mechanics*, 31(1), 417-457.
- Huang, N. E., Wu, M. L. C., Long, S. R., Shen, S. S., Qu, W., Gloersen, P., & Fan, K. L. (2003). A confidence limit for the empirical mode decomposition and Hilbert spectral analysis. *Proceedings of the Royal Society of London. Series A: Mathematical, Physical and Engineering Sciences*, 459(2037), 2317-2345.
- Huang, N. E., & Wu, Z. (2008). A review on Hilbert-Huang transform: Method and its applications to geophysical studies. *Reviews of geophysics*, 46(2).
- Huang, N. E. (2014). *Hilbert-Huang transform and its applications* (Vol. 16). World Scientific.
- Huang, Y., Yang, S., Qiao, X., Lin, M., Zhao, B., & Tan, K. (2017). Measuring ground deformations caused by 2015 Mw7. 8 Nepal earthquake using high-rate GPS data. *Geodesy and Geodynamics*, 8(4), 285-291.
- Jackson, J. E. (2005). *A user's guide to principal components*(Vol. 587). John Wiley & Sons.
- Ji, K. H., & Herring, T. A. (2011). Transient signal detection using GPS measurements: Transient inflation at Akutan volcano, Alaska, during early 2008. *Geophysical Research Letters*, 38(6).
- Ji, K. H., & Herring, T. A. (2012). Correlation between changes in groundwater levels and surface deformation from GPS measurements in the San Gabriel Valley, California. *Geophysical Research Letters*, 39(1).
- Ji, K. H., Yun, S. H., & Rim, H. (2017). Episodic inflation events at Akutan Volcano, Alaska, during 2005–2017. *Geophysical Research Letters*, 44(16), 8268-8275.
- Jiang, Y., Wdowinski, S., Dixon, T. H., Hackl, M., Protti, M., & Gonzalez, V. (2012). Slow slip events in Costa Rica detected by continuous GPS observations, 2002–2011. *Geochemistry, Geophysics, Geosystems*, 13(4).
- Johnson, H. O., & Agnew, D. C. (1995). Monument motion and measurements of crustal velocities. *Geophysical Research Letters*, 22(21), 2905-2908.

- Jolliffe, I. T. (2002). *Principal Component Analysis*, 2nd ed., 487 pp., Springer, New York
- Kahle, H. G., Cocard, M., Peter, Y., Geiger, A., Reilinger, R., Barka, A., & Veis, G. (2000). GPS-derived strain rate field within the boundary zones of the Eurasian, African, and Arabian Plates. *Journal of Geophysical Research: Solid Earth*, 105(B10), 23353-23370.
- Karslıođlu, M. O., Ozdemir, S., Durmaz, M., & Sopacı, E. (2017). Sabit GNSS İstasyonlarına Ait Zaman Serilerinde Zayıf Sinyallerin Tespit Edilmesi. *TUBITAK 113Y511 project report*.
- Khaldi, K., Alouane, M. T. H., & Boudraa, A. O. (2008, November). A new EMD denoising approach dedicated to voiced speech signals. In *2008 2nd International Conference on Signals, Circuits and Systems* (pp. 1-5). IEEE.
- Kılıçođlu, A., Kurt, A. İ., Tepeköylü, S., Cingöz, A., & Akça, E. (2003). Türkiye ulusal sabit GPS istasyonları ađı (TUSAGA). *Cođrafi Bilgi Sistemleri ve Jeodezik Ağlar Çalıştayı Bildirileri*, s, 44, 2003.
- Kim, D., & Oh, H. S. (2016). Empirical mode decomposition with missing values. *SpringerPlus*, 5(1).
- King, N. E., Argus, D., Langbein, J., Agnew, D. C., Bawden, G., Dollar, R. S., ... & Webb, F. H. (2007). Space geodetic observation of expansion of the San Gabriel Valley, California, aquifer system, during heavy rainfall in winter 2004–2005. *Journal of Geophysical Research: Solid Earth*, 112(B3).
- Koch, K. R. (1999). *Parameter estimation and hypothesis testing in linear models*. Springer Science & Business Media.
- Kreemer, C., Blewitt, G., & Klein, E. C. (2014). A geodetic plate motion and Global Strain Rate Model. *Geochemistry, Geophysics, Geosystems*, 15(10), 3849-3889.
- Kuo, C. Y., Chiu, K. W., Chiang, K. W., Cheng, K. C., Lin, L. C., Tseng, H. Z., ... & Lin, H. T. (2012). High-Frequency Sea Level Variations Observed by GPS Buoys Using Precise Point Positioning Technique. *Terrestrial, Atmospheric & Oceanic Sciences*, 23(2).

- Langbein, J. (2008). Noise in GPS displacement measurements from Southern California and Southern Nevada. *Journal of Geophysical Research: Solid Earth*, 113(B5).
- Larson, K. M., Bilich, A., & Axelrad, P. (2007). Improving the precision of high-rate GPS. *Journal of Geophysical Research: Solid Earth*, 112(B5).
- Larson, K. M. (2009). GPS seismology. *Journal of Geodesy*, 83(3-4), 227-233.
- Li, J. D., Rude, C. M., Blair, D. M., Gowanlock, M. G., Herring, T. A., & Pankratius, V. (2016). Computer aided detection of transient inflation events at Alaskan volcanoes using GPS measurements from 2005–2015. *Journal of Volcanology and Geothermal Research*, 327, 634-642.
- Li, W., Shen, Y., & Li, B. (2015). Weighted spatiotemporal filtering using principal component analysis for analyzing regional GNSS position time series. *Acta Geodaetica et Geophysica*, 50(4), 419-436.
- Li, X., Dick, G., Lu, C., Ge, M., Nilsson, T., Ning, T., ... & Schuh, H. (2015). Multi-GNSS meteorology: real-time retrieving of atmospheric water vapor from BeiDou, Galileo, GLONASS, and GPS observations. *IEEE Transactions on Geoscience and Remote Sensing*, 53(12), 6385-6393.
- Li, Y., Xu, C., & Yi, L. (2017). Denoising effect of multiscale multiway analysis on high-rate GPS observations. *GPS solutions*, 21(1), 31-41.
- Li, Y., Xu, C., Yi, L., & Fang, R. (2018). A data-driven approach for denoising GNSS position time series. *Journal of Geodesy*, 1-18.
- Lin, K. C., Hu, J. C., Ching, K. E., Angelier, J., Rau, R. J., Yu, S. B., ... & Huang, M. H. (2010). GPS crustal deformation, strain rate, and seismic activity after the 1999 Chi-Chi earthquake in Taiwan. *Journal of Geophysical Research: Solid Earth*, 115(B7).
- Liu, B., King, M., & Dai, W. (2018). Common mode error in Antarctic GPS coordinate time-series on its effect on bedrock-uplift estimates. *Geophysical Journal International*, 214(3), 1652-1664.
- Liu, Y., & Jin, S. (2019). Ionospheric Rayleigh wave disturbances following the 2018 Alaska earthquake from GPS observations. *Remote Sensing*, 11(8), 901.



- Luukko, P. J. J., Helske, J., & Räsänen, E. (2016). Introducing libeemd: A program package for performing the ensemble empirical mode decomposition. *Computational Statistics*, *31*(2), 545-557.
- Lyard, F., Lefevre, F., Letellier, T., & Francis, O. (2006). Modelling the global ocean tides: modern insights from FES2004. *Ocean dynamics*, *56*(5-6), 394-415.
- Mallat, S. (2009). *A Wavelet Tour of Signal Processing: The Sparse Way. AP Professional, Third Edition, London.*
- Mandelbrot, B. B., & Van Ness, J. W. (1968). Fractional Brownian motions, fractional noises and applications. *SIAM review*, *10*(4), 422-437.
- Mao, A., Harrison, C. G., & Dixon, T. H. (1999). Noise in GPS coordinate time series. *Journal of Geophysical Research: Solid Earth*, *104*(B2), 2797-2816.
- McClusky, S., Balassanian, S., Barka, A., Demir, C., Ergintav, S., Georgiev, I., ... & Kastens, K. (2000). Global Positioning System constraints on plate kinematics and dynamics in the eastern Mediterranean and Caucasus. *Journal of Geophysical Research: Solid Earth*, *105*(B3), 5695-5719.
- Mears, C. A., Schabel, M. C., & Wentz, F. J. (2003). A reanalysis of the MSU channel 2 tropospheric temperature record. *Journal of Climate*, *16*(22), 3650-3664.
- Melbourne, T. I., Szeliga, W. M., Miller, M. M., & Santillan, V. M. (2005). Extent and duration of the 2003 Cascadia slow earthquake. *Geophysical Research Letters*, *32*(4).
- Melbourne, W. (1985). The case for ranging in GPS-based geodetic systems. In *Proc. 1st int. symp. on precise positioning with GPS* (pp. 373-386).
- Mendes, V. B., & Langley, R. B. (1994, August). A comprehensive analysis of mapping functions used in modeling tropospheric propagation delay in space geodetic data. In *Proc International Symposium on Kinematic Systems in Geodesy, Geomatics and Navigation, Banff* (pp. 87-98).
- Mendes, V. B., & Langley, R. B. (1998, June). Tropospheric zenith delay prediction accuracy for airborne GPS high-precision positioning. In *Proceedings of the Institute of Navigation 54th annual meeting* (pp. 337-347).

- Miller, T. P., McGimsey, R. G., Richter, D. H., Riehle, J. R., Nye, C. J., Yount, M. E., & Dumoulin, J. A. (1998). Catalog of the historically active volcanoes of Alaska. *US Geological Survey Open-File Report*, 98(582), 104.
- Misra, P., & Enge, P. (2006). Global Positioning System: signals, measurements and performance second edition. *Massachusetts: Ganga-Jamuna Press*.
- Mogi, K. (1958). Relations between the eruptions of various volcanoes and the deformations of the ground surfaces around them. *Earthq Res Inst*, 36, 99-134.
- Nikolaidis, R. (2002). *Observation of geodetic and seismic deformation with the Global Positioning System*. Ph.D. thesis. Univ. of Calif., San Diego.
- Nyst, M., & Thatcher, W. (2004). New constraints on the active tectonic deformation of the Aegean. *Journal of Geophysical Research: Solid Earth*, 109(B11).
- Obara, K. (2002). Nonvolcanic deep tremor associated with subduction in southwest Japan. *Science*, 296(5573), 1679-1681.
- Obara, K., Hirose, H., Yamamizu, F., & Kasahara, K. (2004). Episodic slow slip events accompanied by non-volcanic tremors in southwest Japan subduction zone. *Geophysical Research Letters*, 31(23).
- Olhede, S., & Walden, A. T. (2004). The Hilbert spectrum via wavelet projections. *Proceedings of the Royal Society of London. Series A: Mathematical, Physical and Engineering Sciences*, 460(2044), 955-975.
- Oppenheim, A. V., & Schaffer, R. W. (2014). *Discrete-time signal processing*. Pearson Education.
- Ostini, L. (2012). *Analysis and quality assessment of GNSS-derived parameter time series* (Doctoral dissertation, Verlag nicht ermittelbar).
- Özdemir, S., Cingöz, A., Aktuğ, B., Lenk, O., Kurt, M., & Parmaksız, E. (2011). Sabit İstasyon Verilerinin Analizi. *TMMOB Harita ve Kadastro Mühendisleri Odası 13. Türkiye Harita Bilimsel ve Teknik Kurultayı*, 18-22 Nisan 2011, Ankara.
- Özdemir, S., & Karslıoğlu, M. O. (2015). Analysis of GNSS time series obtained from Turkish national permanent GNSS stations network-active system using Hilbert Huang Transform. *26th IUGG General Assembly*, Prague, 2015.

- Özdemir, S. (2016). TUSAGA ve TUSAGA-Aktif istasyonlarının hassas koordinat ve hızlarının hesaplanması üzerine. *Journal of Mapping*, 155, 53-81.
- Özdemir, S., Karşlıođlu, M. O., & Durmaz M. (2017). TUSAGA ve TUSAGA-Aktif Veri Analizleri: Stratejiler, Bulgular ve Öneriler. *Proceedings of Türkiye Ulusal Jeodezi Komisyonu (TUJK) Bilimsel Toplantısı-Sabit GNSS İstasyonları Uygulamaları*, Boğaziçi University, İstanbul.
- Özdemir, S., & Karşlıođlu, M. O. (2019). Soft clustering of GPS velocities from a homogeneous permanent network in Turkey. *Journal of Geodesy*, 1-25.
- Özener, H., Arpat, E., Ergintav, S., Dogru, A., Cakmak, R., Turgut, B., & Dogan, U. (2010). Kinematics of the eastern part of the North Anatolian Fault Zone. *Journal of geodynamics*, 49(3-4), 141-150.
- Pearlman, M. R., Degnan, J. J., & Bosworth, J. M. (2002). The international laser ranging service. *Advances in Space Research*, 30(2), 135-143.
- Pearson, K. (1901). LIII. On lines and planes of closest fit to systems of points in space. *The London, Edinburgh, and Dublin Philosophical Magazine and Journal of Science*, 2(11), 559-572.
- Penna, N. T., King, M. A., & Stewart, M. P. (2007). GPS height time series: Short-period origins of spurious long-period signals. *Journal of Geophysical Research: Solid Earth*, 112(B2).
- Petit, G., & Luzum, B. (2010). *IERS conventions (2010)* (No. IERS-TN-36). Bureau International Des Poids Et Mesures Sevres (France).
- Petrie, E. J., King, M. A., Moore, P., & Lavallée, D. A. (2010). Higher-order ionospheric effects on the GPS reference frame and velocities. *Journal of geophysical research: solid earth*, 115(B3).
- Prawirodirdjo, L., & Bock, Y. (2004). Instantaneous global plate motion model from 12 years of continuous GPS observations. *Journal of Geophysical Research: Solid Earth*, 109(B8).
- Priestley, M. B. (1981). Spectral analysis and time series. New York, Academic Press.

- Rea, W., Oxley, L., Reale, M., & Brown, J. (2009). Estimators for long range dependence: an empirical study. *arXiv preprint arXiv:0901.0762*.
- Reilinger, R., McClusky, S., Vernant, P., Lawrence, S., Ergintav, S., Cakmak, R., ... & Nadariya, M. (2006). GPS constraints on continental deformation in the Africa-Arabia-Eurasia continental collision zone and implications for the dynamics of plate interactions. *Journal of Geophysical Research: Solid Earth*, *111*(B5).
- Rilling, G., Flandrin, P., & Goncalves, P. (2003, June). On empirical mode decomposition and its algorithms. In *IEEE-EURASIP workshop on nonlinear signal and image processing*(Vol. 3, No. 3, pp. 8-11). NSIP-03, Grado (I).
- Rilling, G., Flandrin, P., & Gonçalves, P. (2005, March). Empirical mode decomposition, fractional Gaussian noise and Hurst exponent estimation. In *Proceedings.(ICASSP'05). IEEE International Conference on Acoustics, Speech, and Signal Processing, 2005.* (Vol. 4, pp. iv-489). IEEE.
- Rogers, G., & Dragert, H. (2003). Episodic tremor and slip on the Cascadia subduction zone: The chatter of silent slip. *Science*, *300*(5627), 1942-1943.
- Santamaría-Gómez, A., Bouin, M. N., Collilieux, X., & Wöppelmann, G. (2011). Correlated errors in GPS position time series: Implications for velocity estimates. *Journal of Geophysical Research: Solid Earth*, *116*(B1).
- Savage, J. C., & Langbein, J. (2008). Postearthquake relaxation after the 2004 M6 Parkfield, California, earthquake and rate-and-state friction. *Journal of Geophysical Research: Solid Earth*, *113*(B10).
- Schaffrin, B., & Bock, Y. (1988). A unified scheme for processing GPS dual-band phase observations. *Bulletin géodésique*, *62*(2), 142-160.
- Schmalzle, G. M., McCaffrey, R., & Creager, K. C. (2014). Central Cascadia subduction zone creep. *Geochemistry, Geophysics, Geosystems*, *15*(4), 1515-1532.
- Schmidt, D. A., & Gao, H. (2010). Source parameters and time-dependent slip distributions of slow slip events on the Cascadia subduction zone from 1998 to 2008. *Journal of Geophysical Research: Solid Earth*, *115*(B4).
- Schroeder, M. (2009). *Fractals, chaos, power laws: Minutes from an infinite paradise*. Courier Corporation.

- Schuh, H., & Behrend, D. (2012). VLBI: a fascinating technique for geodesy and astrometry. *Journal of Geodynamics*, 61, 68-80.
- Seeber, G. (2003). Satellite Geodesy, 2nd completely revised and extended edition. *Walter de Gruyter GmbH & Co. KG*, 10785.
- Segall, P., & Davis, J. L. (1997). GPS applications for geodynamics and earthquake studies. *Annual Review of Earth and Planetary Sciences*, 25(1), 301-336.
- Shen, S. S., Shu, T., Huang, N. E., Wu, Z., North, G. R., Karl, T. R., & Easterling, D. R. (2014). HHT analysis of the nonlinear and non-stationary annual cycle of daily surface air temperature data. In *Hilbert–Huang Transform and Its Applications* (pp. 261-283).
- Shen, Y., Li, W., Xu, G., & Li, B. (2014). Spatiotemporal filtering of regional GNSS network's position time series with missing data using principle component analysis. *Journal of Geodesy*, 88(1), 1-12.
- Shlens, J. (2014). A tutorial on principal component analysis. *arXiv preprint arXiv:1404.1100*.
- Silverii, F., D'Agostino, N., Borsa, A. A., Calcaterra, S., Gambino, P., Giuliani, R., & Mattone, M. (2019). Transient crustal deformation from karst aquifers hydrology in the Apennines (Italy). *Earth and Planetary Science Letters*, 506, 23-37.
- Smith, L. I. (2002). *A tutorial on principal components analysis*.
- Soler, T., Michalak, P., Weston, N. D., Snay, R. A., & Foote, R. H. (2006). Accuracy of OPUS solutions for 1-to 4-h observing sessions. *GPS solutions*, 10(1), 45-55.
- Spinler, J. C., Bennett, R. A., Anderson, M. L., McGill, S. F., Hreinsdóttir, S., & McCallister, A. (2010). Present-day strain accumulation and slip rates associated with southern San Andreas and eastern California shear zone faults. *Journal of Geophysical Research: Solid Earth*, 115(B11).
- Szeliga, W., Melbourne, T. I., Miller, M. M., & Santillan, V. M. (2004). Southern Cascadia episodic slow earthquakes. *Geophysical Research Letters*, 31(16).

- Szeliga, W., Melbourne, T., Santillan, M., & Miller, M. (2008). GPS constraints on 34 slow slip events within the Cascadia subduction zone, 1997–2005. *Journal of Geophysical Research: Solid Earth*, *113*(B4).
- Tanaka, Y., Ohta, Y., & Miyazaki, S. I. (2019). Real-Time Coseismic Slip Estimation via the GNSS Carrier Phase to Fault Slip Approach: A Case Study of the 2016 Kumamoto Earthquake. *Geophysical Research Letters*, *46*(3), 1367-1374.
- Tarpey, T., & Flury, B. (1996). Self-consistency: A fundamental concept in statistics. *Statistical Science*, *11*(3), 229-243.
- Tian, Y., & Shen, Z. K. (2016). Extracting the regional common-mode component of GPS station position time series from dense continuous network. *Journal of Geophysical Research: Solid Earth*, *121*(2), 1080-1096.
- Tiryakioglu, I., Yavasoglu, H., Ugur, M. A., Özkaymak, C., Yilmaz, M., Kocaoglu, H., & Turgut, B. (2017). Analysis of October 23 (Mw 7.2) and November 9 (Mw 5.6), 2011 Van Earthquakes Using Long-Term GNSS Time Series. *Earth Sciences Research Journal*, *21*(3), 147-156.
- Tomecek, S. (2011). *Plate tectonics*. Infobase Publishing.
- Torge, W., & Müller, J. (2012). *Geodesy*. Walter de Gruyter.
- Torres, M. E., Colominas, M. A., Schlotthauer, G., & Flandrin, P. (2011, May). A complete ensemble empirical mode decomposition with adaptive noise. In *2011 IEEE international conference on acoustics, speech and signal processing (ICASSP)* (pp. 4144-4147). IEEE.
- Tregoning, P., Watson, C., Ramillien, G., McQueen, H., & Zhang, J. (2009). Detecting hydrologic deformation using GRACE and GPS. *Geophysical Research Letters*, *36*(15).
- Tregoning, P., & Watson, C. (2009). Atmospheric effects and spurious signals in GPS analyses. *Journal of Geophysical Research: Solid Earth*, *114*(B9).
- Tsolis, G. S., & Xenos, T. D. (2009). Seismo-ionospheric coupling correlation analysis of earthquakes in Greece, using empirical mode decomposition. *Nonlinear Processes in Geophysics*, *16*(1), 123-130.

- Tukey, J. W. (1977) Explanatory data analysis. Addison Wesley, Reading.
- Uzel, T., Eren, K., Gulal, E., Tiryakioglu, I., Dindar, A. A., & Yilmaz, H. (2013). Monitoring the tectonic plate movements in Turkey based on the national continuous GNSS network. *Arabian Journal of Geosciences*, 6(9), 3573-3580.
- Üstün, A., Tuşat, E., Yalvaç, S., Özkan, İ., Eren, Y., Özdemir, A., ... & Doğanalp, S. (2015). Land subsidence in Konya Closed Basin and its spatio-temporal detection by GPS and DInSAR. *Environmental earth sciences*, 73(10), 6691-6703.
- Vautard, R., & Ghil, M. (1989). Singular spectrum analysis in nonlinear dynamics, with applications to paleoclimatic time series. *Physica D: Nonlinear Phenomena*, 35(3), 395-424.
- Vergnolle, M., Walpersdorf, A., Kostoglodov, V., Tregoning, P., Santiago, J. A., Cotte, N., & Franco, S. I. (2010). Slow slip events in Mexico revised from the processing of 11 year GPS observations. *Journal of Geophysical Research: Solid Earth*, 115(B8).
- Vidal, R., Ma, Y., & Sastry, S. S. (2016). Principal component analysis. In *Generalized principal component analysis* (pp. 25-62). Springer, New York, NY.
- Walwer, D., Calais, E., & Ghil, M. (2016). Data-adaptive detection of transient deformation in geodetic networks. *Journal of Geophysical Research: Solid Earth*, 121(3), 2129-2152.
- Wang, G., Chen, X. Y., Qiao, F. L., Wu, Z., & Huang, N. E. (2010). On intrinsic mode function. *Advances in Adaptive Data Analysis*, 2(03), 277-293.
- Wang, W., Zhao, B., Wang, Q., & Yang, S. (2012). Noise analysis of continuous GPS coordinate time series for CMONOC. *Advances in space research*, 49(5), 943-956.
- Wdowinski, S., Bock, Y., Zhang, J., Fang, P., & Genrich, J. (1997). Southern California permanent GPS geodetic array: Spatial filtering of daily positions for estimating coseismic and postseismic displacements induced by the 1992 Landers earthquake. *Journal of Geophysical Research: Solid Earth*, 102(B8), 18057-18070.
- Weng, B., Blanco-Velasco, M., & Barner, K. E. (2006, August). ECG denoising based on the empirical mode decomposition. In *2006 International Conference of the IEEE Engineering in Medicine and Biology Society* (pp. 1-4). IEEE.

- Williams, S. D., Bock, Y., Fang, P., Jamason, P., Nikolaidis, R. M., Prawirodirdjo, L., ... & Johnson, D. J. (2004). Error analysis of continuous GPS position time series. *Journal of Geophysical Research: Solid Earth*, *109*(B3).
- Willis, P., Fagard, H., Ferrage, P., Lemoine, F. G., Noll, C. E., Noomen, R., ... & Tavernier, G. (2010). The international DORIS service (IDS): toward maturity. *Advances in space research*, *45*(12), 1408-1420.
- Wu, F., & Qu, L. (2008). An improved method for restraining the end effect in empirical mode decomposition and its applications to the fault diagnosis of large rotating machinery. *Journal of sound and vibration*, *314*(3-5), 586-602.
- Wu, H. T., Flandrin, P., & Daubechies, I. (2011). One or two frequencies? The synchrosqueezing answers. *Advances in Adaptive Data Analysis*, *3*(01n02), 29-39.
- Wu, Z., & Huang, N. E. (2004). A study of the characteristics of white noise using the empirical mode decomposition method. *Proceedings of the Royal Society of London. Series A: Mathematical, Physical and Engineering Sciences*, *460*(2046), 1597-1611.
- Wu, Z., & Huang, N. E. (2005). Statistical significance test of intrinsic mode functions. In *Hilbert-Huang Transform and its applications* (pp. 107-127).
- Wu, Z., & Huang, N. E. (2009). Ensemble empirical mode decomposition: a noise-assisted data analysis method. *Advances in adaptive data analysis*, *1*(01), 1-41.
- Wu, Z., & Huang, N. E. (2010). On the filtering properties of the empirical mode decomposition. *Advances in Adaptive Data Analysis*, *2*(04), 397-414.
- Wubben, G. (1985). Software developments for geodetic positioning with GPS using TI 4100 code and carrier measurements. In *Proceedings 1st international symposium on precise positioning with the global positioning system* (pp. 403-412). US Department of Commerce.
- Wyatt, F. K. (1989). Displacement of surface monuments: Vertical motion. *Journal of Geophysical Research: Solid Earth*, *94*(B2), 1655-1664.
- Xu, G., Xu, C., Wen, Y., & Yin, Z. (2019). Coseismic and Postseismic Deformation of the 2016 MW 6.2 Lampa Earthquake, Southern Peru, Constrained by Interferometric Synthetic Aperture Radar. *Journal of Geophysical Research: Solid Earth*.



Xun, J., & Yan, S. (2008). A revised Hilbert–Huang transformation based on the neural networks and its application in vibration signal analysis of a deployable structure. *Mechanical Systems and signal processing*, 22(7), 1705-1723.

Yan, J., & Lu, L. (2014). Improved Hilbert–Huang transform based weak signal detection methodology and its application on incipient fault diagnosis and ECG signal analysis. *Signal Processing*, 98, 74-87.

Yeh, J. R., Shieh, J. S., & Huang, N. E. (2010). Complementary ensemble empirical mode decomposition: A novel noise enhanced data analysis method. *Advances in adaptive data analysis*, 2(02), 135-156.

Zhang, J., Bock, Y., Johnson, H., Fang, P., Williams, S., Genrich, J., ... & Behr, J. (1997). Southern California Permanent GPS Geodetic Array: Error analysis of daily position estimates and site velocities. *Journal of geophysical research: solid earth*, 102(B8), 18035-18055.

Zumberge, J. F., Heflin, M. B., Jefferson, D. C., Watkins, M. M., & Webb, F. H. (1997). Precise point positioning for the efficient and robust analysis of GPS data from large networks. *Journal of geophysical research: solid earth*, 102(B3), 5005-5017.



## CURRICULUM VITAE

### PERSONAL INFORMATION

Surname, Name : Özdemir, Soner  
Nationality : Turkish (TC)  
Date and Place of Birth : December 25, 1982, Giresun/Turkey  
E-mail : soner.zdemir@gmail.com

### EDUCATION

<b>Degree</b>	<b>Institution</b>	<b>Year of Graduation</b>
M.Sc.	METU, Civil Eng./Geomatics Lab.	2014 (Highest GPA)
B.Sc.	High Tech. School of Mapping, Geomatics Eng.	2007 (Highest GPA)
B.Sc.	National Defense Univ., Systems Eng.	2005
HS	Kuleli Military High School	2001

### PROFESSIONAL EXPERIENCE

<b>Year</b>	<b>Place</b>	<b>Enrollment</b>
2007-2008	GDM	GPS Officer
2009-2012	GDM	Permanent GNSS Stations Data Manager
2014-2017	GDM	Analyst of Geodetic Networks
2017-	GDM	Head of Geodetic Networks Section
2011-2012, 2014-	Turkish National Geodesy Commission	Secretary

## **FOREIGN LANGUAGES**

Proficient English, Intermediate Polish

## **AWARDS**

Turkish National Geodesy Commission – Young Scientist Award (2016)

## **EDITORSHIP**

Turkish National Geodesy Program, Turkish National Geodesy Commission, General Directorate of Mapping, Ankara, 2016

## **PUBLICATIONS**

### **International Journal Publications (SCI):**

Özdemir S, Karşlıoğlu MO (2019) Soft clustering of GPS velocities from a homogeneous network in Turkey. *J Geodesy*. <https://doi.org/10.1007/s00190-019-01235-z>.

Yıldız H, Andersen O, Simav M, Aktuğ B, Özdemir, S. (2013) Estimates of vertical land motion along the southwestern coasts of Turkey from coastal altimetry and tide gauge data, *Advances in Space Research*.

Aktuğ B, Meherremov E, Kurt M, Özdemir S, Esedov N, Lenk O (2012) GPS constraints on the deformation of Azerbaijan and surrounding regions, *Journal of Geodynamics*.

Aktuğ B, Parmaksız E, Kurt M, Lenk O, Kılıçoğlu A, Gürdal MA, Özdemir S (2012) Deformation of Central Anatolia: GPS Implications, Journal of Geodynamics.

#### **National Journal Publications:**

Özdemir S (2016) TUSAGA ve TUSAGA-Aktif İstasyonlarının Hassas Koordinat ve Hızlarının Hesaplanması Üzerine, Harita Dergisi, 155, 53-81.

Aktuğ B, Seymen S, Kurt M, Parmaksız E, Lenk O, Sezer S, Özdemir S (2011) ED-50 (European Datum-1950) İle TUREF (Türkiye Ulusal Referans Çerçevesi) Arasında Datum Dönüşümü, Harita Dergisi, 146, 8-17.

Aktuğ B, Sezer S, Özdemir S, Lenk O, Kılıçoğlu A (2011) Türkiye Ulusal Temel GPS Ağı Güncel Koordinat ve Hızlarının Hesaplanması, Harita Dergisi, 145, 1-14.

#### **International Conference Proceedings:**

Dogru A., F. Bulut, B. Aktug, S. Ozdemir, and H. Ozener, "Seismo-geodetic Behavior of Basic Tectonic Elements in Anatolia", 19th. General Assembly of WEGENER (WEGENER 2018), 10-13 September 2018, Grenoble, France.

Özener, H., Dogru, A., Aktug, B., Ozdemir, S., (2017) "Seismo-geodetic Behavior of Basic Tectonic Elements in Anatolian Region and Surroundings", IAG-IASPEI, 30 July-4August 2017, Kobe, Japan.

Özdemir, S., Akabali, O.A., Yıldız, H., Kurt, A.I., Sezen, E., Simav, M., (2017) National Report of Turkey to EUREF Symposium, 17-19 May 2017, Wroclaw, Poland.

Özener, H., Dogru, A., Bulut, F., Aktug, B., Ozdemir, S., (2017) "Seismo-geodetic Behavior of Basic Tectonic Elements in Anatolia", 23-28 April 2017, EGU 2017, Vienna, Austria.

Özdemir, S., Karslıoğlu, M.O., (2015) Analysis of GPS Time Series Obtained from Turkish National Permanent GNSS Stations Network-Active System Using Hilbert-Huang Transform, 26th IUGG General Assembly, June 22-July 2 2015, Prague, Czech Republic.

Özdemir, S., Aktug, B., Lenk, O., Kurt, M., Parmaksız, E. (2011) Monitoring Deformation at the Intersection of Eurasian, Anatolian and Arabian Plates, IUGG General Assembly, 28 June – 7 July 2011, Melbourne, Australia.

Aktug, B., Arıkan, F., Arıkan, O., Sezen, U., Toket, C., Lenk, O., Kurt, M., Parmaksız, E., Özdemir, S. (2011) Space Weather Activities of Ionolab Group Using CORS-TR GPS Network, Recent Advances in Space Technologies, Harbiye Military Museum And Culture Center, 9-11 June, 2011, Istanbul.

Özdemir, S., Aktuğ, B., Parmaksız, E., Kurt, M., Cingöz, A., Erkan, Y. (2010) Monitoring the kinematics of Anatolia through Continuous GPS Observations, 15th General Assembly of WEGENER, 14-17 September 2010, Bogazici University.

Meherremov, E., Aktuğ, B., Parmaksız, E., Kurt, M., Esedov, N., Kılıçoğlu, A., Özdemir, S., Seymen, S. (2010) Kinematics of Azerbaijan and surroundings through GPS Observations, 15th General Assembly of WEGENER, 14-17 September 2010, Bogazici University.

Aktuğ, B., Parmaksız, E., Kurt, M., Kılıçoğlu, A., Gürdal, M.A., Özdemir, S., (2010) Deformation of Central Anatolia by GPS Data, 15th General Assembly of WEGENER, 14-17 September 2010, Bogazici University.

Aktuğ, B., Özdemir, S., Sezer, S., Lenk, O., Kılıçoğlu, A., Simav, M., Direnç, A. (2010) Deformation of Central Anatolia through GPS Observations, EGU General Assembly, 02-07 May 2010, Vienna, Austria.

Aktuğ, B., Lenk, O., Kılıçoğlu, A., Cingöz, A., Özdemir, S., (2009) Network Maintenance and Reference Frame Definition under interseismic, coseismic and postseismic deformation, Geodesy for Planet, Assembly of International Association of Geodesy, 31 August – 4 September 2009, Buenos Aires.

Aktuğ, B., Lenk, O., Kılıçoğlu, A., Cingöz, A., Özdemir, S., (2009) Recent slip rate constraints on Eurasia, Anatolia, Arabia boundaries, Geodesy for Planet, Assembly of International Association of Geodesy, 31 August – 4 September 2009, Buenos Aires.

Aktuğ, B., Lenk, O., Kılıçoğlu, A. Cingöz, A. Özdemir, S., (2009) Deformation of Western Anatolia, 62. Jeoloji Kurultayı, 13-17 Nisan 2009, Maden Tetkik Arama Genel Müdürlüğü Kültür Sitesi, Ankara.

Aktuğ, B., Lenk, O., Kılıçoğlu, A. Cingöz, A. Özdemir, S., (2009) How rigid is Central Anatolia: GPS Implications, 62. Jeoloji Kurultayı, 13-17 Nisan 2009, Maden Tetkik Arama Genel Müdürlüğü Kültür Sitesi, Ankara.

Aktuğ, B., Lenk, O., Kılıçoğlu, D.E.Ilgın, A. Cingöz, A. Özdemir, S., (2009) Recent Constraints on the Deformation of Central Anatolia: GPS Implications, International Symposium on Historical Earthquakes and Conservations of Monuments and Sites in the Eastern Mediterranean Region, 500th Aniversary Year of the 1509 September 10 Marmara Earthquake, 10-12 September 2009, İstanbul, Turkey.

#### **National Conference Proceedings:**

Özdemir, S., Karşlıoğlu, M.O., (2017), TUSAGA ve TUSAGA-Aktif Veri Analizleri: Stratejiler, Bulgular ve Öneriler, Türkiye Ulusal Jeodezi Komisyonu Sabit GNSS

İstasyonları Uygulamaları Çalıştayı, 02-03 Kasım 2017, Boğaziçi Üniversitesi, İstanbul.

Özdemir, S., Kurt, M., Aktuğ, B. (2012) GNSS ile Elipsoit Yükseklik Tayini ve Katı Yer Gelgit Modellerinin Belirlenen Elipsoit Yüksekliklerine Etkisi, TUJK Türkiye Ulusal Yükseklik Sisteminin Modernizasyonu Çalıştayı, 28-30 Mart 2012, Zonguldak Karaelmas Üniversitesi, Zonguldak.

Özdemir, S., Cingöz, A., Aktuğ, B., Lenk, O., Kurt, M., Parmaksız, E. (2011) Sabit İstasyon Verilerinin Analizi, 13. Türkiye Harita Bilimsel Ve Teknik Kurultayı, 18-22 Nisan 2011, Sheraton Oteli, Ankara.

Aktuğ, B., Seymen, S., Kurt, M., Parmaksız, E., Lenk, O., Sezer, S., Özdemir, S. (2011). ED50 (EUROPEAN DATUM1950) ile TUREF (Türkiye Ulusal Referans Çerçevesi) Arasında Datum Dönüşüm Çalışmaları, 13. Türkiye Harita Bilimsel Ve Teknik Kurultayı, 18-22 Nisan 2011, Sheraton Oteli, Ankara.

Özdemir, S., Cingöz, A., Aktuğ, B., Kurt, M., Erkan, Y., Peker, S. (2011) Türkiye’de Sabit GNSS İstasyonlarının CBS Uygulamaları İçin Anlamı ve Güncel Analizleri, TMMOB Coğrafi Bilgi Sistemleri Kongresi, 31 Ekim - 04 Kasım 2011, Antalya.

Özdemir, S., Aktuğ, B., Kurt, M., Lenk, O., Erkan, Y., Peker, S.(2011) TUSAGA ve TUSAGA-Aktif, Türkiye Ulusal Jeodezi Komisyonu Çalıştayı, 23-25 Kasım 2011, Boğazici Üniversitesi, İstanbul.

Özdemir, S., Aktuğ, B., Kurt, M., Lenk, O., Erkan, Y., Peker, S.(2011) TUSAGA-Aktif Sistemi ile İyonosferik Çalışmalara Ait Ön Sonuçlar, Türkiye Ulusal Jeodezi Komisyonu Çalıştayı, 23-25 Kasım 2011, Boğazici Üniversitesi, İstanbul.

Özdemir, S., Gürdal, M.A., Cingöz, A., Mert, İ., Buyruk, T., Erkan Y., Atalar, K., Aysezen, M.Ş., Lenk, O., Aktuğ, B. (2007) Regional Testing of Weighted-Mean Temperature Predictions and Its Effects on GPS-Derived Precipitable Water



Estimates, Türkiye Ulusal Jeodezi Komisyonu Jeodezi ve Atmosfer Çalıştayı, Ortadoğu Teknik Üniversitesi, 14-15 Kasım 2007, Ankara.

Aktuğ, B., Lenk, O., Kılıçoğlu, A. Cingöz, A. Özdemir, S., (2008) Türkiye Hız Alanı, Aktif Tektonik Araştırma Grubu Toplantısı, 8 Kasım 2008, Akçakoca.

Aktuğ, B., Lenk, O., Kılıçoğlu, A. Cingöz, A. Özdemir, S., (2008) Yersel Koordinat Sistemleri ve Türkiye, Bakanlıklararası Harita ve Harita İşlerini Koordinasyon ve Planlama Kurulu 1. Sempozyumu, 8 Kasım 2008, Ortadoğu Teknik Üniversitesi, Ankara.